June 2020

BM@N Analysis Note

Inverse kinematics nucleon knockout and SRC measurements with a 4 GeV/c/u carbon beam

Analysis Team: M. Patsyuk, J. Kahlbow, G. Laskaris, M. Duer, V. Lenivenko, E. P. Segarra, T. Atovullaev, G. Johansson, T. Aumann, A. Corsi, O. Hen, M. Kapishin, V. Panin, E. Piasetzky, M. Rumyantsev, N. Voytishin, S. Merts

Abstract

This analysis note reports on our measurement of the scattering of 4 GeV/c/u ^{12}C ions from hydrogen in inverse quasi-free kinematics. The ground-state distribution of single nucleons in the p-shell of ^{12}C is studied by detecting two protons at large angles in coincidence with an intact ^{11}B nucleus. The ^{11}B detection is shown to select the transparent part of the reaction and exclude the otherwise large contributions from initial and final state interactions (ISI/FSI) that would break the ^{11}B apart. By detecting residual ^{10}B and ^{10}Be nuclei, we further identified short-range correlated (SRC) nucleon-nucleon pairs, and establish the separation of the pair wave-function from that of the residual nuclear system. All measured reactions are well described by theoretical calculations that do not contain ISI/FSI.

Contents

1. Experimental Setup:

The experiment took place at the Joint Institute for Nuclear Research (JINR), using a 4 GeV/c/nucleon ion beam from the Nuclotron accelerator, a stationary liquid hydrogen target (30 cm long), and a modified BM@N (Baryonic Matter at Nuclotron) experimental setup [9], as shown in Fig. 1.1

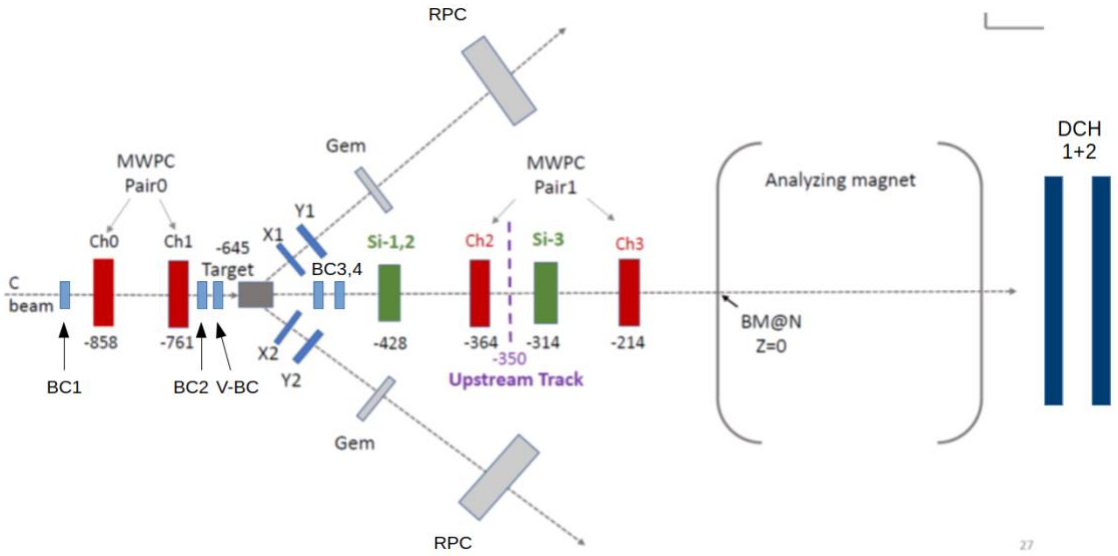

Fig 1.1: Experimental setup, showing only the detectors used for this analysis.

1.1 Beam Monitoring

The incident beam was monitored upstream the target using two thin scintillator-based beam counters (BCs) used for charge identification, a beam-halo veto beam counter (V-BC), and two multi-wire proportional chambers (MWPCs) for event-by-event beam tracking. The most upstream BC is referred to here as BC1 while the one closer to the target is called BC2, cf. Fig. 1.1.

Each of the two BCs was 3 mm thick and was readout using one PMT. The BC closer to the target was unique in that it was readout by an MCP-PMT that allowed it to be used to define the event start time t_0. For the analysis of the beam monitoring data see chapters 3 and 4.

1.2 Two-Arm Spectrometer

A two-arm spectrometer (TAS) was placed down-stream of the target to detect the two protons from the (p,2p) reaction that emerge at 24° − 37°, corresponding to 90° quasielastic (QE) scattering in the two-protons center-of-mass (c.m.) frame. Each spectrometer arm consisted of scintillator trigger counters (TC, marked as X1, X2, Y1, Y2 in Fig. 1.1), gas electron multiplier (GEM) stations, and multi-gap resistive plate chamber (RPC) walls.

The GEM stations are placed at a distance of 2.3 m from the center of the target. Each GEM station contained two GEM planes with the dimensions of 66 cm (x) x 40 cm (y) each, placed on top of each other (centered at y = 0) to increase the overall sensitive area to 66 cm x 80 cm. The spatial resolution of the GEM hit is 300 µm.

Each RPC detector station, located at the end of the two arms at a distance of 5 m from the target, has a sensitive area of 1.1 m x 1.2 m. Each station consists of two gas boxes next to each other, each holds 5 multi-gap RPC planes inside [10]. Two neighboring planes within one box overlap by 5 cm in y direction. Each plane has 30 cm long 1.2 cm wide horizontally aligned readout strips with a pitch of 1.25 cm. The measured x position is obtained by the time difference measured between the ends of one strip. The resolution is 0.6 cm.

Charged particle tracks were reconstructed using their hit location in the GEM and RPC walls. And the reaction vertex is reconstructed from those two tracks. The time difference between the RPC and t_0 signals define the proton time of flight (TOF), that is used to determine its momentum from the measured track length, assuming the particle is a proton.

In addition, each arm was equipped with two trigger counters (TC), scintillator planes close to the target. The X (X1, X2) planes consisted of two scintillators with dimensions of 30 cm x 15 cm x 0.5 cm located vertically side by side and read out by one PMT each. It was located closest to the target at a distance of 42 cm from the target center. Each Y plane (Y1, Y2) was a single scintillator piece of 50 cm x 50 cm x 2 cm, read out by two PMTs. The distance between the target center and the Y planes was 170 cm. One X detector covered a solid angle of 0.46 sr, and thus the largest acceptance, while the Y detector covers basically the acceptance of the GEM station of 0.088 sr.

Overall, each arm covers a solid angle of 0.06 sr, limited by the RPC acceptance, cf. Fig. 1.2. For the analysis of the TAS data see chapter 5.

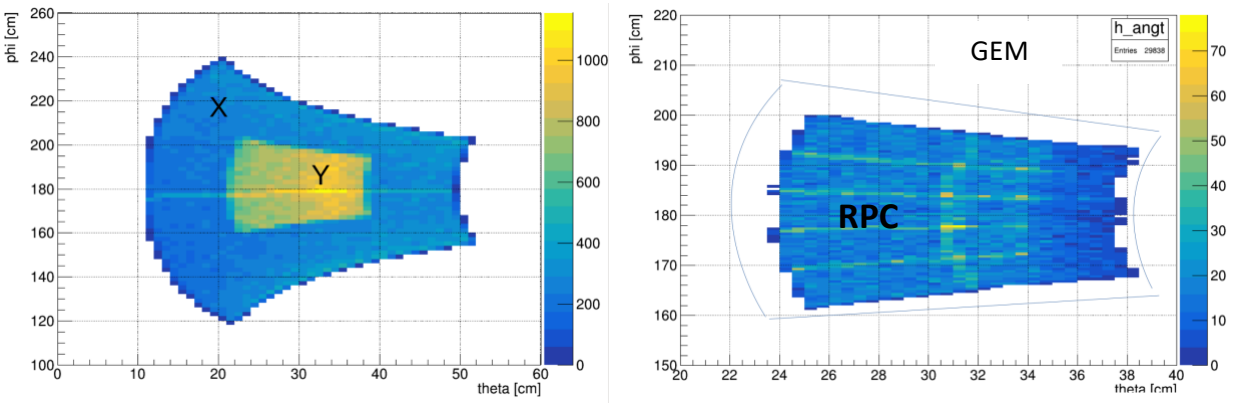

Fig. 1.2: Angular coverage of TAS detectors. Left: X and Y detectors. Right: RPC and GEM (covering larger acceptance, indicated with lines around).

1.3 Fragment Tracking

Nuclear fragments produced by the beam and emitted at small angles (< ~1°) with respect to the incident beam are tracked in the beamline. Three silicon (Si) planes and two MWPCs were placed in the beam-line downstream the target to measure the fragment scattering angle. Following the MWPCs, the fragments enter a large acceptance 2.87 T·m dipole magnet. Two drift chambers (DCH) are used to measure the fragment trajectory after the magnet.

We used one pair of MWPC chambers after the target for fragment tracking [1] (and one pair in front of the target). Each chamber has six planes {X,U,V,X,U,V}. The X wires are aligned in y direction, U and V planes are oriented ±60° to X. The distance between wires within one plane is 2.5 mm, the distance between neighboring planes is 1 cm. In total 2304 wires are read out. The active area of each chamber is 500 cm² (22 cm x 22 cm). About 1 m separated the chambers in the first pair upstream the target and 1.5 m between the chambers in the second pair downstream the target. The polar angle acceptance of the chambers downstream the target is 1.46°.

An additional tracking system composed of three Silicon planes [2] was also placed downstream the target. Its combination with the target downstream MWPCs increased the fragment tracking efficiency. The first and second Si planes share the same housing. The first plane consists of four modules, the second plane has two modules, the third plane has eight modules. Each module has 640 X-strips (vertical in y-direction) and 640 X`-strips (tilted 2.5° relative to X strips). The first plane has smaller modules with 614 X` strips and 640 X strips. The first two planes and the third plane are separated by 109 cm. The angular acceptance of the Si detector system is 1.58°. The design resolution of 1 mm for the y-coordinate and 50 µm for the x-coordinate was achieved in the experiment.

Two large-area drift chambers (DCH), separated by 2 m, are located downstream the bending magnet. These detectors are used for tracking the charged fragments in the forward direction. Together with the information of MWPC and Si detectors upstream the magnet, the bending angle and thus the magnetic rigidity of the tracked ions is determined. Each chamber consists of eight coordinate planes, twice {X,Y,U,V}, where X wires are perpendicular to the x-axis, Y wires are at 90° relative to X, and U and V are tilted by ±45◦, respectively. The distance between wires within one plane is 1 cm, in total 12,300 wires are read out. The spatial resolution, given as residual resolution, for one plane (X, Y, U, or V) is around 200 μm (1σ). It is obtained by the difference between the measured hit and the position from the reconstructed track at that plane. The efficiency of around 98% (97%) for each plane was estimated for the first (second) DCH based on the reconstructed matched track in the second (first) DCH. A reconstructed track within one DCH chamber has at least 6 points.

Inside the gap of the analyzer magnet, several GEM modules were placed for possible particle tracking along the bending curve. In between the DCH chambers is an TOF RPC (TOF-700) and downstream of it was a zero-degree calorimeter (ZDC). A neutron detector, LAND, was brought from GSI for this experiment and placed next to the ZDC. The analysis reported here does not make use of the magnet GEMs, the TOF-700, ZDC, and LAND detectors. They are expected to be used in future analyses. For the analysis of the fragments see chapter 6.

2. Data Acquisition (DAQ) and Trigger System:

Readout of the front-end electronics of the BM@N detectors is done event-by-event based on the information of the trigger system [3]. Timing information were read out from DCH and RPC (two-edge time stamp) and processed by Time to Digital Converters (TDC) based on HPTDC chip with typical accuracy of 20 ps for RPC and 60 ps for DCH. The amplitude information were read out from the detector systems of Si and GEMs and processed by Amplitude to Digital Converters (ADC). The last 30 μs of waveforms were read back. The clock and time synchronization was performed using White Rabbit protocol.

Trigger detector information was processed by TQDC16VS (waveform information) and TDC72VHL (timing information) modules. A CAEN digitizer was used to collect raw trigger event rates that are used for absolute luminosity extraction.

The experiment used four triggers, detailed in the following, for main physics runs and for monitoring and calibration purposes. The triggers only use information from scintillator counters in the beamline and in the TAS, see Fig 2.1 for their readout scheme. The trigger configuration scheme is shown in Fig. 2.2 and Table 2.1 summarizes the conditions for the different triggers that are explained in detail in the following.

Table 2.1: Trigger Matrix showing the different coincident input triggers for collecting the data.

Trigger	BC1	BC2	!V-BC	AndXY	OrXY
Beam	x	x	x		
AndSRC	x	x	x	x	
OrSRC	x	x	x		x

Beam trigger: Our basic trigger that requires good hits in BC1 and BC2 (the target upstream beam counters) and no hit in the beam halo veto counter V-BC. This trigger essentially selects events where a beam ion hits the target.

AndSRC and *OrSRC* triggers: Adds to the *beam* trigger a requirement for a signal in the TAS scintillator counters (X and Y). The '*AndSRC'* trigger requires signals in both the left and right TAS arms while the '*OrSRC'* trigger requires signals in either arm.

Physics data were taken requesting the *AndSRC* trigger at a rate of about 180 Hz as measured during a beam pulse duration. Under these conditions the measurement live-time was close to 100%.

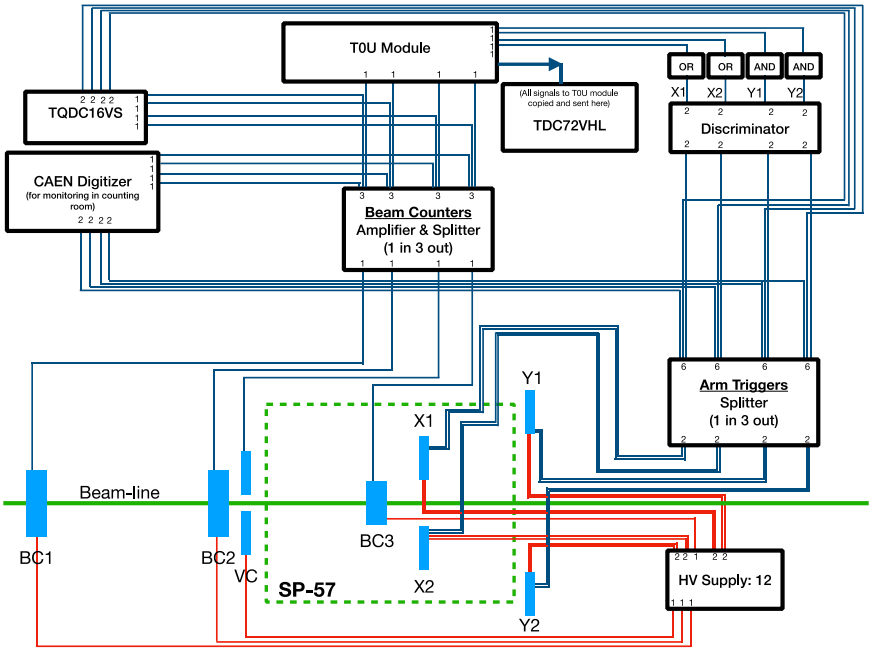

Fig. 2.1: Trigger system readout.

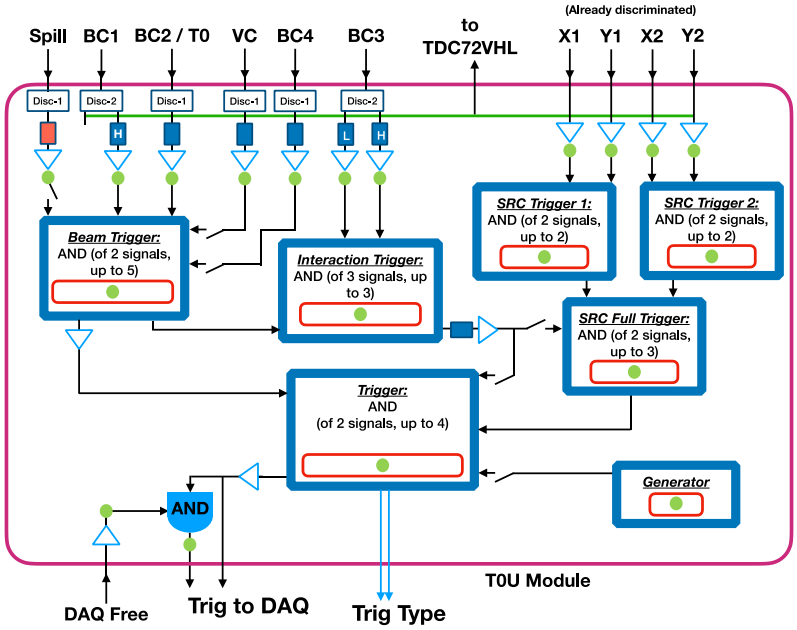

Fig. 2.2: Configurable T0U module responsible for triggering DAQ readout, showing the different input signals and the coincidence units.

3. Beam Counters

The beam ions are identified on an event-by-event basis using their energy loss signal in the BC detectors (BC1, BC2 upstream the target) that is proportional to their nuclear charge squared Z^2. The QDC signals from the scintillator beam counters BC1, BC2, BC3, BC4 were read and the pedestals were subtracted. Events with timing signal outside of the main time peak were rejected as well as events with multiple hits in BC2.

3.1 Incoming Charge Z

The BC1 and BC2 scintillators are used for monitoring the incoming beam. The incoming beam consists of C, N, and O nuclei. The signal amplitude is proportional to the energy loss. The different beam species can be identified in Fig. 3.1. We apply a 2D cut as indicated to select the incoming carbon ions in the analysis. The positions of BC1,2 amplitude peaks over the data taking time was slightly shifting. That was taken into account in the incoming selection.

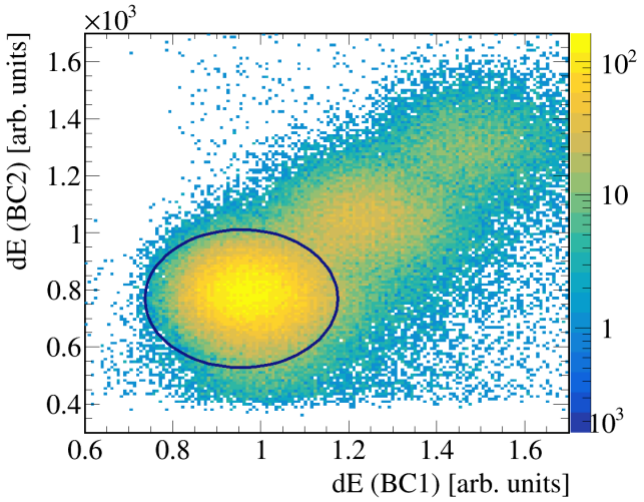

Fig. 3.1: Incoming charge identification. The selection of 12C is indicated by the blue ellipse, the other contaminants are 14N and 16O.

3.2 Outgoing Charge Z

The charge identification of the fragment after the target is done using the energy deposition in the two scintillator-based beam counters BC3 and BC4, placed between the target and the magnet entrance. Their amplitudes are proportional to the sum over all fragment charges squared, $Z_{eff} \equiv \sqrt{\sum Z^2}$. The outgoing beam includes elements from C to H, see Fig. 3.2, the selection of Boron isotopes is indicated. We also observed a dependence of the signal height as function of run time. That drift is apparent in Fig. 3.3, shown for the geometric mean using the BC3 and BC4 amplitudes $\sqrt{A(BC3) * A(BC4)}$, i.e. the Z_{eff} peak. That drift was taken into account by a run-dependent selection of the outgoing charge.

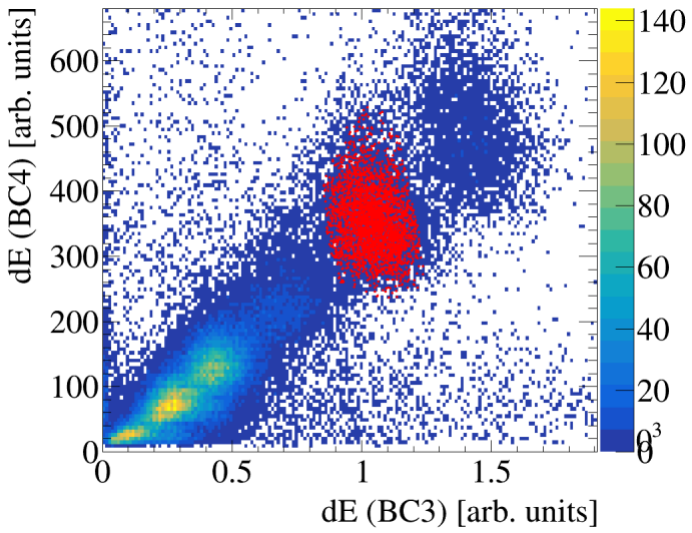

Fig. 3.2: Fragment charge identification behind the target. The selected Boron events are shown in red.

3.3 Efficiency

The efficiency for incoming and outgoing charge identification using the BCs is done by analyzing empty-target data with Z = 6. For the charge efficiency measurement we consider the energy loss in BC1,2 for the incoming fragment Zin, and BC3,4 for the outgoing fragment Zout. Figure 3.4 (left) shows the energy loss in BC2 vs. BC1 for the empty target run. The ellipse shown defines the Zin = 6 cut. Figure 3.4 (right) shows the energy loss in BC4 vs. BC3 after a cut on Zin = 6. We tried different cuts shown by the ellipses in the region of (2−3)σ, in order to get an averaged value for the efficiency and its uncertainty

$$\varepsilon_Z = \frac{\#(Z_{in} = 6 \,\&\, Z_{out} = 6)}{\#(Z_{in} = 6)} = (83 \pm 6)\%.$$

We adapt this value for outgoing charge Zout = 4,5.

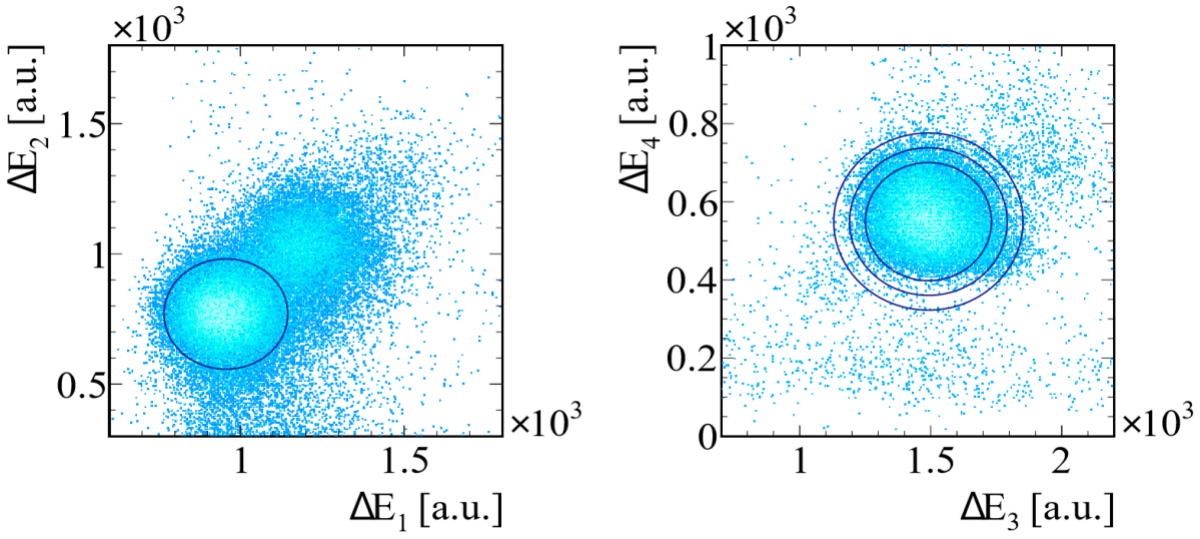

Fig. 3.4: Left: Energy loss in BC2 vs. BC1 for an empty target run. The ellipse sown defines the Zin = 6 cut. Right: Energy loss in BC4 vs. BC3 for events with Zin = 6. The different ellipses define different cuts on Zout = 6.

4. Beamline tracking detectors (MWPCs and Si):

4.1 MWPC: Calibration and Track Identification

Prior to hitting the target, the beam was tracked by two MWPCs mentioned above, they comprise Pair 0. Two more such MWPCs were located downstream the target making up Pair 1 (Fig. 4.1). Each MWPC consists of six planes located sequentially along the Z axis at a distance of 1 cm. In each plane the wires are oriented along X, U, or V axis, so that there are two X, two U, two V planes in each chamber. The coordinate axes X, U, V are oriented at an angle of 60 degrees relative to each other. The coordinates are related as X = U + V.

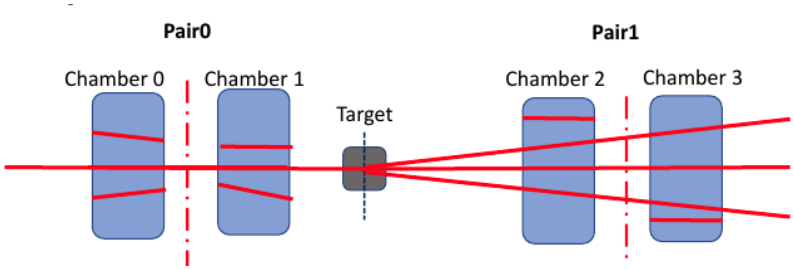

Fig. 4.1: MWPC location in the experimental setup.

The tracks in MWPCs were reconstructed as the following:

1. The fired wires were read out in each plane and combined into clusters. A cluster is a group of neighboring fired wires. The cluster size in each chamber is presented in Fig. 4.2. The cluster coordinate (called a point) is defined by the wire with the local time minimum in a group of neighboring fired wires in a given plane.

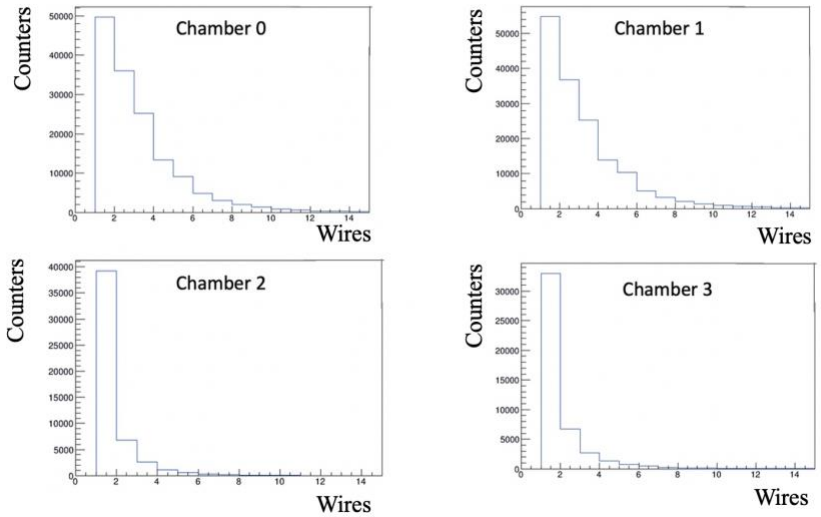

Fig. 4.2: The cluster size in each chamber. Data from run 3430, empty target.

2. The spatial hit is defined by three points in X, U, and V planes that satisfy the condition: $| U + V – X | = 3 * dw$,
   where dw = 0.25 cm is the wire pitch.
3. The reconstructed tracks within one chamber are formed using one spatial hit and points in the next three planes of the same chamber within the corridor of 3*dw. Tracks having the highest number of points are searched first. The maximum possible number of points for a track within one chamber is 6. The minimum accepted number of points is 4. Each track candidate is fitted with a straight line. The set of tracks in each chamber

in a given event is sorted according to χ^2 criterion. The number of points for the reconstructed tracks within one chamber is shown in Fig. 4.3.

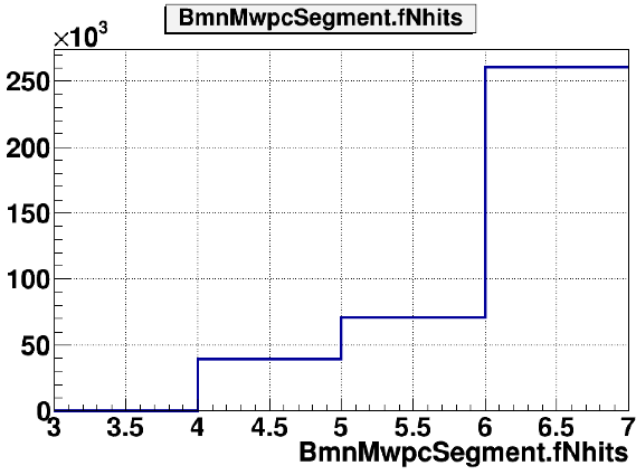

Fig. 4.3: The number of points for the reconstructed track candidates within one chamber. Data from run 3430, empty target.

4. Each track candidate for MWPC0 and MWPC1 comprising Pair 0 (and separately for MWPC2 and MWPC3 comprising Pair 1) is extrapolated to a defined z position Z_{Pair_i} (Z_{Pair0} = -809 cm and Z_{Pair1} = -275 cm). The resulted coordinates of the extrapolation are compared, the matched pairs of tracks are ranged by χ^2-criterion (angles of tracks are not considered in this selection). The χ^2- is calculated by the formula $\frac{dx^2}{\delta x^2} + \frac{dy^2}{\delta y^2}$, where $\delta x = \delta y$ = 0.7 cm. The tracks with χ^2 less than 100 were accepted.

5. The reconstructed tracks going through two chambers are fitted by straight lines and ranged by χ^2 criterion. The maximum possible number of points for a track passing through a pair of chambers is 12, the minimum accepted number of points is 8.

The reconstructed track parameters (X and Y coordinates at the Z_{Pair_i} between two chambers comprising Pair 0 or Pair 1, the track direction in terms of angle (tangent) in XZ and YZ planes are shown in Fig. 4.4 for Pair 0, and in Fig. 4.5 for Pair 1. The data are for run 3430, empty target (for events with charge 6). The difference in position reflects the beam (de)focusing.

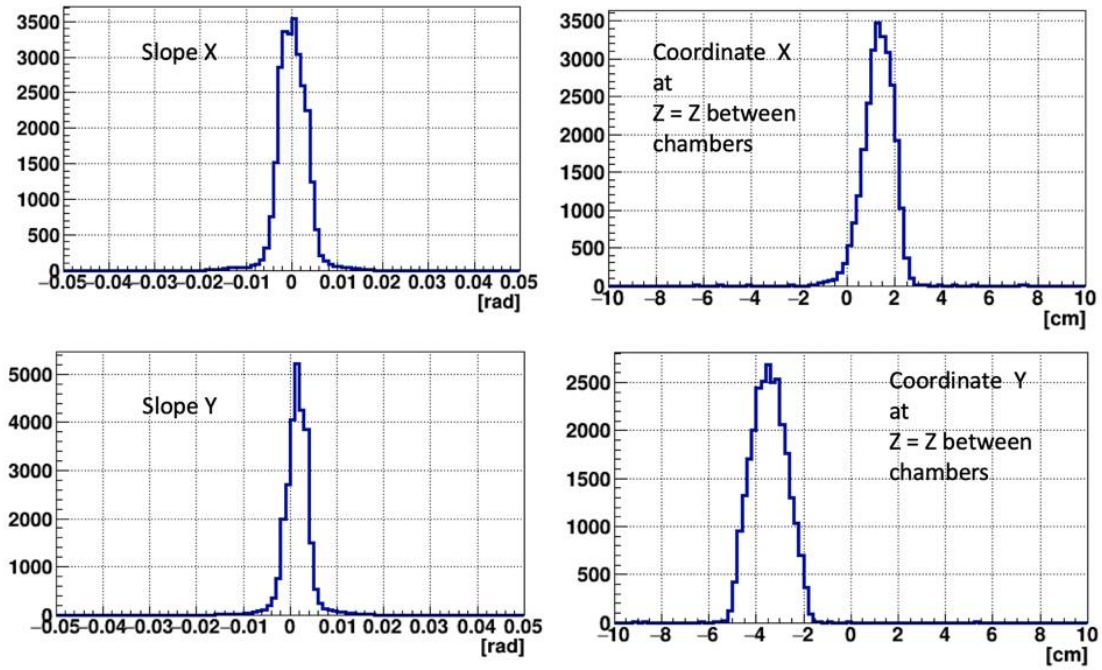

Fig. 4.4: The reconstructed track parameters for Pair0, at Z_{Pair0} = -809 cm. Data are for run 3430 with an empty target. Events selected with incident carbon.

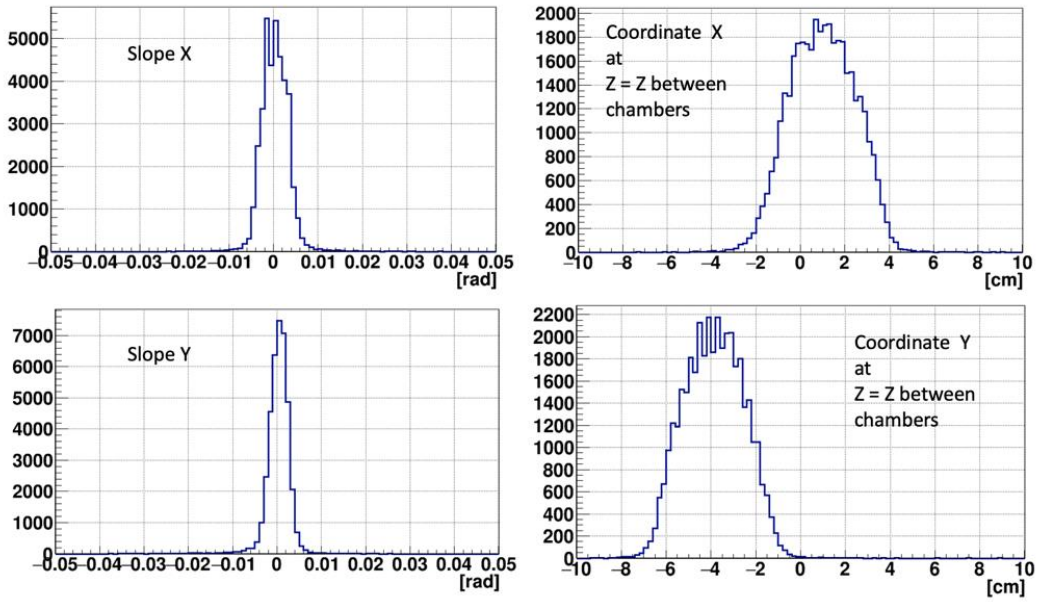

Fig. 4.5: Same as Fig. 4.4 for Pair1, at Z_{Pair1} = -275 cm.

The reconstructed beam profile at Z_{Pair0} = -809 cm is shown in Fig. 4.6(left) for run 3430, empty target, and events with incident charge of 6. Figures 4.6(center) and 4.6(right) show the beam profile from Pair 1 for empty target data and LH2 target data (with total outgoing charge 5).

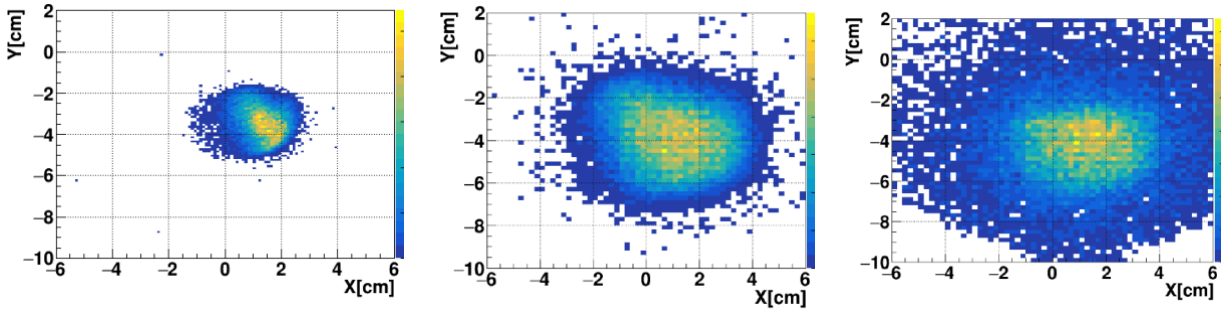

Fig. 4.6: Left: The beam profile at Z_{pair0} = -809 cm in Pair 0. Data are for run 3430 with an empty target, incoming charge of 6. Center: Same for Pair1 at Z_{Pair1} = -275 cm. Right: Beam profile at Z_{Pair1} = -275 cm in Pair 1. Data are for run 3338 with the LH2 target. Events were selected with the incoming charge of 6 and outgoing 5.

Figures 4.7 and 4.8 show the matching between Pair 0 and Pair 1 at the center target position Z_{target} = -645 cm for an empty target run. The plots show the coordinate difference between the extrapolated tracks from Pair 0 and Pair 1 at that z position, which is a measure of spatial resolution. The sigma value of a fit to these distributions for X is 0.37 cm and for Y is 0.36 cm. The design detector coordinate resolution is 0.72 mm for X coordinate and 1.1 mm for Y coordinate. The angular width (Fig. 4.8) is tan(dX) = 1.6 mrad and tan(dY) = 1.7 mrad (sigma).

While the z-position (along the beamline) of the reaction vertex is reconstructed from two tracks in the TAS, the (x,y) position is obtained from the extrapolated MWPC track in front of the target (when available) since this system provides a better transverse position resolution.

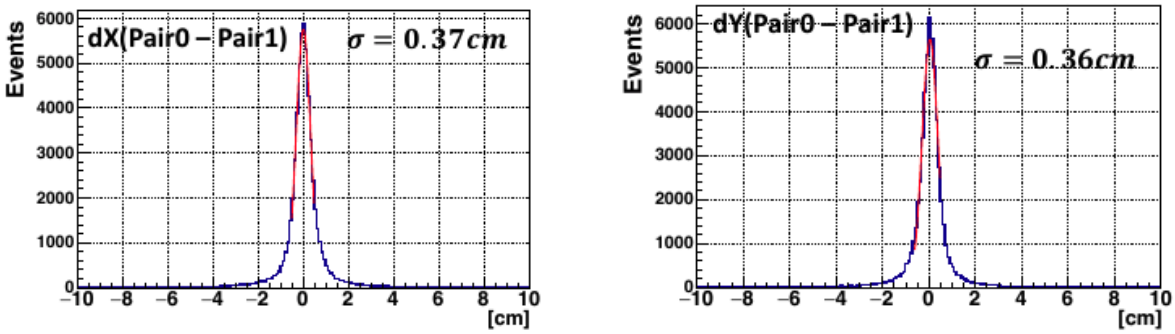

Fig. 4.7: The coordinate difference between the extrapolated tracks from Pair 0 and Pair 1 at the Z target. Data are for run 3430 without a target. Sigma X = 0.37 cm, sigma Y = 0.36 cm.

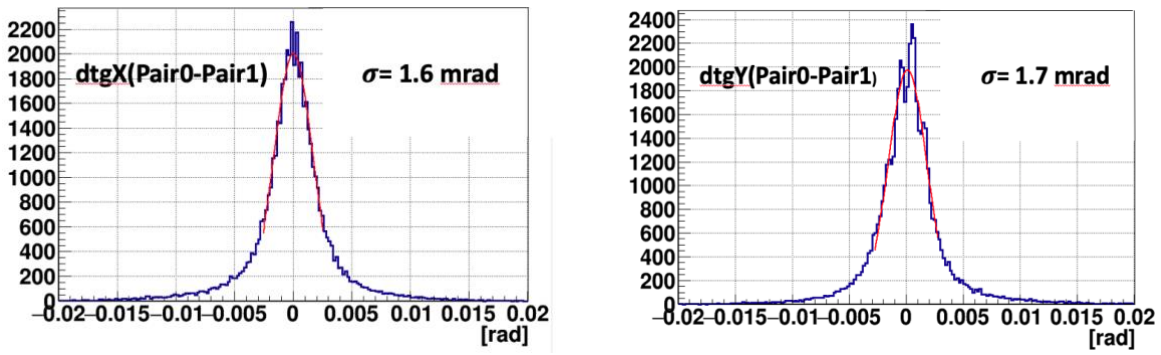

Fig. 4.8: Same as Fig. 4.7 for the difference between the reconstructed angles from Pair 0 and Pair 1. Sigma X = 1.6 mrad, sigma Y = 1.7 mrad.

4.2 Si: Calibration, Tracking, Resolution

Additionally to the MWPCs, three silicon detectors were located between the target and the analyzing magnet as shown in Fig. 4.9. The Si 1 and Si 2 were located at Z = -428 cm within the same housing, therefore the distance between them is only 4 cm. The third station Si 3 had a separate housing and was placed at Z = -314 cm.

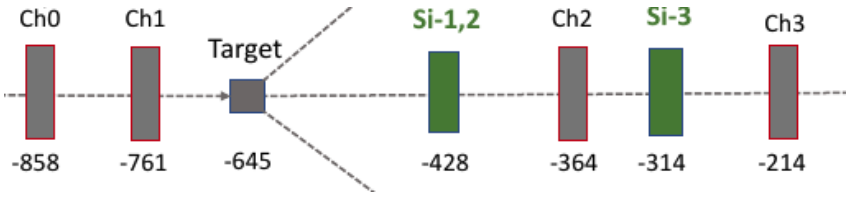

Fig. 4.9: Silicon Detectors location in the experimental setup.

Each silicon detector has two coordinate planes: the vertical X strips and X' strips tilted by 2.5° relative to the X strips. For the collected data the readout from the X' strips was not always efficient, which was accounted for in the reconstruction:

1. The fired strips in each plane are combined into clusters. The cluster is a group of neighboring fired strips in a given plane. The cluster coordinate is calculated using the center of gravity $CoG = \frac{\sum_{i=0}^{n} A_i * i}{\sum_{i=0}^{n} A_i}$, where A_i is the amplitude of the strip number i.

2. The track recognition is carried out in the corridors dX = 7 mm, dX' = 11 mm using the 4 cases shown in Fig. 4.10. The spatial points (based on X and X') and individual signals from X or X' separately (hits) are used to find a track.

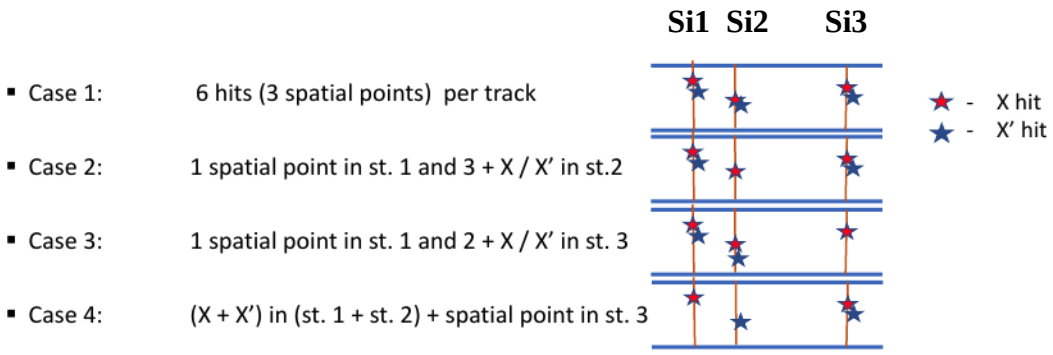

Fig. 4.10: Possible combinations of X and X' signals for track reconstruction algorithm using the data from the 3 Si detectors.

3. The hits and points attributed to a track are fitted by a straight line. Each track is checked to originate in the target area. Only the tracks extrapolated to the target area were accepted. The reconstructed tracks are ranked by χ^2 criterion. The Y coordinate is calculated as $Y = \frac{X'-X}{tg2.5°}$.

The distribution of the number of hits and points for Silicon tracks is shown in Fig. 4.11.

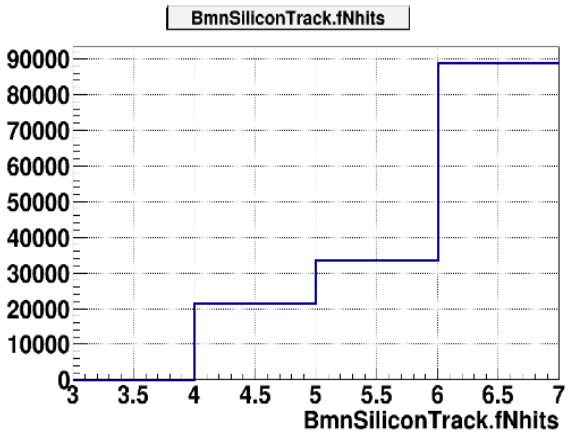

Fig. 4.11: The number of hits and points in Silicon tracks. Data are for run 3430, empty target.

The reconstructed track parameters including X and Y coordinates at the Z = -371 cm (an average Z position for 3 Silicon stations) and the direction in terms of tangents in XZ and YZ planes are also shown in Fig. 4.12. Data are for the empty target run 3430. The reconstructed beam profiles are shown in Fig. 4.14. The silicon detector Si 3 at Z = -214 cm consists of two modules located one above the other (see Fig. 4.15) which causes a gap in the Y direction. This feature propagates to the Y-coordinate distribution of the reconstructed Si tracks (see Fig. 4.12). The location of the individual modules within the Silicon stations is shown in Fig. 4.13.

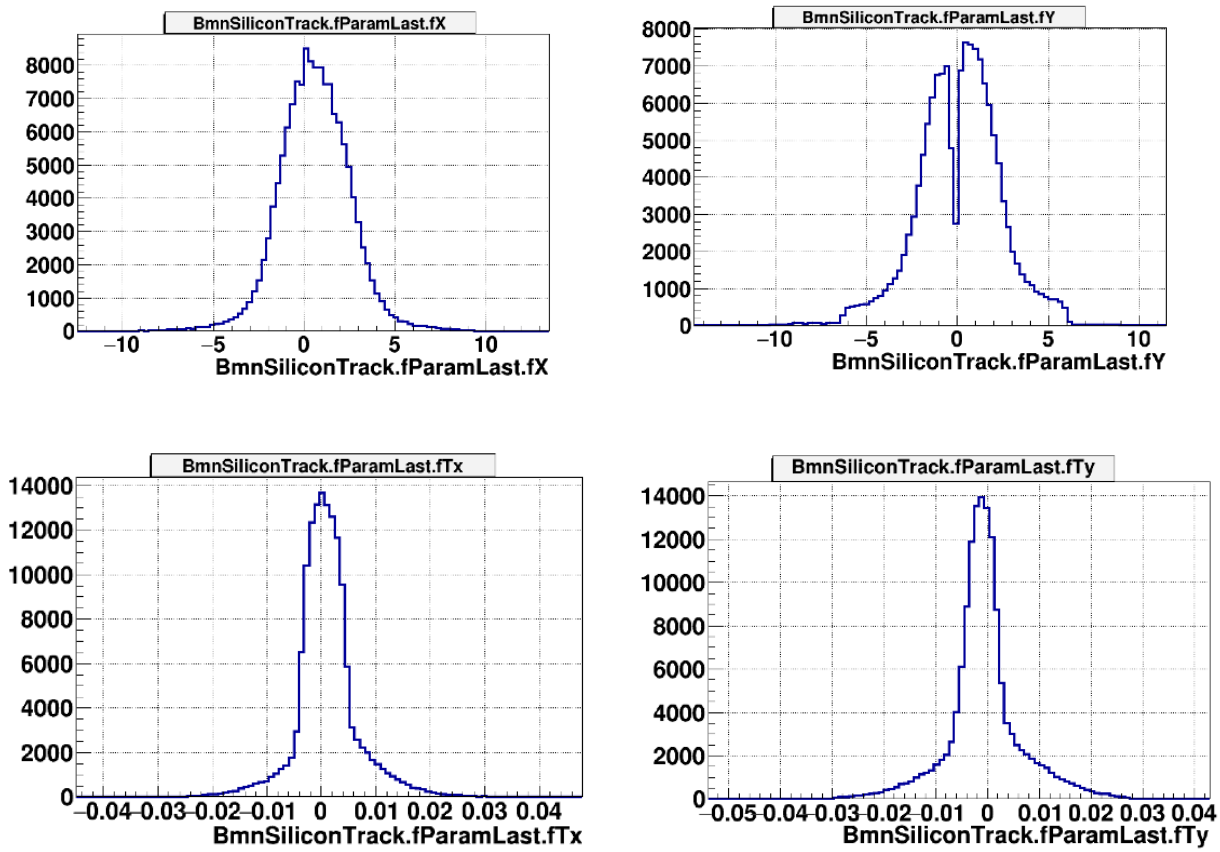

Fig. 4.12: The silicon reconstructed coordinates (x, y) and angles (Tx, Ty) at Z = -371 cm. Data are for run 3430, empty target.

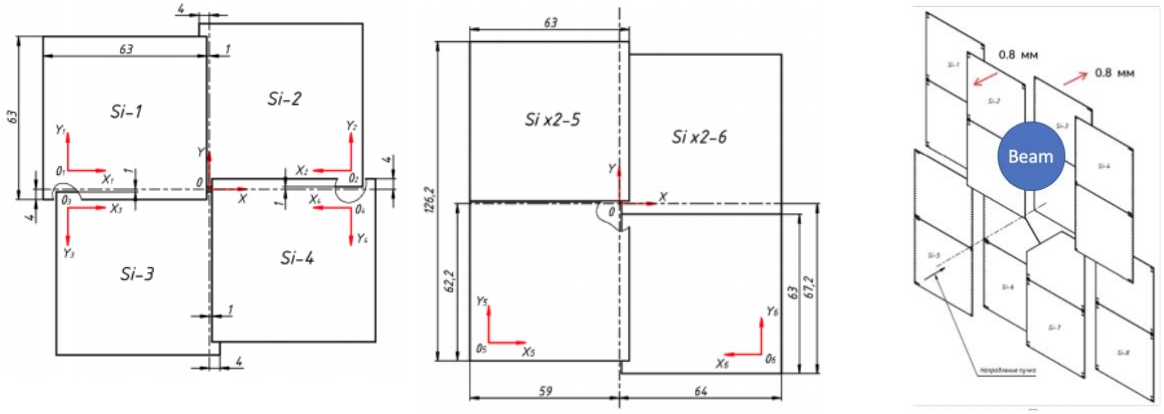

Fig. 4.13: The location of the modules in the Silicon stations at Z = - 428 cm (left), - 424 cm (center), - 314 cm (right). A triangular hole in the Si 3 station (right) was below the beam and did not affect the track measurement.

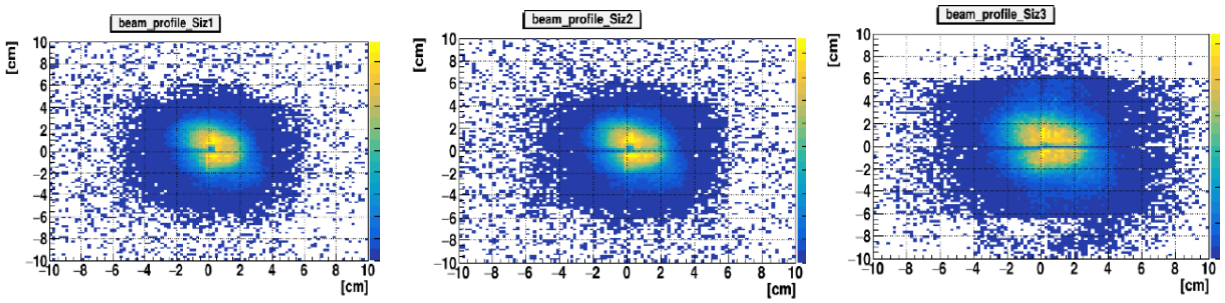

Fig. 4.14: The reconstructed beam profile at Z = - 428 cm (left), - 424 cm (center), - 314 cm (right). Data are for the run 3430, empty target.

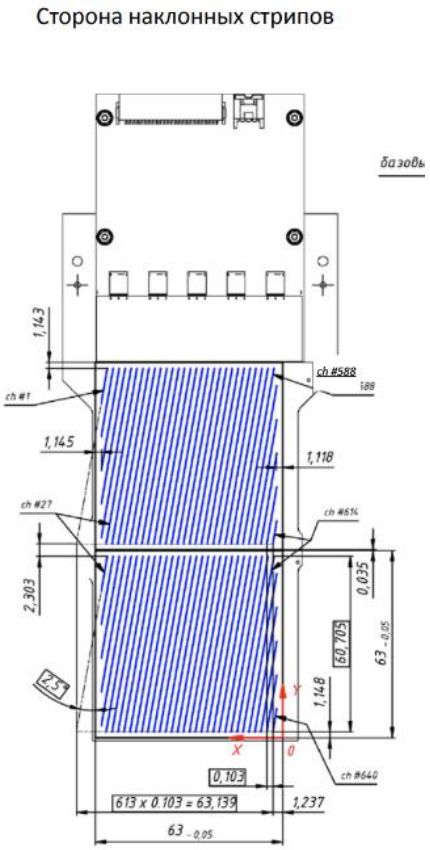

Fig. 4.15: The technical drawing for the Si 3 detector. The upper and lower modules are separated by a gap. The X' strips of the upper part are shifted relatively to the X' strips of the lower part by 2 mm.

4.3 Combined upstream Tracking

Three silicon (Si) planes and two MWPCs are placed in the beam-line downstream the target to measure the fragment scattering angle. The combined tracks from the MWPCs and Si were reconstructed in the following way.

1. The silicon tracks are extrapolated to the Z = -271 cm between the proportional chambers of Pair 1 where they are matched to the MWPC tracks by coordinates and angles. The matching criteria are: angular difference of less than 0.02 mrad in X (Y) and X (Y) coordinate difference of less than 15 (20) mm.
2. The silicon tracks that were not matched in step 1 are matched to individual track-segments in each proportional chamber of Pair1.
3. The best combinations after fitting are selected by a χ^2-criterion. The differences of coordinates and angles between the Silicon tracks and MWPC tracks at Z = -271 cm are shown in Fig. 4.16.

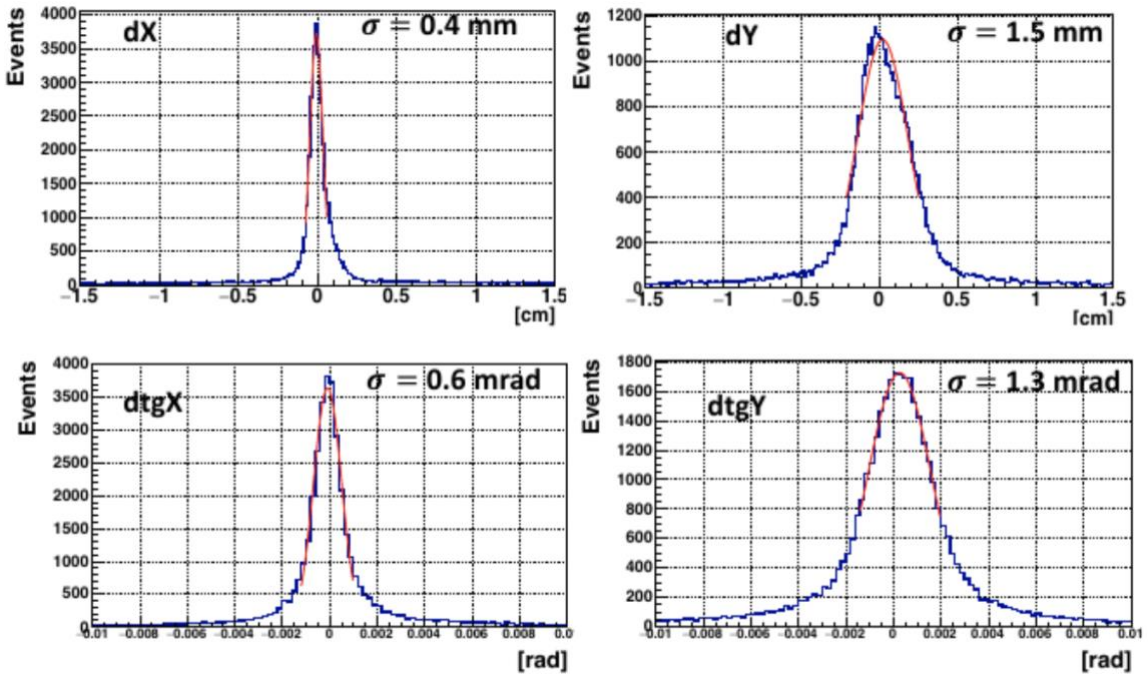

Fig. 4.16: The difference of coordinates (dX, dY) and angles (dtgX, dtgY) between the Silicon tracks and MWPC tracks at Z = -271 cm. Data are for the run 3430 (empty target).

The residuals and standard deviation for the combined tracks with respect to the single detectors are shown in Tab. 4.1.

Tab. 4.1: Track residuals for the combined Si-MWPC tracks

	1 st SiDet	2 st SiDet	3 st MWPC	4 st SiDet	1 st MWPC
X Mean[mm]	0	0	0.07	0	0.10
X Sigma[mm]	0.018	0.021	0.46	0.011	0.49
Y Mean[mm]	0.021	-0.021	-0.02	0.02	0.01
Y Sigma[mm]	0.75	0.84	0.55	1.36	0.16

4.4 Tracking Efficiency

The reconstruction efficiency of the MWPC detector system was calculated relative to the scintillator counters BCs.

The average efficiency of the MWPC pair in front of the target for particles with the charge of 6 is (92.2±0.1)%. The efficiency as function of run number is shown in Fig. 4.17. The deviations in efficiency don´t affect the analysis, the efficiency is not used for any correction. It was calculated relative to BC1,2 like

$$\frac{MWPCPair0 \wedge Cin}{Cin}$$

The numerator is the number of events containing at least one MWPC track and incident carbon. The denominator is the number of events with an incident carbon as defined by the energy deposition in the scintillator counters.

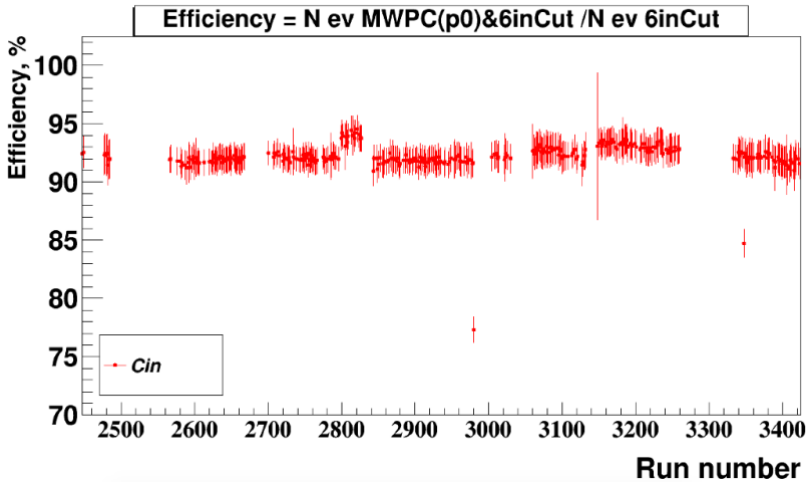

Fig. 4.17: The MWPC Pair 0 (in front of target) efficiency for the production runs. The efficiency with incident and outgoing carbon is (92.2 ± 0.1)%

The average efficiency of the MWPC pair1 after the target is (88.8±0.7) % for ions with Z = 6, and (89.1±0.2)% for ions with Z = 5. The efficiency for the production runs is shown in Fig. 4.18. The deviations in efficiency don´t affect the analysis, this particular efficiency is not used for any correction. The reconstruction efficiency for MWPC Pair 1 was calculated relative to BC1,2 and BC3,4. The numerator is the number of events containing at least one MWPC Pair1 track assuming incident and outgoing carbon (boron) and more than zero MWPC Pair 0 tracks. The denominator is the number of events with incident and outgoing carbon (boron) and at least one track in MWPC Pair 0. In particular, the efficiency for MWPC Pair 1 was calculated like

$$\frac{MWPCPair1 \wedge IonCut \wedge MWPCPair0}{IonCut \wedge MWPCPair0}.$$

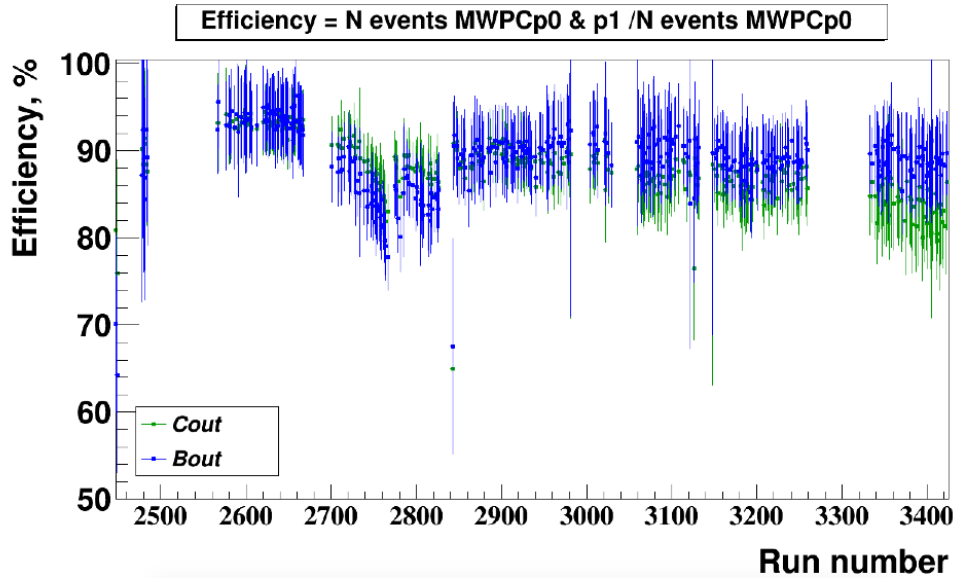

Fig. 4.18: The MWPC Pair1 efficiency for the production runs with different outgoing charge cuts. The averaged efficiency is (88.8±0.7)% for ions with outgoing Z = 6, and (89.1±0.2)% for ions with Z = 5.

The Si reconstruction efficiency for several runs is shown in Fig. 4.19. The deviations in efficiency don´t affect the analysis, this particular efficiency is not used for any correction. The numerator is the number of events containing at least one Si-track assuming a particular incident and outgoing ion and at least one MWPC Pair 0 track. The denominator is the number of events with a particular incident and outgoing ion and at least one track in MWPC Pair 0. The efficiency of the Si system was calculated like

$$\frac{Si \wedge IonCut \wedge MWPCPair0}{IonCut \wedge MWPCPair0}.$$

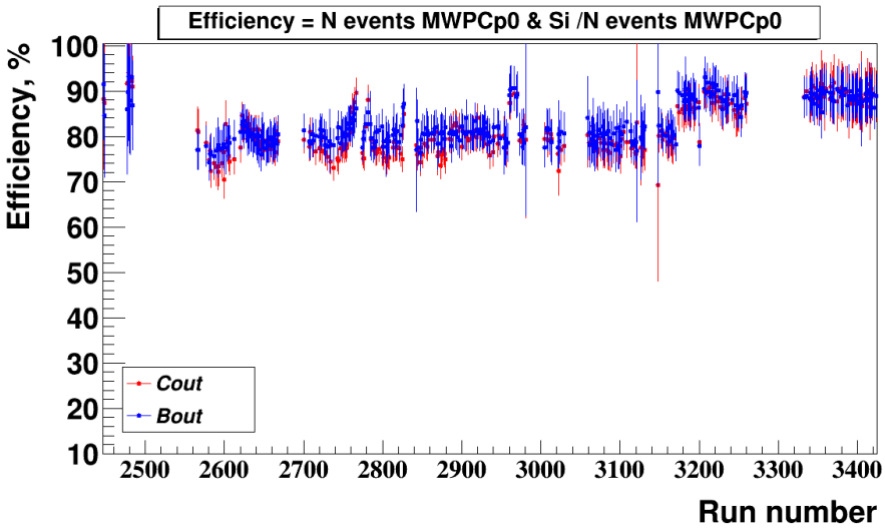

Fig. 4.19: The Silicon efficiency for production runs for incident carbon and different outgoing ions. The average efficiency is (81.5±0.7)% for ions with outgoing Z = 6, and (82.6±0.7) % for ions with outgoing Z = 5.

Combined upstream tracks after the target were reconstructed using information from the MWPC pair after the target and the Si detectors. The numerator is the number of events containing at least one track in Si or MWPC Pair 1 or a combined track, and at least one MWPC Pair 0 track assuming a particular incident (carbon) and outgoing ion. The denominator is the number of events with at least one MWPC Pair 0 track assuming a particular incident (carbon) and outgoing ion. The charge was determined with BC1,2 and BC3,4 respectively. The efficiency for combined tracks was calculated as

$$\frac{(Si \vee Pair1 \vee (Si \wedge Pair1)) \wedge IonCut \wedge Pair0}{IonCut \wedge Pair0}.$$

The results are shown in Fig. 4.20, it is flat as function over run time as it contributes to the overall fragment tracking efficiency.

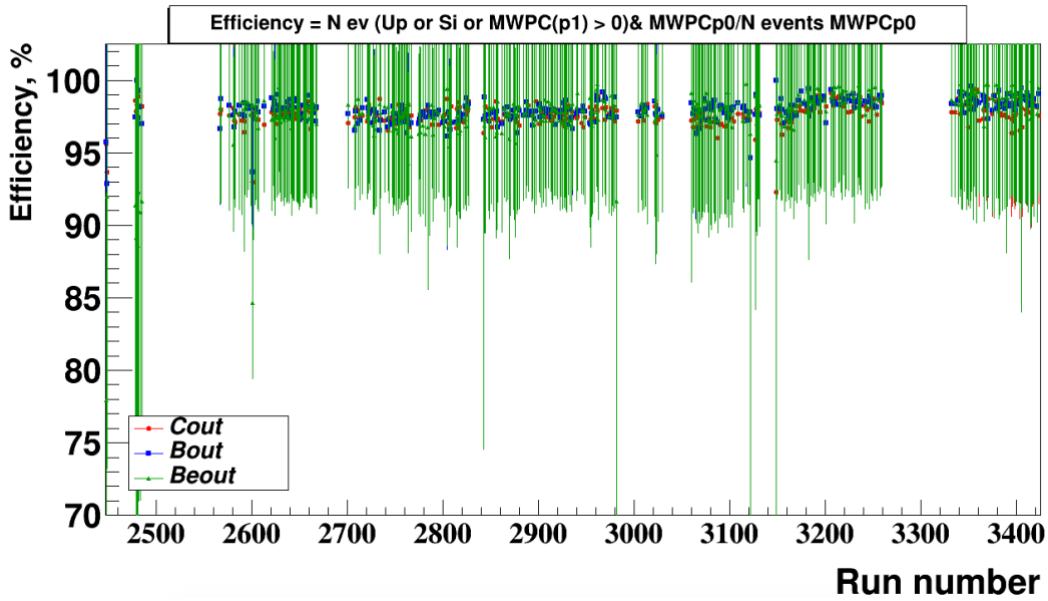

Fig. 4.20: The efficiency for upstream combined tracks for the production runs, an incident carbon and different outgoing ions. The average efficiency is (97.7±0.2)% for ions with Z = 6, (97.9±0.3)% for Z = 5 and (97.7 ± 0.3)% for Z = 4.

5. Two-Arm Spectrometer (TAS)

The two-arm spectrometer (TAS) was placed downstream of the target to detect the two protons from the (p,2p) reaction that emerge at about 90° QE scattering in the two-protons c.m. frame. Each spectrometer arm consisted of scintillator trigger counters (TC), gas electron multiplier (GEM) stations, and multi-gap resistive plate chamber (RPC) walls.

We describe the proton track reconstruction using their hit location in the GEM and RPC walls, the interaction vertex (reconstruction, resolution, cuts), the pion rejection, and momentum determination.

5.1 Vertex Reconstruction

The z-position (along the beamline) of the reaction vertex is reconstructed from two tracks in the TAS, while the (x,y) position is obtained from the extrapolated MWPC track in front of the target. The reaction vertex is reconstructed whenever one particle track is reconstructed in each arm of the TAS. This requires at least one hit in the GEM and RPC systems to form a linear track in each arm. We consider only single-track options from the hit combinations. The coincident two tracks that come closest, formed from all possible hit combinations, determine the vertex position along the beamline in the z direction.

Most events considered in our analysis (80%) have hit multiplicity of 1 in each detector, where a hit is a cluster determined by the BM@N tracking algorithm. The multiplicity distribution in the different detectors for our meanfield QE physics events looks like:

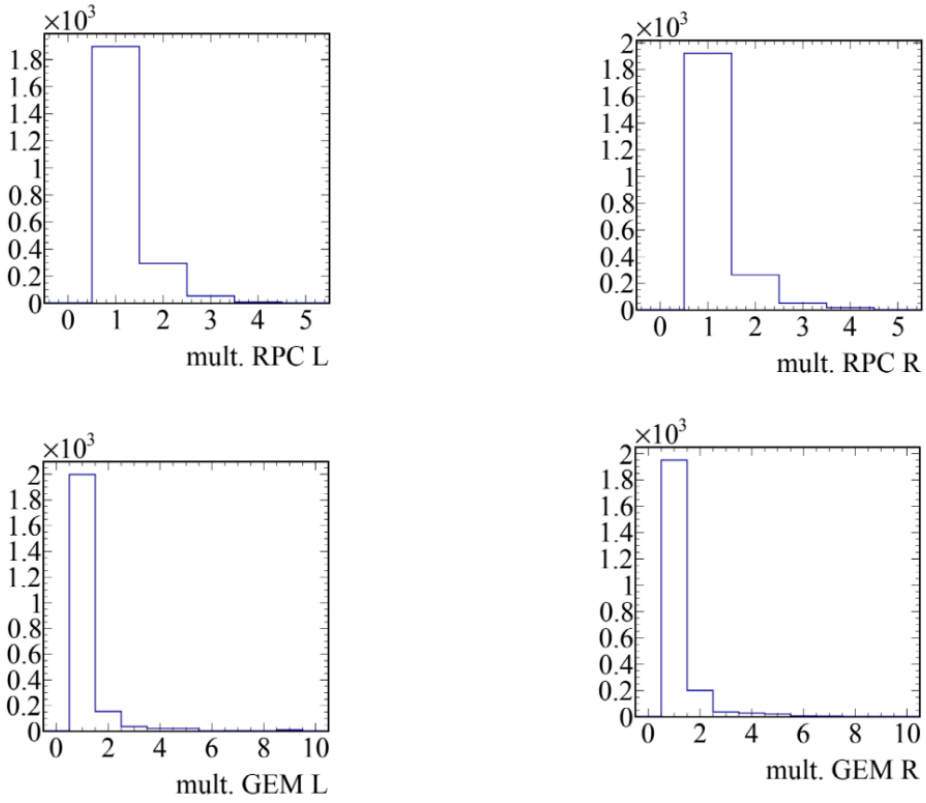

Fig. 5.1: Multiplicity distribution for RPC (top) left (L) and right (R) arm, and GEM (bottom) left and right.

For the remaining 20% of events with more than one hit, we choose the 'correct' track as the one that results in the smallest distance between the left and right arm tracks intersection, which is obtained from a minimization of

$$D^2 = (x_l - x_r)^2 + (y_l - y_r)^2 + (z_l - z_r)^2$$

$$dD^2 = \frac{\delta D^2}{\delta z_l} dz_l + \frac{\delta D^2}{\delta z_r(z_l)} dz_r(z_l) = 0$$

The algorithm follows this scheme:

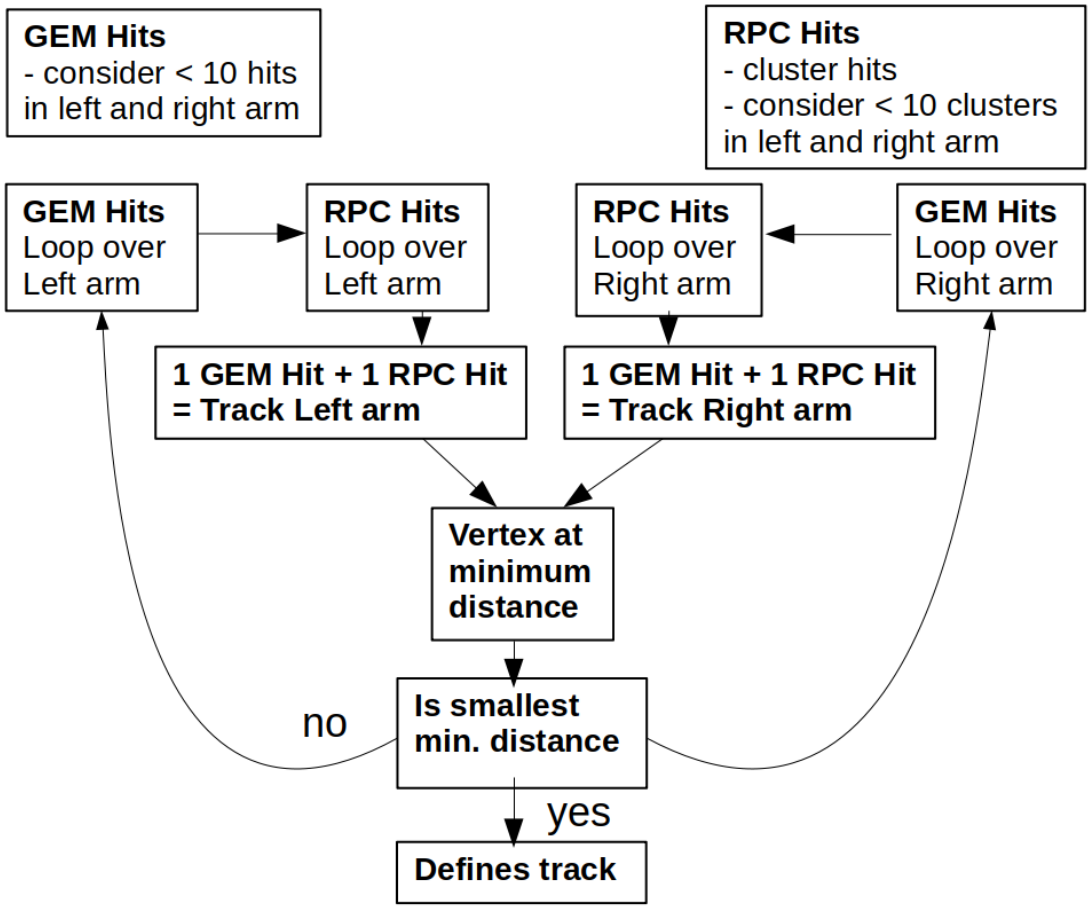

Fig. 5.2: Vertex reconstruction scheme.

The vertex quality is ensured by requiring that the minimum distance between the two tracks, which define the vertex, is smaller than 4 cm, see Fig. 5.3.

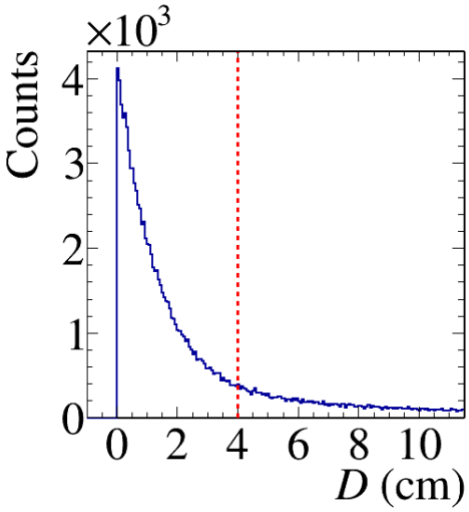

Fig. 5.3: Vertex minimum distance and cut. See text for details.

When there is more than one vertex combination, the distance between the second smallest approach and the minimal approach vertices is often still within our 4 cm condition, it looks like:

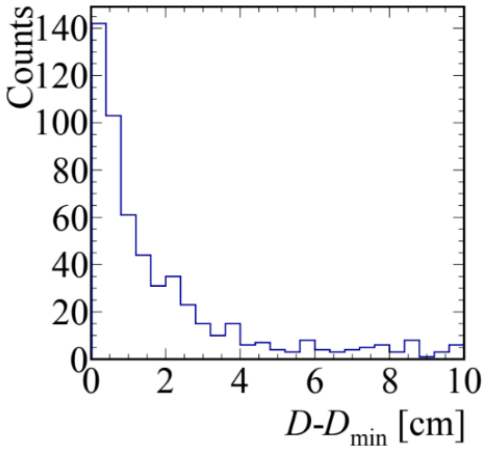

Fig. 5.4: Minimal distance difference to second smallest D.

We examined what would happen if we choose the 2nd best track that still satisfies the 4 cm difference cut which we apply in the data analysis process. No visible impact is seen because these tracks are essentially the same and result from small 'leftovers' of the clustering algorithm. The difference in their momentum follows a Gaussian distribution with sigma <5 MeV/c. Similarly,

their angles are practically identical. The momentum difference between minimal approach vertex and the second closest approach vertex with (D-D_{min}) < 4 cm:

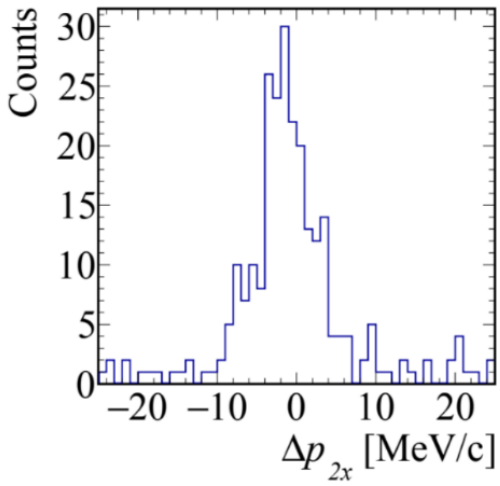

Fig. 5.5: Momentum difference, between D_{min} and the second closest approach extraction. Shown for example is the p_x of the right arm.

The overall the track reconstruction efficiency is 40%, given the smaller angular coverage of the RPC system compared to the GEMs and detector inefficiencies, with an RPC detection efficiency of about 85%. The latter was extracted from coincident hits in overlapping RPC modules.

5.2 Alignment Procedure

Before discussing the momentum analysis, we present below the calibration of the tracks. Alignment procedures within the GEM-RPC system, the left and right arm, as well as relative to the incoming beam are applied. The detector positioning relies on a laser-based measurement, and the alignment relative to the other detector systems using experimental data, obtained with the beam on. We did perform the alignment using data taken with a single 9 mm Pb target:

1. Alignment of full (GEM-RPC) system relative to MWPC vertex by introducing shift in x and y to GEM and RPC.

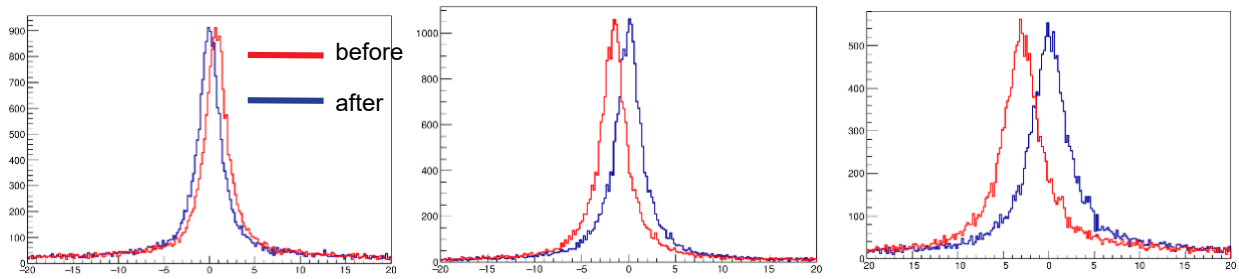

Fig. 5.6: Alignment of full (GEM-RPC) system relative to MWPC vertex, before and after correction. Left: vtx,X – MWPC0,X. Center: vtx,Y – MWPC0,Y. Right: vtx,Z.

2. Alignment of separate RPC planes by extrapolating the track, determined from the vertex and GEM, to the RPC z hit and aligning the x,y difference to the actual hit.

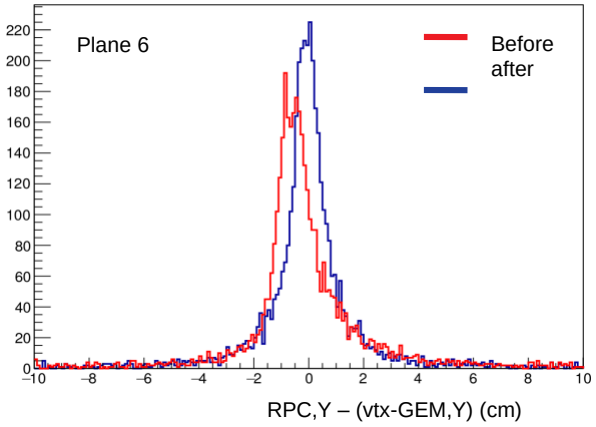

Fig. 5.7: Alignment of separate RPC planes, example for plane 6 in y position, before and after correction.

3. Left-Right Arm Alignment. We employ physics data with LH2 target and basic proton selection cuts including the beta cut, opening angle cut, and missing mass cut around the proton mass. In order to match the momentum sum p1+p2 (left+right arm) at zero the complete TAS is rotated together in space in x and y.

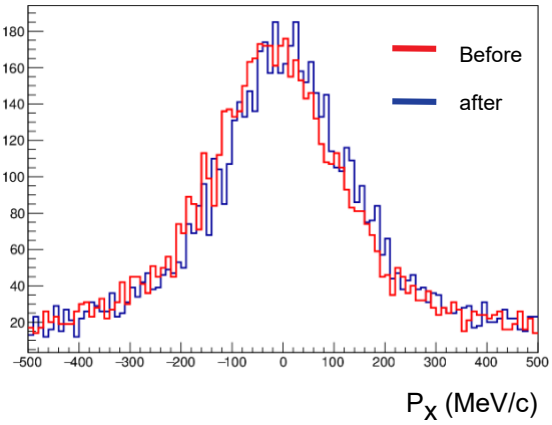

Fig. 5.8: Rotating arms to center momentum distribution, example for p_x.

The results of this calibration manifests in the position resolution in z that was determined by looking to calibration data taken with three Pb foils separated by 15 cm placed at the target position. The reconstructed vertex position is shown in Fig. 5.9 below, clearly three distinct peaks at a distance of 15 cm representing the Pb foils, are reproduced. Given the width of each peak, the z-position resolution from the two-arm spectrometer is on average 1.8 cm (1σ).

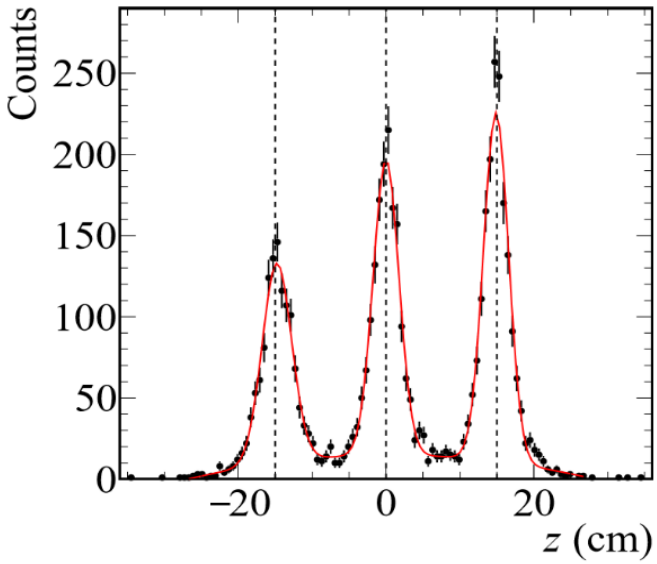

Fig. 5.9: Vertex in z direction for 3 Pb foils at the target position to determine the position resolution of the vertex reconstruction. The position resolution is 1.8 cm (1σ), the fit is shown by the red line (plus background). The dashed black lines indicate the absolute position alignment at z = ±15 cm and zero

When reconstructing the vertex position along the z-direction with LH2 target, we nicely reproduce the target volume and surrounding structures, see Fig. 5.10.

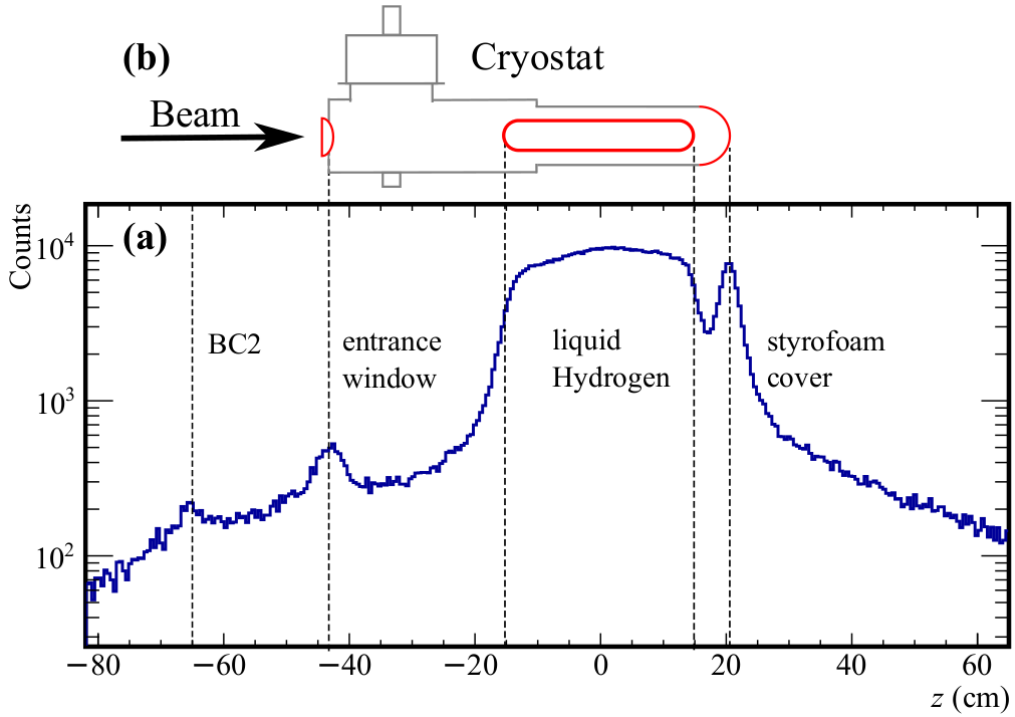

Fig. 5.10: Reconstructed reaction vertex in the LH2 target. The position along the beam line is shown in (a), scattering off in-beam material is also visible. For comparison, a sketch of the target device is shown in (b), scattering reactions are matched at the entrance window, the target vessel, styrofoam cover. A selection of |z| < 13 cm is applied to reject such reactions.

5.3 Time-of-Flight Calibration and resolution

Knowing the vertex and the position in the RPC, the flight length and angle is determined. In order to obtain the momentum, the time-of-flight information needs to be added, which is measured between the t0 and RPC.

T0 Resolution

First, the T0 detector was calibrated absolutely for time-walk and its resolution was extracted. A special, low-luminosity run was performed with two additional fast-timing detectors (T02, T03) in the beamline. The two additional detectors were of similar construction as T0. The beam was measured in all three detectors and the resolution of our T0 can be extracted by combining pairs of detectors (cf. Fig. 5.12):

$$t_{T0} - t_{T02} \rightarrow \sigma^2_{T0+T02} = \sigma^2_{T0} + \sigma^2_{T02}$$

$$t_{T0} - t_{T03} \rightarrow \sigma^2_{T0+T03} = \sigma^2_{T0} + \sigma^2_{T03}$$

$$t_{T02} - t_{T03} \rightarrow \sigma^2_{T02+T03} = \sigma^2_{T02} + \sigma^2_{T03},$$

where we have three equations with three unknowns, and we're most interested in σ^2_{T0}. To extract the resolution, we first need to correct T0 detector for time-walk variation. This was done by first cutting tightly on waveform amplitude in T02 and T03 in order to ignore time-walk effects in T02 and T03, and then characterizing and correcting T0 for time-walk variation. T02 (or FFD) is an MCP-PMT detector with 4 independent readouts. The beam was impingent roughly 50-50 on 2 of the pixel readouts, and therefore we have an additional equation for the 2nd readout of T02. Similar time-walk curves were extracted for T0 when using the different references of T02 and T03, ensuring that we are characterizing the T0 time-walk variation, see Fig 5.11.

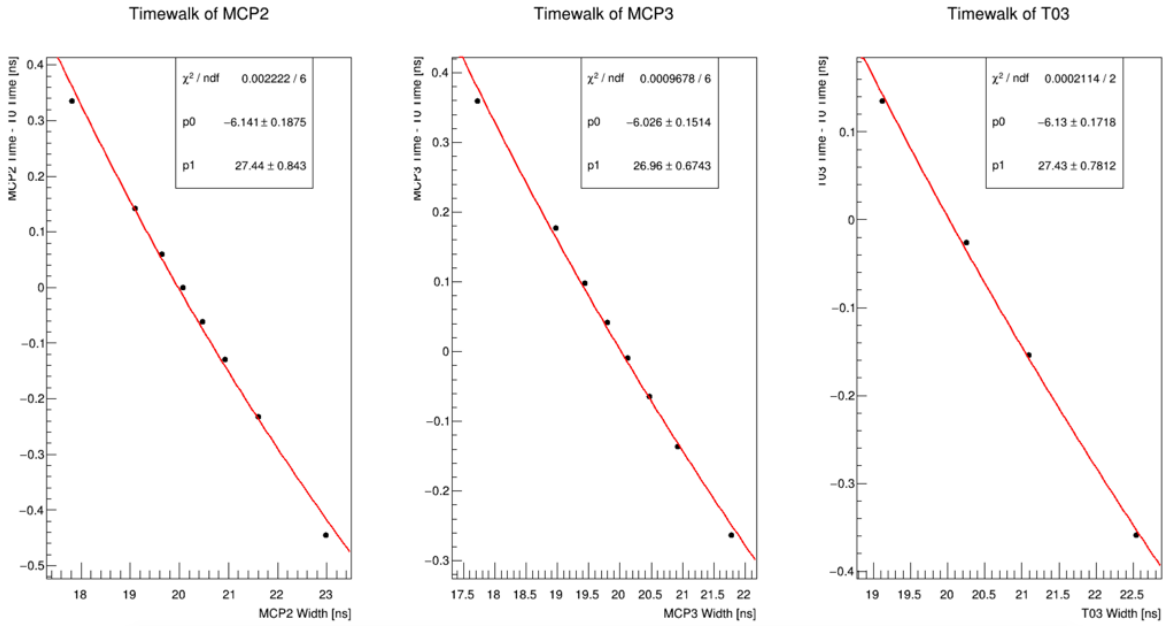

Fig 5.11: Time walk variation of T0 with respect to T02 and T03.

After time-walk variation was corrected, the T0 resolution was extracted from time-difference spectra, Fig. 5.12, and measured to be $\sigma_{T0} \approx 110$ ps.

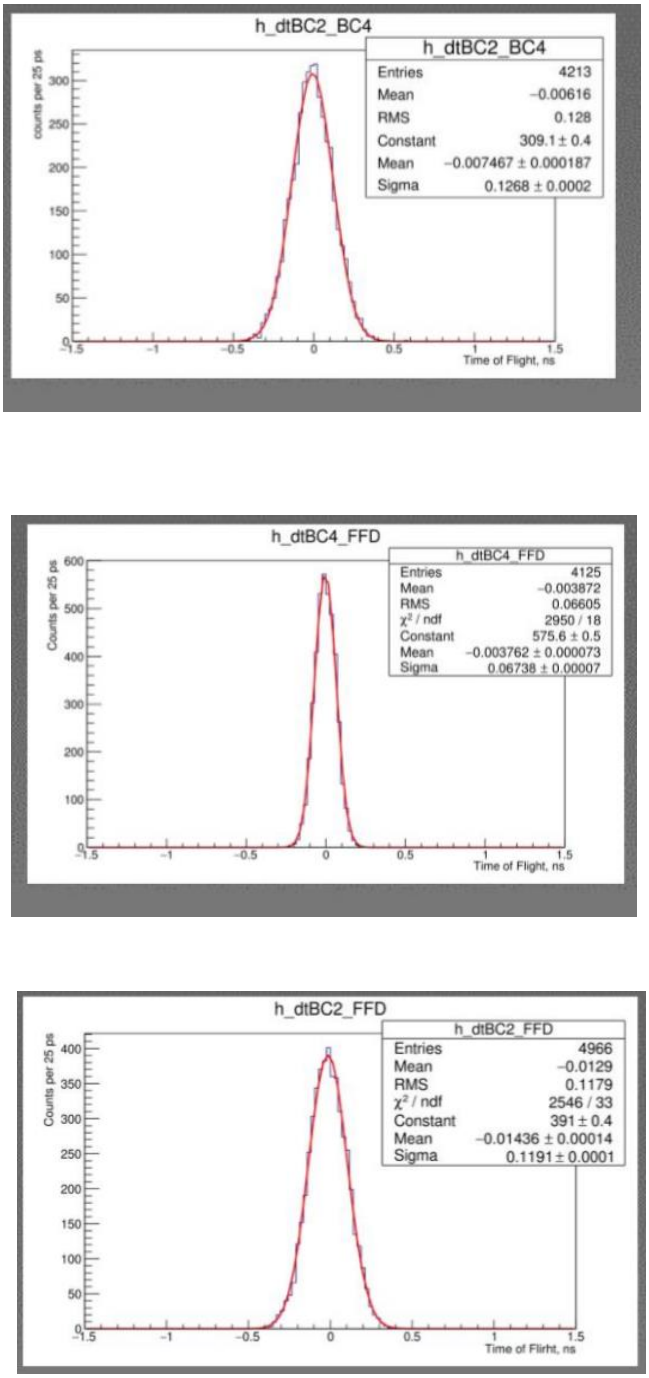

Fig. 5.12: Time difference distribution for BC2-BC4 (top) [mean=-0.007ns, sigma=0.127ns], BC4-FFD (center) [mean=-0.004ns, sigma=0.067ns], BC2-FFD (bottom) [mean=-0.014ns,sigma=0.119ns].

RPC Time-of-Flight

A pre-processing of RPC hits was done in order to account for strip fires due to cross-talk. The pre-processing clustered nearby strips based on an algorithm outlined in Fig. 5.13. Before performing clustering, 70% of events had multiple strips firing in a single plane, and after clustering, 90% of all events have 1 cluster in a single plane of the RPC detector. Almost 95% of all clusters contained fewer than three strips. The clustering conditions in position and time are shown in Fig. 5.14. For the x and y selection we compare to random combinatorics from a MonteCarlo simulation. Strip time were also corrected for time-walk variation relative to T0 time. See Fig. 5.15 for an example where time-walk corrections used. The time-walk correction also aligns all strips to have a ToF peak at 0 ns. The final step needed is a global offset for each strip, which was performed using a photon peak.

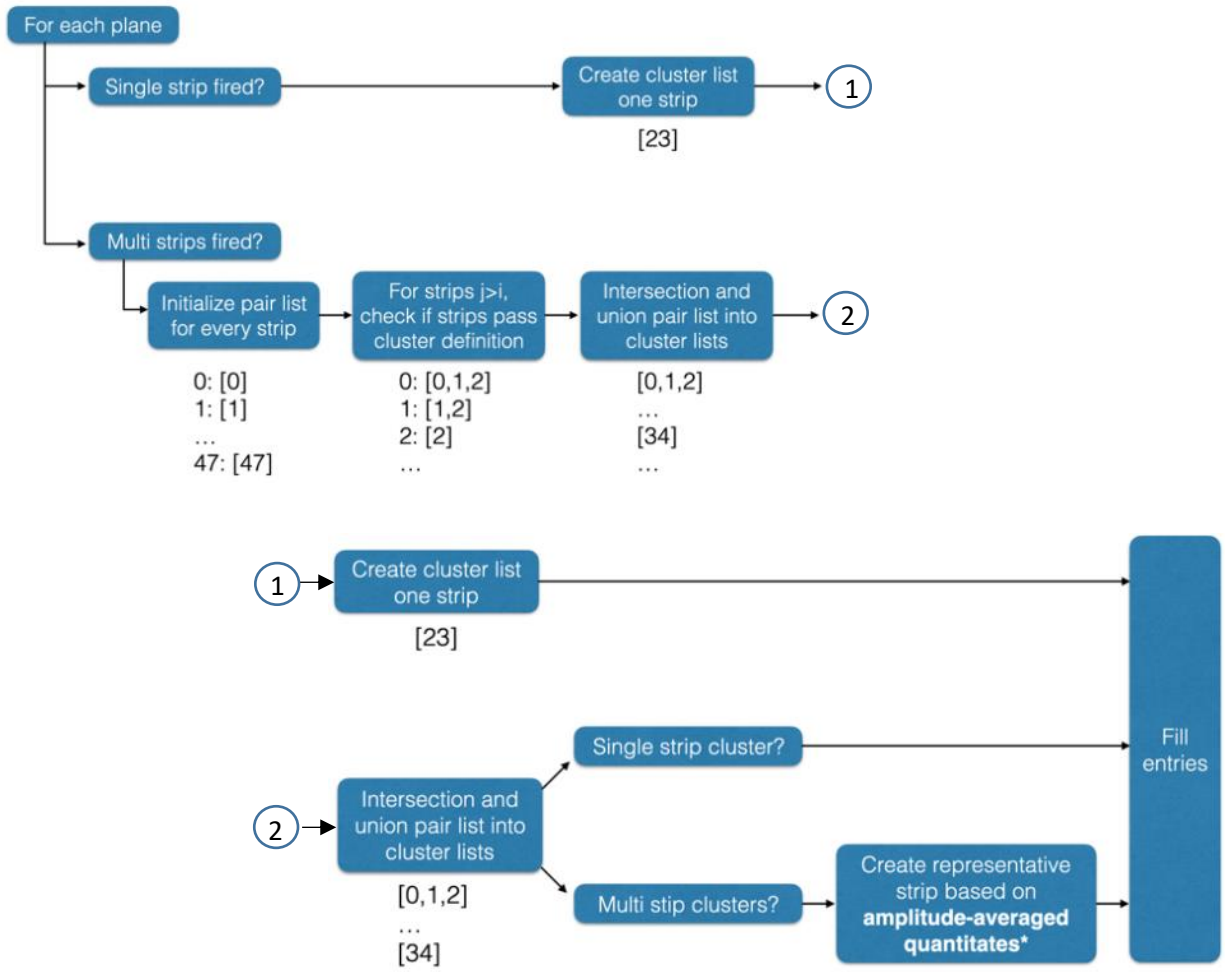

Fig. 5.13: Cluster algorithm for RPC.

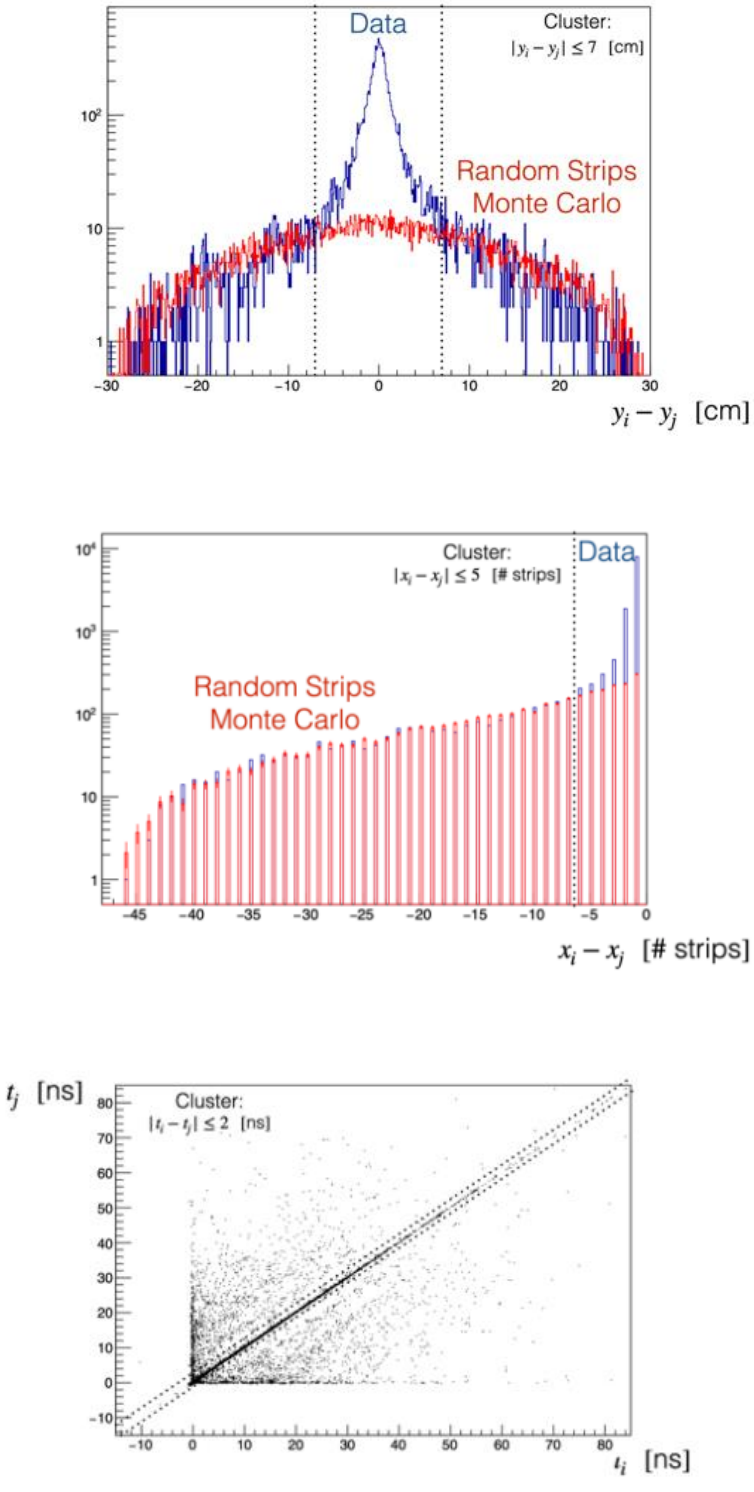

Fig. 5.14: Clustering criterion for two strips (i,j) being considered.

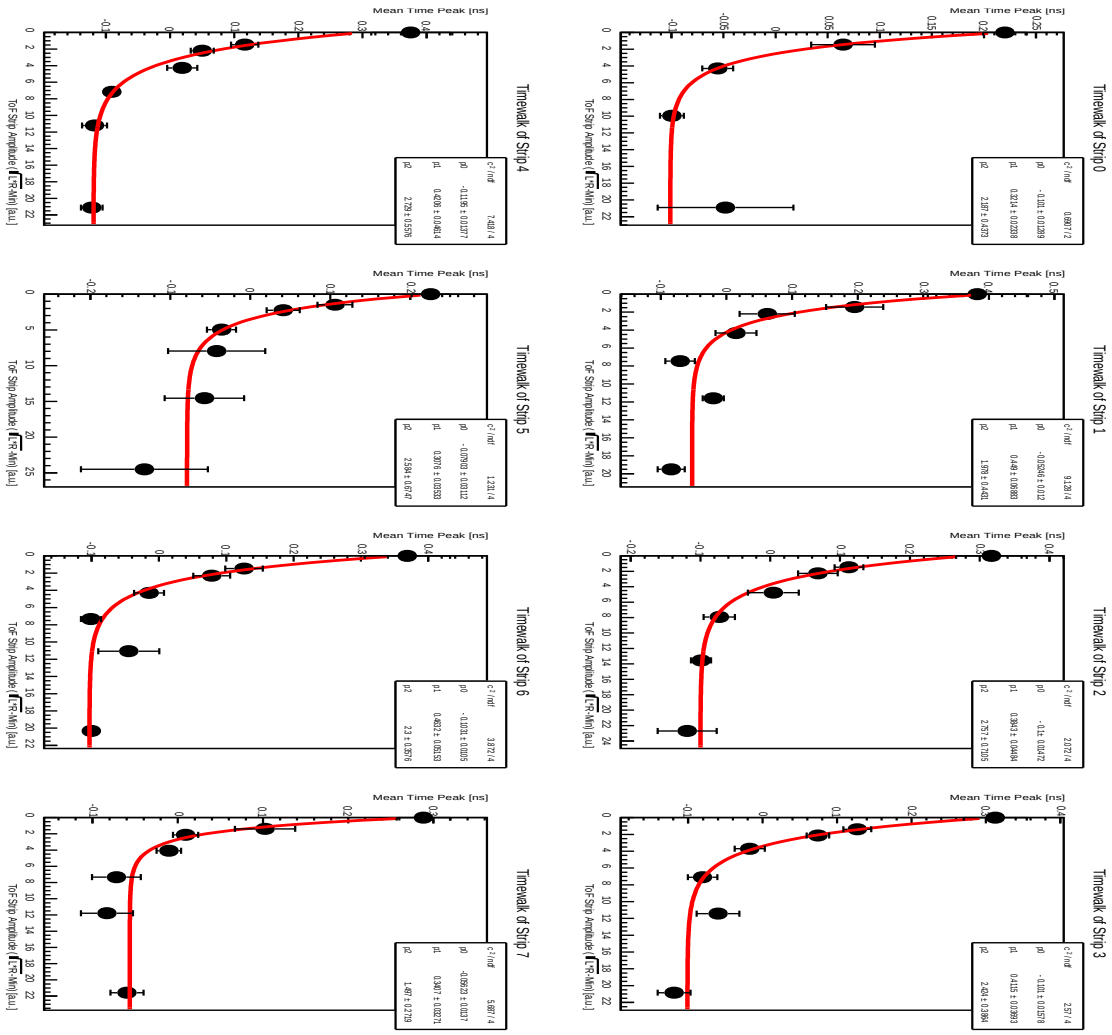

Fig. 5.15: Time walk correction for some representative strips in plane 0 of the RPC detector. The y-axis is mean time of strip relative to T0 time. T0 time has been corrected for time-walk.

The time-of-flight (ToF) global offset for the RPC is done by measuring gamma rays emitted from beam interaction in a single-foil Pb target. A 9 mm thick single Pb target was installed at the center position of the LH_2 target. In addition, a thin lead sheet was placed directly in front of the RPCs to convert gammas to charged particles. Measurements were done with and without the RPC lead sheet and the difference in the measured ToF spectrum for the two measurements was used to isolate the gamma ray events. The subtracted ToF spectrum after calibration is shown in in Fig. 5.16 below, presenting a total ToF resolution (including the t_0 resolution) of 175 ps.

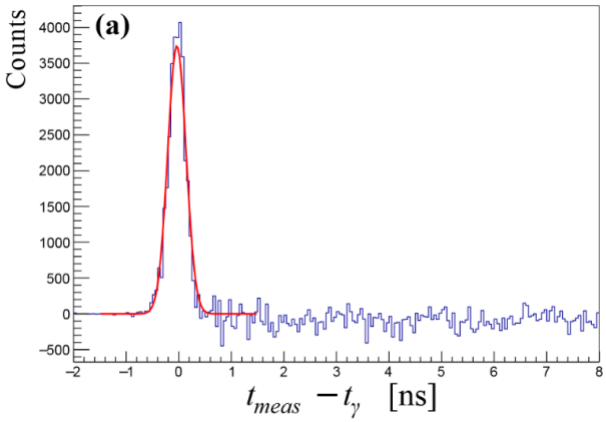

Fig. 5.16: Result of RPC ToF calibration, γ peak arising in subtracted spectrum for Pb target runs with and without Pb sheets directly in front of RPC. The extracted ToF resolution is 175 ps (1σ).

Having determined the reaction vertex, the tracks of the two charged particles in the arms, and the time-of-flight, the total momentum of each of the two particles *i* can be determined, $p_i=\beta_i\gamma_i m$. We assume m is the proton mass.

The momentum resolution is dominated by the ToF resolution. For a 2 GeV/c proton with ΔToF/ToF ∼ 0.95% this translates into a total-momentum resolution of 5.3% in the laboratory system and ∼ 60 MeV/c for the missing momentum in the 12C rest frame extracted from the two protons measured momenta.

6. Fragment Spectrometer

Nuclear fragments following the (p,2p) reaction are emitted at small angles in the direction of the incident beam and therefore pass through the large analyzer magnet SP-41. Trajectories (position and angle) of the forward-focused fragments are measured in front of SP-41 using three silicon (Si) planes and two MWPCs placed in the beam-line downstream of the target (see Chapter 4).

Following the last MWPC the fragments enter SP-41. Two drift chambers (DCH) behind the magnet are utilized to determine trajectories (position and angle) of the outgoing fragments. Inside the magnetic field, fragment trajectories are bent according to their magnetic rigidity *Bρ:*

$$B\rho = \frac{m_u c}{e}\frac{A}{Z}\beta\gamma \sim \frac{P}{Z}$$

where m_u is the atomic mass unit, *c* - speed of light, *e* - electron charge, A - mass number of the fragment, Z - atomic number of the fragment, β=v/c - absolute velocity of the fragment, γ - Lorentz factor, *P* - total momentum of the fragment. It can be seen that the bending magnitude is proportional to the *P*/Z ratio of a given fragment. Hence, by measuring the deflection of the particle trajectory after SP-41 one can obtain information about the total momentum and particle ID.

This is achieved by combining the trajectory information from multiple tracking detectors with Z(dE) information from the two scintillating BCs placed between the target and the entrance of SP-41 (see Chapter 3). As a result, the information on A and Z of a fragment is obtained together with the magnitude of its total momentum P and the corresponding Cartesian components (P_x, P_y, P_z) in the laboratory frame.

We discuss below the fragment analysis –limited in this work to events with a single fragment (B or Be). Discussed are methods for track reconstruction, fragment PID, momentum resolution, and detection efficiency

6.1 MDF Method and BMNRoot Simulations - simple Machine Learning

We follow a Monte-Carlo-based approach to derive the P/Z function from a Multi-Dimensional Fit (MDF) to the simulated fragment trajectories. For this purpose, we used the standard BMNRoot simulator software based on the Geant3 engine. Figure 6.1 shows an example of 100 simulated ^{12}C Monte-Carlo tracks with wide angular and momentum spread centered at the experimental value of 4 GeV/c/u, as well as various experimental devices which were utilized in the experiment, in particular the main tracking detectors which were used for the present analysis: MWPCs, Silicons and Drift Chambers (DCH). The simulated setup geometry is according to the laser measurements performed by Kolesnikov [11]. The corresponding materials of the detectors are also implemented into the simulation.

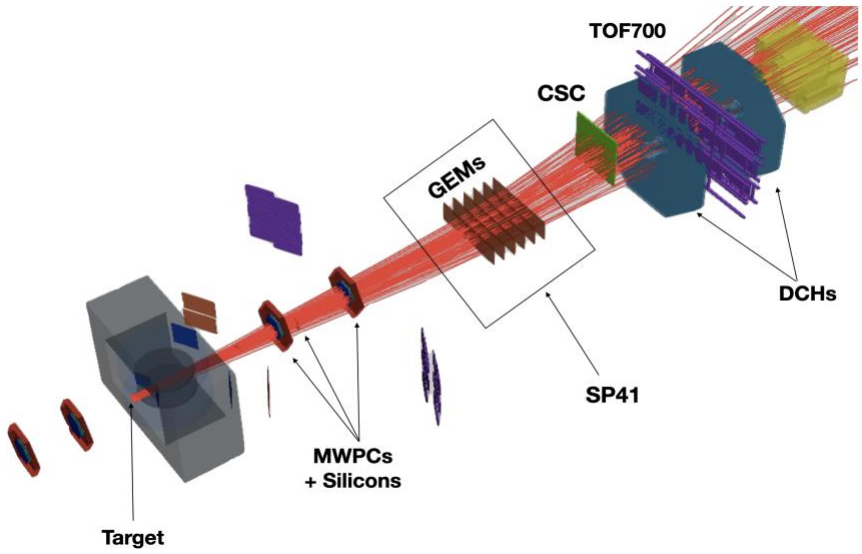

Fig. 6.1: BMNRoot simulations of 100 ^{12}C trajectories through the magnetic field of SP41 (the yoke of the magnet is not shown).

We deployed the standard magnetic field map of SP-41 available in BMNRoot with the field scaling parameter of 1.932. This corresponds to the experimentally set current of 1800 A inside the magnet, same value as used in all main physics runs. The scaling parameter is consistent with the one evaluated from the Hall probe which was continuously monitored during the experiment. Using this "standard" settings, the bending angle of ~6° is obtained for the unreacted ^{12}C beam (P/Z~8 GeV/c).

The simulated Monte-Carlo tracks were chosen to have the maximum random spread in position, angles and momentum in front of SP-41 to cover the entire experimental geometrical acceptance of the magnet and tracking detectors. In total 10^6 Monte-Carlo primary tracks, starting just behind the target position, were simulated and fed as a training sample to the MDF.

A particle trajectory is determined via MWPC-Si upstream tracking system in front of SP-41 (Track Point 0) and via DCHs after the magnet (Track Point 1). Figure 6.2 shows a simplified sketch of the trajectory, lab coordinate system and the definition of the tracking variables which are further used by the MDF algorithm. Both Tracking Points (0 and 1) provide position information (X,Y,Z) and angles (tangents TX, TY). The output of the simulation is used as a training sample for the multidimensional fit (MDF) algorithm [4] in the form of n-tuples which hold positions and angles of the fragment trajectory upstream and downstream of the magnet.

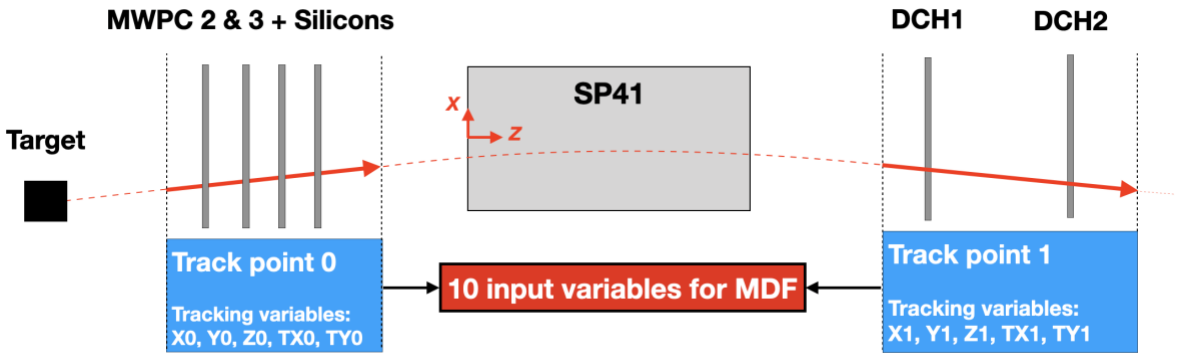

Fig. 6.2: Simplified sketch of the trajectory determination and the corresponding tracking variables used for the Multi-Dimensional Fit.

The Multi-Dimensional-Fit method is based on the following approach. Assume P to be a known quantity of interest (e.g. P/Z, angle, trajectory length, etc.), which depends on N observables (x_1, …, x_N). At first, one creates a training sample of M tuples (events) of the form (xj, Pj, Ej), where $x_j = (x_{1,j}, \ldots, x_{N,j})$ - are N observables in the event j,

P_j - a known value of P in the event j,

E_j - a known error of P_j in the event j.

On the second step, the MDF algorithm tries to find the following parameterization:

$$P_p(\boldsymbol{x}) = \sum_{l=1}^{L} c_l \prod_{i=1}^{N} p_{li}(x_i) = \sum_{l=1}^{L} c_l F_l(\boldsymbol{x})$$

such that:

$$S = \sum_{j=1}^{M} (P_j - P_p(\boldsymbol{x}_j))^2$$

is minimal. In the formulae above: $p_{li}(x_i)$ - Monomials, Legendre or Chebyshev polynomials of x_i, c_l - coefficients determined by the fit. If x_i are linearly dependent, it is possible to apply transformation to an orthogonal basis e.g. using Principle Component Analysis (PCA). Hence, performing MDF over the simulated training sample yields an analytical fit function P/Z_{mdf} =f(X0, Y0, Z0, TX0, TY0, X1, Y1, Z1, TX1, TY1), which can be applied to the positions and angles measured in the experiment.

In a similar way, a second MDF function for TX angle is determined as $TX0_{mdf}$ = f(X0, Y0, Z0, TY0, X1, Y1, Z1, TX1, TY1). This function is used in the following for the tracker alignment and as the track-matching condition $(TX0_{mdf} - TX0_{exp})$ = min, which allows to determine whether the tracks in upstream and downstream detection systems belong to the same global track through the magnet. Figure 6.3 shows the MDF results for these two functions. The obtained tracking precision of ~0.6% for P/Z_{mdf} (without detector resolution) is the result of the multiple scattering in the materials of the beam-line detectors and of a relatively small bending angle in SP-41. For $TX0_{mdf}$ the method provides a precision around 0.7 mrad, see Fig. 6.4.

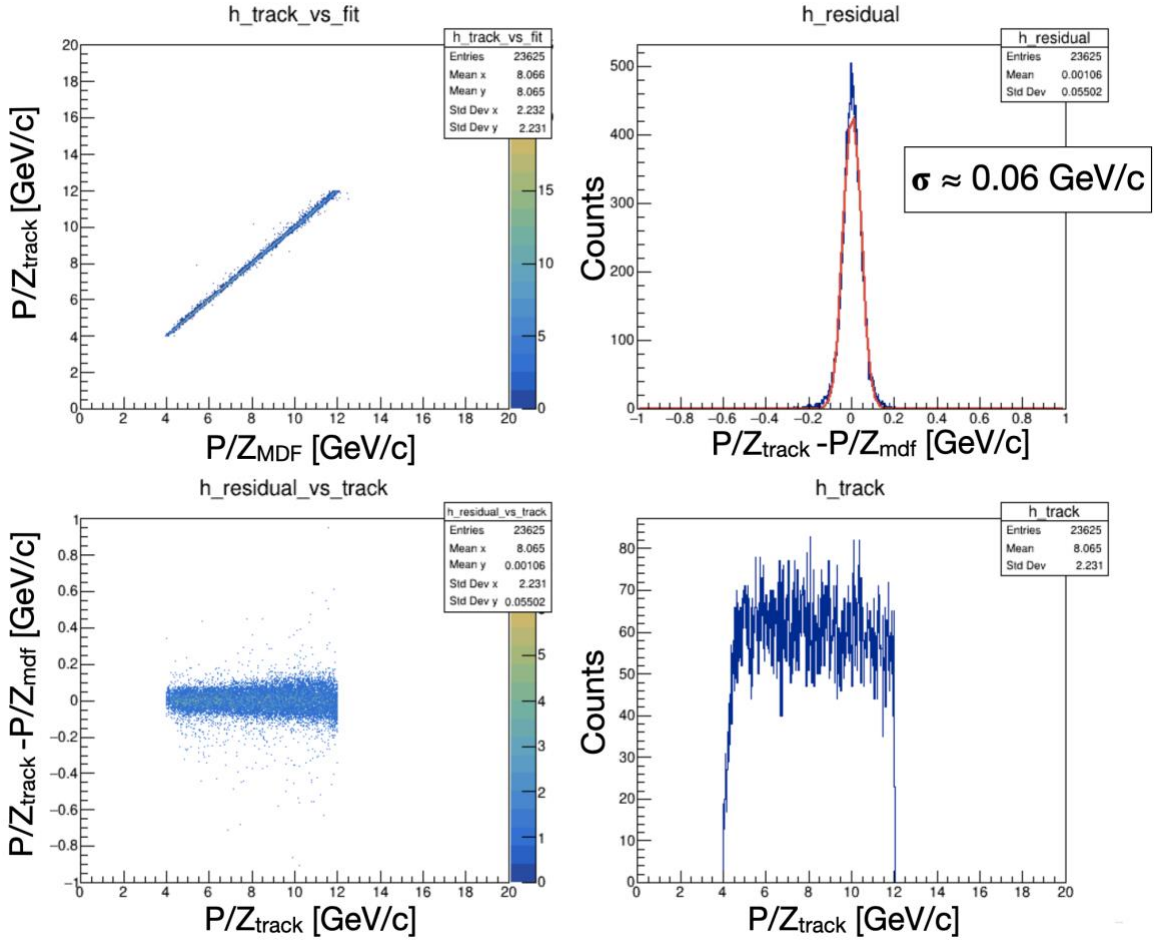

Fig. 6.3: The results of Multi-Dimensional fit to 10_6 simulated Monte-Carlo tracks without detector resolutions. P/Z_{track} is a true value (simulation input) and P/Z_{mdf} is the corresponding value obtained from the MDF fit.

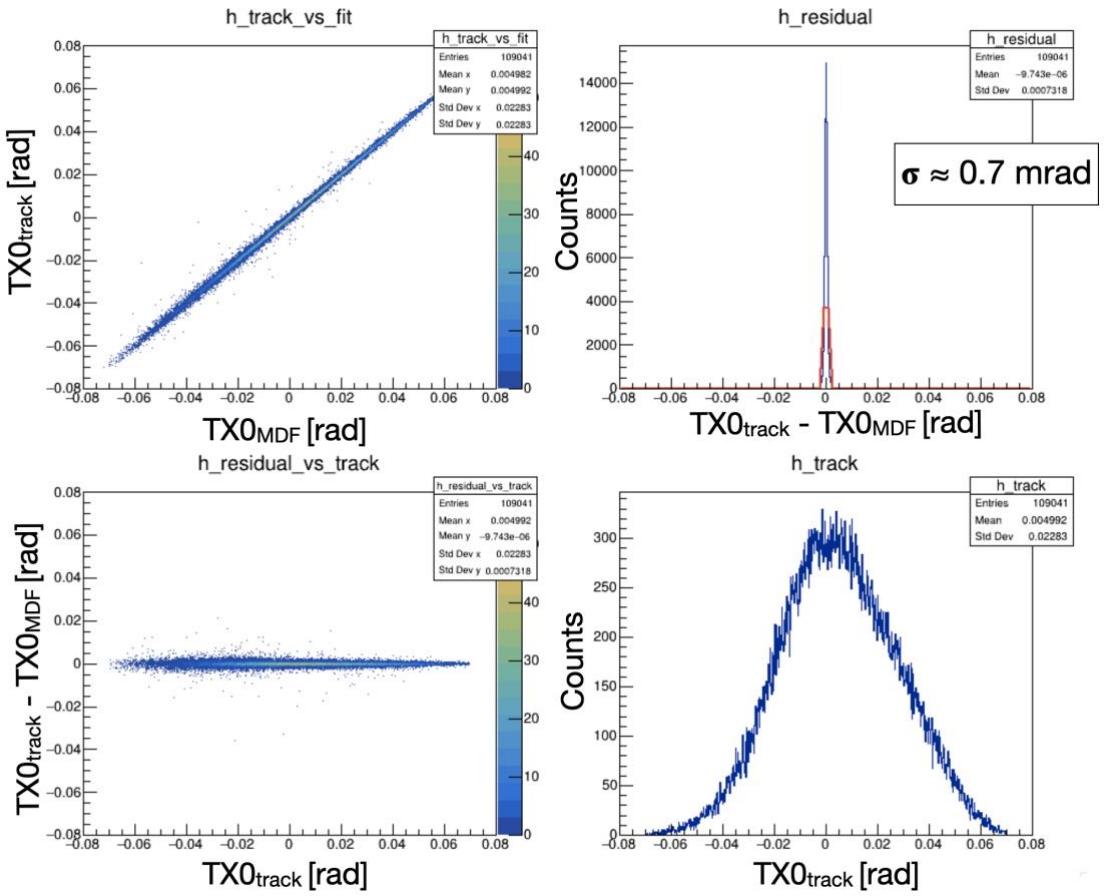

Fig. 6.4: The results of Multi-Dimensional fit to 10_6 simulated Monte-Carlo tracks without detector resolutions. $TX0_{track}$ is a true value and $TX0_{mdf}$ is the corresponding value obtained from the MDF fit.

6.2 Alignment of the Tracker

Having determined the two MDF functions, $TX0_{mdf}$ and P/Z_{mdf}, experimental data requires some fine alignment to match with the MDF input variables. This is related to the fact that precise orientation of the magnetic field with respect to the tracking detectors, as well as the detectors themselves, may slightly differ from what is assumed in the "idealized" simulation, although the physical alignment of the detectors relative to the external yoke of SP-41 may still be correct.

The alignment of the tracker is performed through simultaneous variation of small offsets for each experimental input variable to $TX0_{mdf}$ and P/Z_{mdf}. This requires some reference trajectory, for which purpose the most suitable is unreacted ^{12}C, because its P/Z at the entrance to SP-41 can be precisely evaluated. We have performed additional Geant3 simulations and Bethe-Bloch-based

calculations of the energy loss of ^{12}C in the beam-line materials, which consistently yielded the reference value P/Z_{12C}=7.983 GeV/c for ^{12}C beam at the exit of LH2 target.

At the next step, this reference value is used for the tracker alignment algorithm based on Minuit2-MIGRAD minimization of the multi-parametric function $sqrt[(P/Z_{mdf} - P/Z_{12C})^2]$ which provides an optimum set of constant offsets to be added to the experimental input variables. Figure 6.5 shows the result of such optimization and an offset determined for the experimental TX0 variable.

Below is the summary of the determined offsets:

- TX0 = TX0 + 8.4 mrad
- TX1 = TX1 + 9.2 mrad
- X0 = X0 + 2.8 mm

Offsets for other variables were determined to be either irrelevant or negligibly small. It is interesting to note that the obtained TX0 and TX1 offsets are rather similar, which may point to small rotation (8-9 mrad) of the magnetic field in SP-41 with respect to the externally aligned system of the tracking detectors.

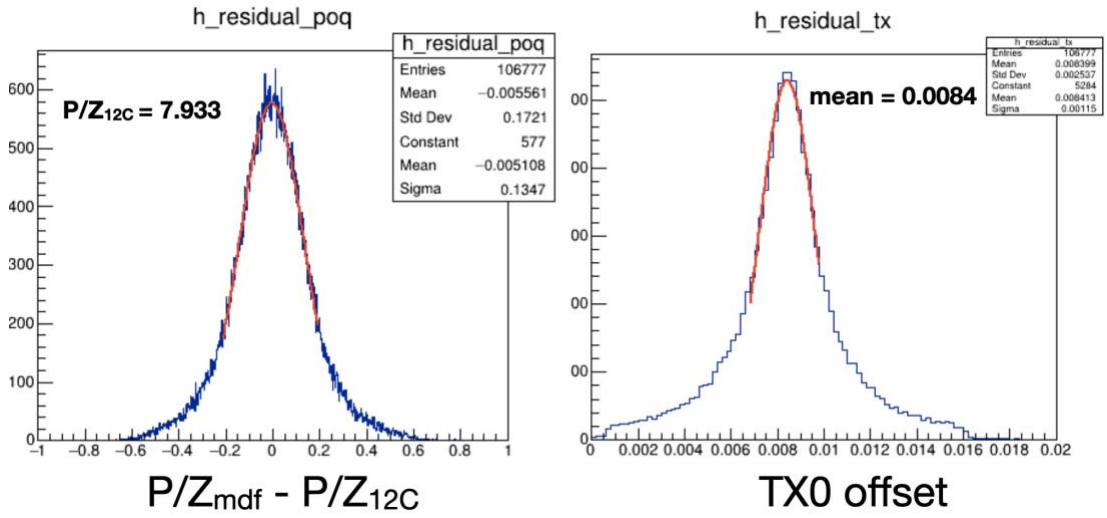

Fig 6.5: Tracker alignment results. Left: MDF residual of experimental P/Z value (unreacted ^{12}C). Right: angular offset for TX0 variable.

Figure 6.6 shows the final momentum distribution of unreacted ^{12}C determined by the MDF method using experimental data from empty target run #2675. Using the MDF approach, a total-momentum resolution of 0.7 GeV/c for 12C is achieved, as estimated with the empty target data, consistent with the resolution limits of the detection systems. The same momentum resolution was obtained for unreacted 12C events, analyzed under the same conditions but with LH2 target

inserted. A width of σ = 0.7 GeV/c was measured with a reduced beam momentum of 47.6 GeV/c due to energy loss in the target and additionally straggling. The achieved momentum accuracy is evaluated to be 0.2%.

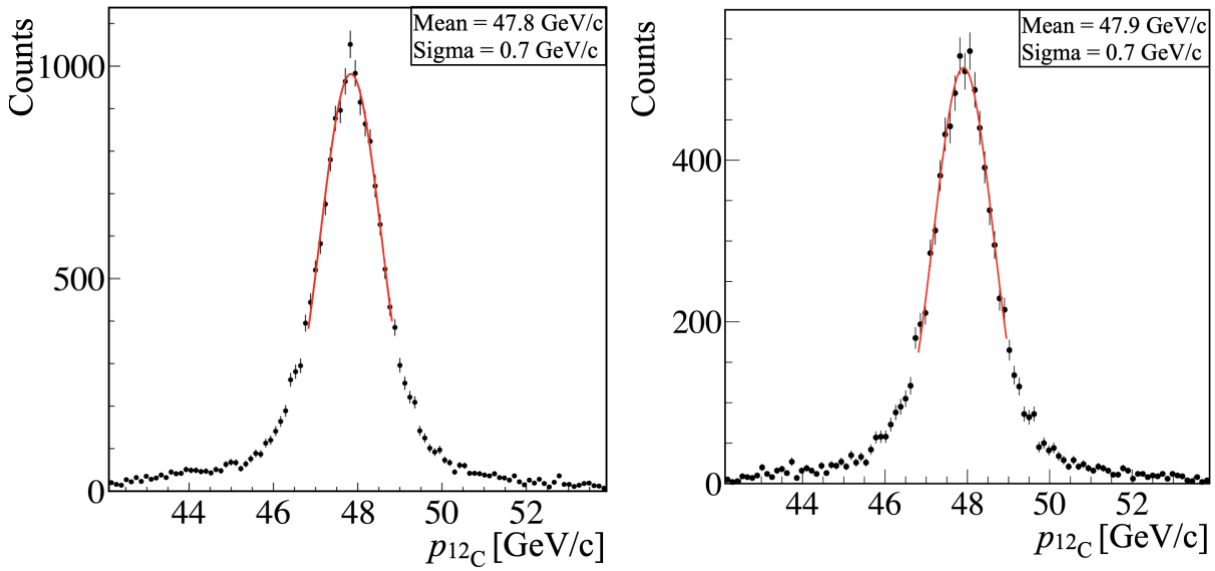

Fig. 6.6: Experimental momentum of unreacted ^{12}C determined by MDF method using data from empty target run #2675 (left) and from a run with filled LH2 target (right).

6.3 Global Tracking: Applying MDF tracking to the experimental data

After the alignment of the tracker has been performed, the two functions P/Z_{mdf} and $TX0_{mdf}$ can be applied to define global tracks through the setup. Track information before SP-41 is reconstructed either from Silicons or MWPC_p1 or from both (Upstream). This work is described in Chapter 4 of this report. Downstream tracking in DCH1 and DCH2 was performed by N. Voitishin and his colleagues as well as tedious calibrations and alignments of those detectors. Here we discuss only the global track information provided by stitching tracks between DCH1 and DCH2. Thus, the remaining issue is combinatorics of the downstream tracks in DCH and upstream tracks in the detectors before SP-41. To solve this problem, we used the following track matching criteria:

$$|TX^0_{mdf} - TX^0_{exp}| < 5\sigma_{tx}$$

Figure 6.7 shows the performance of the second MDF function for $TX0_{mdf}$. A global track is constructed when the reconstructed $TX0_{exp}$ falls within the 5σ gate indicated in the figure. Figure 6.8 illustrates the basic global track-matching algorithm in the form of the decision-making tree. Multiplicities of the reconstructed global tracks and their correlation with DCH tracks are shown in Fig. 6.9.

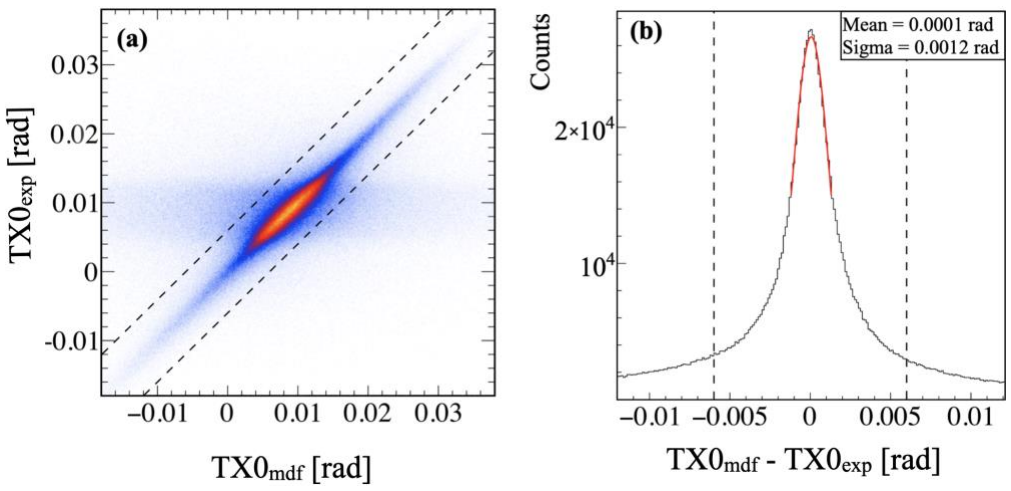

Fig. 6.7: Track Matching. (a) Correlation between TX0 angle measured upstream of the magnet and the TX_{mdf} reconstructed by the MDF. Dashed lines indicate applied cuts for the track matching condition. (b) Residual distribution and the applied cuts as in (a).

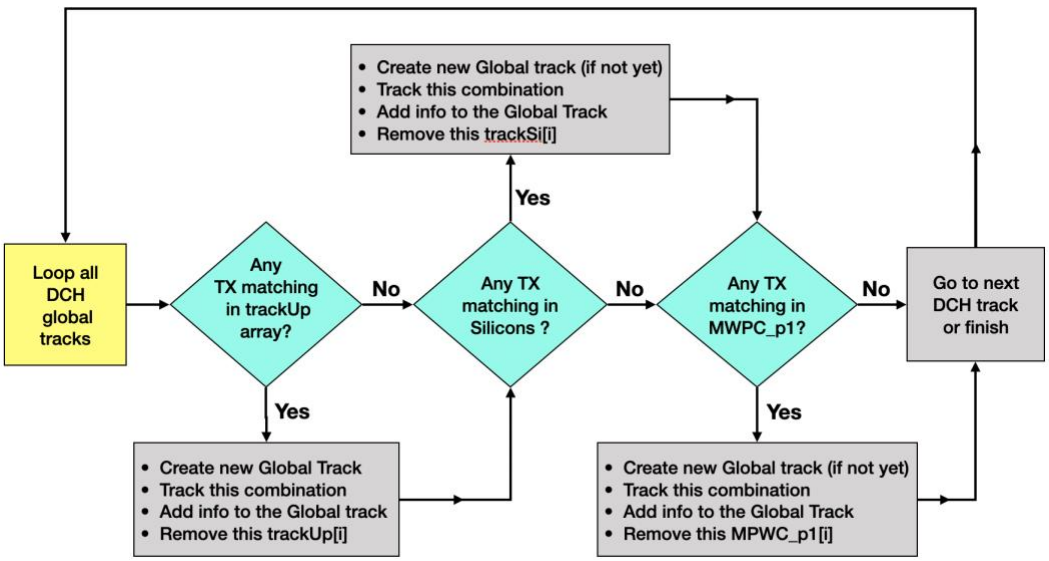

Fig. 6.8: Global track-matching algorithm.

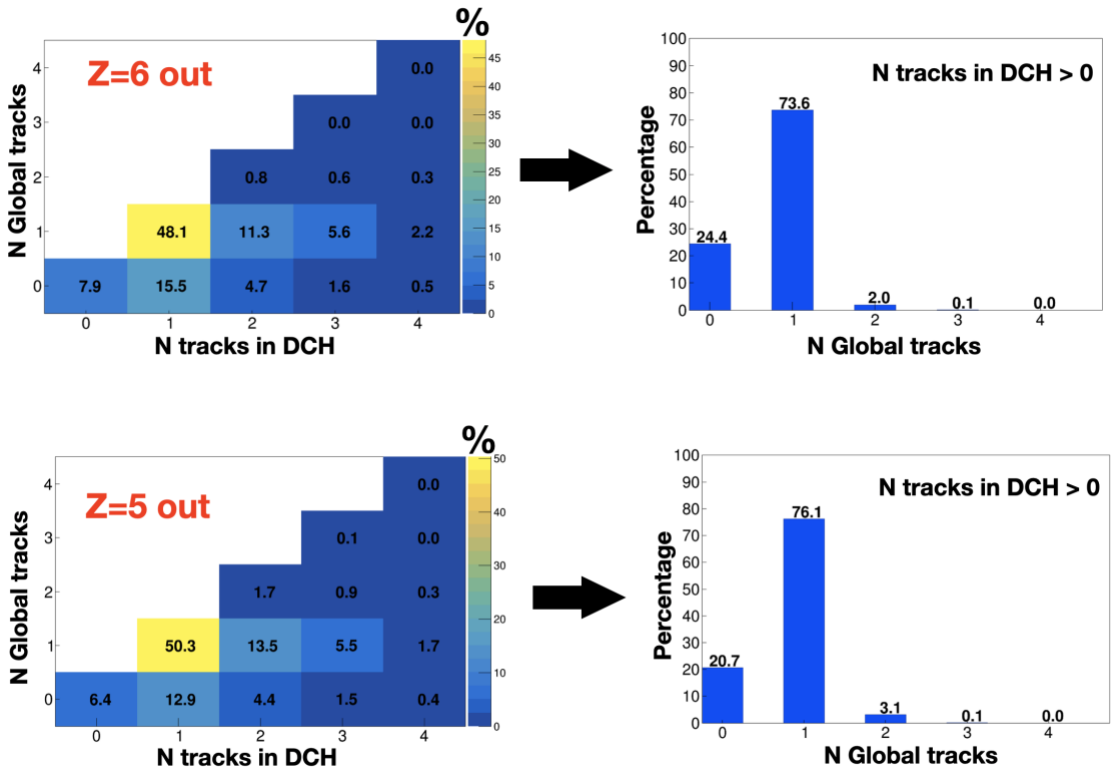

Fig. 6.9: Multiplicities of the reconstructed global tracks (color = normalized counts) and their correlation with DCH track.

6.4. Fragment PID and Momentum

Output of the track matching algorithm provides global track information which includes Px, Py, Pz, Ptot, A and Z of the fragments escaping the target. Figure 6.10 illustrates two examples of particle ID for single and double track events. In the present analysis we focus on the events with a single heavy global track (e.g. 11B,10B,10Be) so we do not detail here the multi-track events.

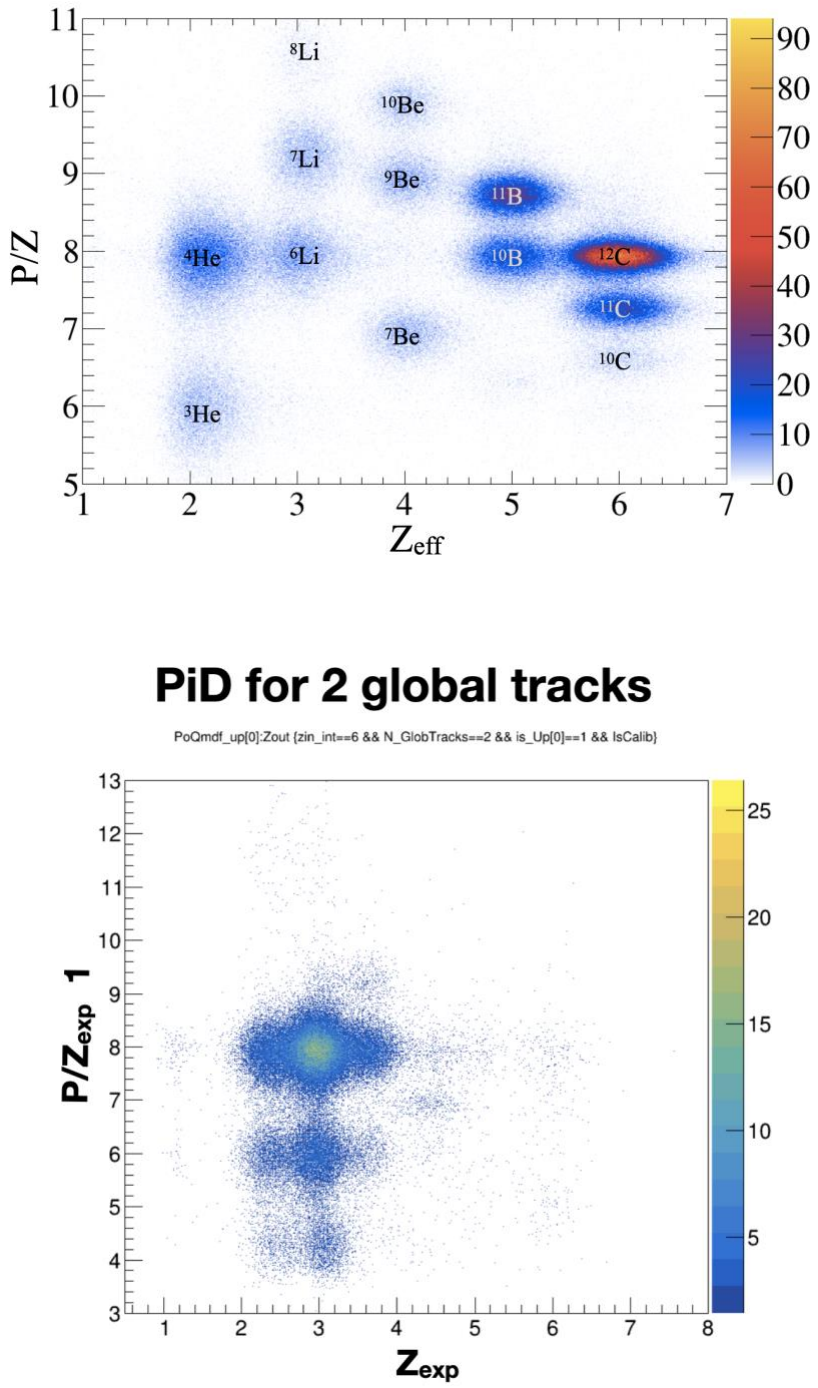

Fig. 6.10: Particle ID example for the events with one reconstructed global track (top) and when two global tracks are reconstructed (bottom). In the right picture P/Z of only one track is plotted. Z information is obtained from energy-loss measurement in BC counters after the target (as Z_{eff}).

The P/Z information together with the total charge measured in BC3 and BC4 ($\sqrt{\Delta E_{BC3}\Delta E_{BC4}}$) is the way we select the heavy fragment in a 2D elliptical cut, requesting also a single track. However, we apply beforehand already a 2D charge selection for the signal between BC3 and BC4, see Chapter 3. The elliptical cut for selecting 11B, cf. Fig. 7.6, selects in P/Z and $\sqrt{\Delta E_{BC3}\Delta E_{BC4}}$, the size is defined as:

$\sqrt{\Delta E_{BC3}\Delta E_{BC4}}$ = 624.4901 with radius 140.04 (arb. units)

P/Z = 8.6910 with radius 0.3656.

As the total fragment momentum is obtained at the position right after the target from the MDF, we correct explicitly for the energy loss in liquid hydrogen up to the reaction vertex in beam z direction. Since on a short path in the target (max. 30 cm) and at high beam energy that loss is well described by a linear function for the momentum decrease, but different for different nuclear charge. For carbon we apply 10.82 MeV/c/cm.

The fragment momentum is obtained directly from the MDF, its Cartesian components are given with respect to the incoming beam vector (event-wise). Eventually, the fragment momentum is studied in the rest frame of the incoming 12C beam, boosted along the beam vector. The distributions are shown in Fig. 6.11 for 12C(p,2p)11B. We acknowledge that the fragment selection in P/Z introduces a momentum acceptance in the longitudinal component.

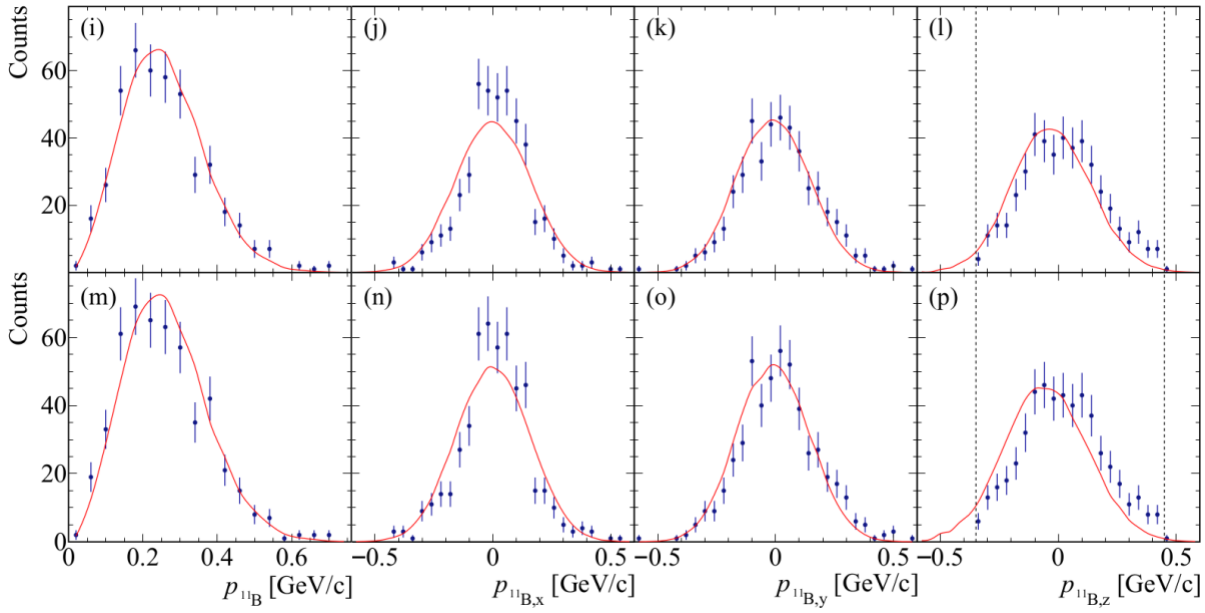

Fig. 6.11: $_{11}$B fragment momentum components are shown in (i)-(l), and (m)-(p). The dashed lines in $p_{11B,z}$ indicate the momentum acceptance due to the fragment selection in P/Z. Upper panel: With QE selection as described in Chapter 7, lower panel only with missing mass cut for QE selection, see Chapter 7 for details.

6.5 Tracking Efficiency

The fragment tracking efficiency is (50 ± 5)%, obtained for an empty target run and given with respect to the incoming and outgoing Z = 6 ion. This tracking efficiency includes the involved detector efficiencies, as well as the reconstruction and matching efficiency of good tracks. We define the tracking efficiency for 12C as ratio of events, incoming carbon $12C_{in}$ vs. carbon downstream the target $12C_{out}$, with

$$\epsilon_{\text{track}} = \frac{\#^{12}\text{C}_{\text{out}}}{\#^{12}\text{C}_{\text{in}}} = \frac{\#(\text{Good track})\&(Z_{\text{in}} = 6)\&(Z_{\text{eff}} = 6)}{\#(Z_{\text{in}} = 6)\&(Z_{\text{eff}} = 6)},$$

where a "good track" is defined by

- Tracks in one of the upstream detector systems and in DCH.
- Exactly one reconstructed matched global track based on the combined information from upstream detectors and DCH as explained above.
- A "good" P/Z value: for 12Cout the P/Z value is expected to be centered around 7.98 GeV/c (for beam momentum of 47.9 GeV/c), cf. Fig. 6.6. To determine the efficiency we examined different cuts in the range1275 $(2 - 5)\sigma$ based on a Gaussian distribution in order to get an averaged value for the tracking efficiency. To identify the outgoing fragment in a similar way to the physics analysis we considered the 2D cut on P/Z vs. the energy deposit in BC4 and BC3, and checked for the systematics. The uncertainty is defined as the standard deviation resulting from those different cuts with respect to the mean value.

The table below lists the different contributions to the extracted efficiency.

Table 6.1: The different contributions to the tracking efficiency.

Good track	$\epsilon_{\text{track}}(\%)$
$Z_{\text{in}} = 6$, $Z_{\text{eff}} = 6$	100
Upstream track	98
DCH track	93
Upstream and DCH tracks	91
Global track	70
Good P/Z	50

We adapt the same value for outgoing charge Z_{eff} = 4,5, in particular for 10Be the only Be isotope of interest. The reaction probability from in-beam material downstream the target was estimated to be smaller 5% and thus only contributes a small fraction to the latter condition.

We estimated the uncertainty for B isotopes, and 10Be extraction efficiency using the experimental data. We looked at the fraction of 11,10B (10Be) from events with Z_{eff} = 5 (Z_{eff} = 4). Z_{eff} = 5 comes

dominantly with 11B or 10B. We varied the fragment identification cuts to check the sensitivity of this fraction. This resulted in a very similar uncertainty to the 12C, and therefore we adapt the same uncertainty. $Z_{eff} = 4$ can come with several Be isotopes, or a combination of lighter fragments. In this case, to evaluate the uncertainty, we looked at the fraction of 10Be from events with $Z_{eff} = 4$, and changed the identification cuts to evaluate the sensitivity. This resulted in ~ 30% difference (as opposed to 10% for C and B). Therefore, for 10Be, we consider $\varepsilon_{track} = (50\pm15)\%$. For the overall fragment identification efficiency an additional $(83 \pm 6)\%$ efficiency for the measurement of the outgoing charge in BC3 and BC4 needs to be added.

7. Single-Proton Knockout

In order to select the reaction channels of interest we identify event-wise incoming 12C as discussed before, and two protons in the TAS, which together defines the *inclusive channel* (12C(p,2p)). Making use of the fragment identification, discussed above, the *exclusive channel* is identified (12C(p,2p)11B).

7.1 Event Selection

The basic selection criteria for any analysis require an incoming 12C, as well as a "good" reaction vertex with scattering in the LH2 volume. This means, two tracks in the TAS with the minimum distance smaller 4 cm have to be reconstructed. The spatial selection of the beam spot in xy is indicated in Fig. 7.1, which removes scattering on the target vessel that was not rejected by the V-BC. In the z direction a selection from the target center with +-13 cm is applied (see Fig 5.10). Both conditions ensure scattering on target protons only.

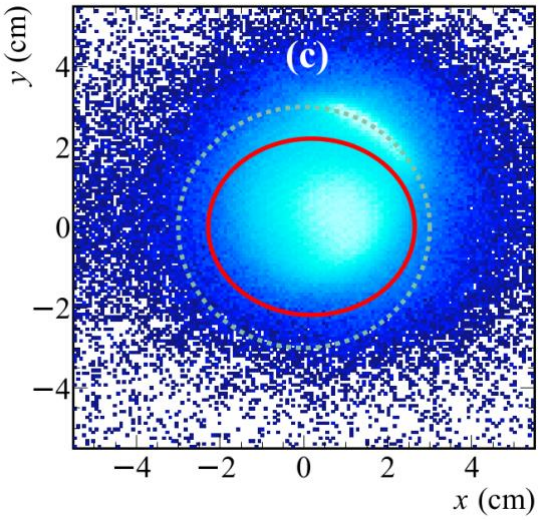

Fig. 7.1: The xy position at the reaction vertex is shown, measured with the MWPCs in front of the target. The dashed line indicates the target cross section. Scattering at the target vessel at

around (x = 2 cm,y = 2 cm) can be seen which is removed by the selection as indicated by the red circle.

As described before, the momenta of the presuming two protons are calculated with respect to the incoming beam direction and using the time-of-flight information between the target and the RPC. In order to select (p,2p) events from Quasi-Free Scattering (QFS), other particles that also create a track but originate from e.g. inelastic reactions like pions need to be rejected. The basic selection is applied to the velocity of the two measured particles. In the analysis, every particle must pass the velocity condition $0.8 < \beta < 0.96$, see Fig. 7.2, which removes fast and slow pions in coincidence with another particle, further details on the effectiveness are studied in a simulation (see App. A). The additional selection criteria based on the reconstructed missing momentum are discussed in the following.

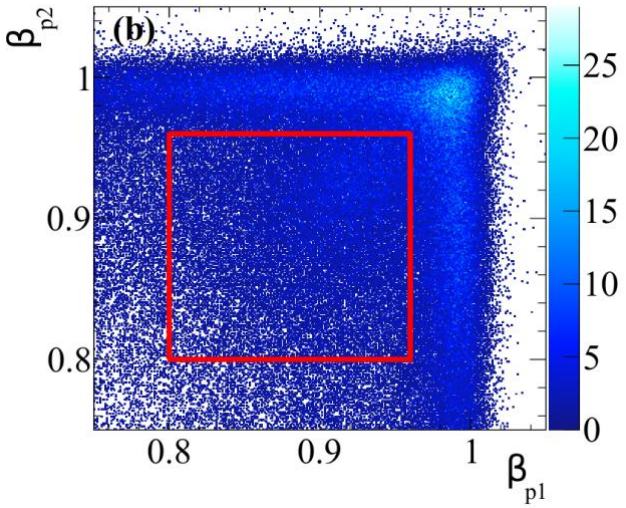

Fig. 7.2: Basic velocity condition to select protons, the velocity cut in the left and right arm are indicated by the red lines.

7.2 Missing Momentum Extraction

The momentum of the knocked-out proton p_{miss} is obtained from the four-momenta of the scattered protons (p1,p2) in the TAS,

$$\bar{p}_i \approx \bar{p}_{\mathrm{miss}} \equiv \bar{p}_1 + \bar{p}_2 - \bar{p}_{tg},$$

assuming the target-proton is standing in lab. system, and working in the spectator assumption

$$\bar{p}_{^{12}\mathrm{C}} = \bar{p}_i + \bar{p}_{^{11}\mathrm{B}}.$$

A boost from the laboratory system into the rest frame is applied along the incoming beam direction considering the reduced beam energy at the reaction vertex.

In order to identify real (p,2p) QE events and reject IE events, we applied a 2D selection in missing energy and the in-plane opening angle of the two particles measured in the arms, i.e. an elliptical cut denoted by 2σ is applied in each direction, defined in the exclusive channel. The distribution is shown in Fig. 7.3, and their projection in Fig. 7.4. The standard deviation was obtained from a Gaussian fit to E_{miss} and $\theta_{p1} + \theta_{p2}$. The missing energy is defined as $E_{miss} = m_p - e_{miss}$, where e_{miss} is the energy component of P_{miss} in the rest frame of the 12C nucleus.

The QE elliptical cut is:

$\theta_{p1} + \theta_p = 63.1°$, radius 3.6° (2σ),

$E_{miss} = 0.016$ GeV, radius 0.216 GeV (2σ)

The IE part is defined from the remaining events within the other ellipse. The same criteria are applied in the inclusive channel. Other relevant distributions are shown in Fig. 7.5. We chose to apply the selection not in pmiss to not introduce an obvious bias in the momentum distributions. A selection in missing mass is applied in a second step as detailed in the next section.

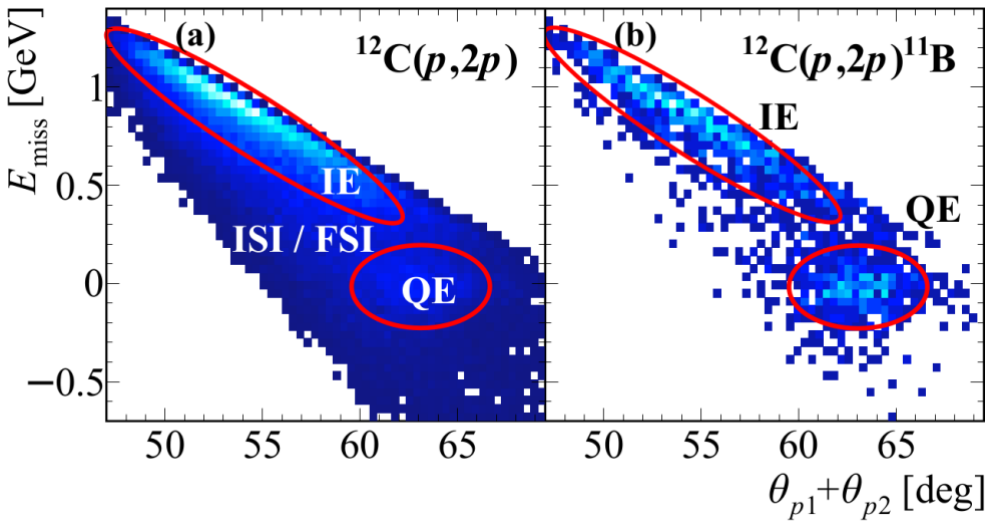

Fig. 7.3: The correlation between the measured missing-energy E miss, calculated in the 12 C rest-frame, and the measured lab-frame two-proton in-plane opening angle. Distributions are shown for (a) 12 C(p, 2p) and (b) 12 C(p, 2p) 11 B events. Quasielastic (QE) events are seen as a peak around low missing energy and opening angles of ∼ 63° that is marked by a red oval.

Inelastic (IE) reactions populate higher missing-energy and lower opening angles while ISI/FSI populate both regions and the ridge between them in the inclusive spectra.

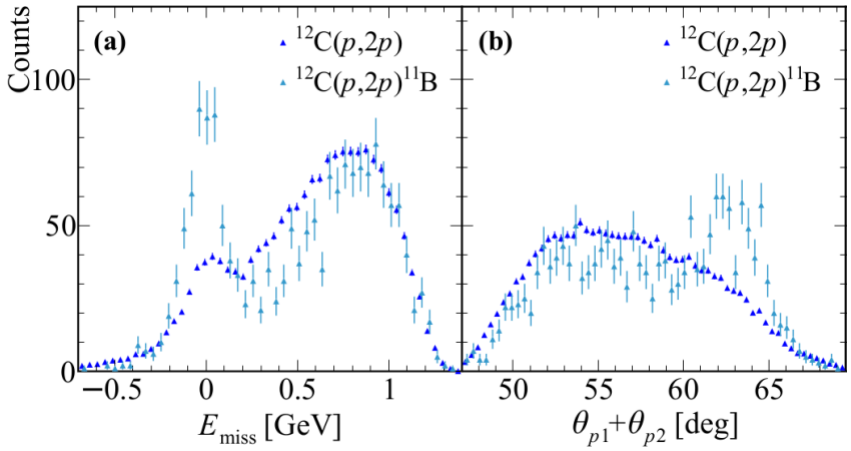

Fig. 7.4: Projection in missing energy (a) and in-plane opening angle (b) of Fig. 7.3, comparing the inclusive reaction 12C(p, 2p) and tagged events with 11B coincidence (the latter points are slightly offset for better visibility). The inclusive distribution is area normalized to the tagged one. The fragment selection clearly suppresses FSI, and the QE signal separates from IE.

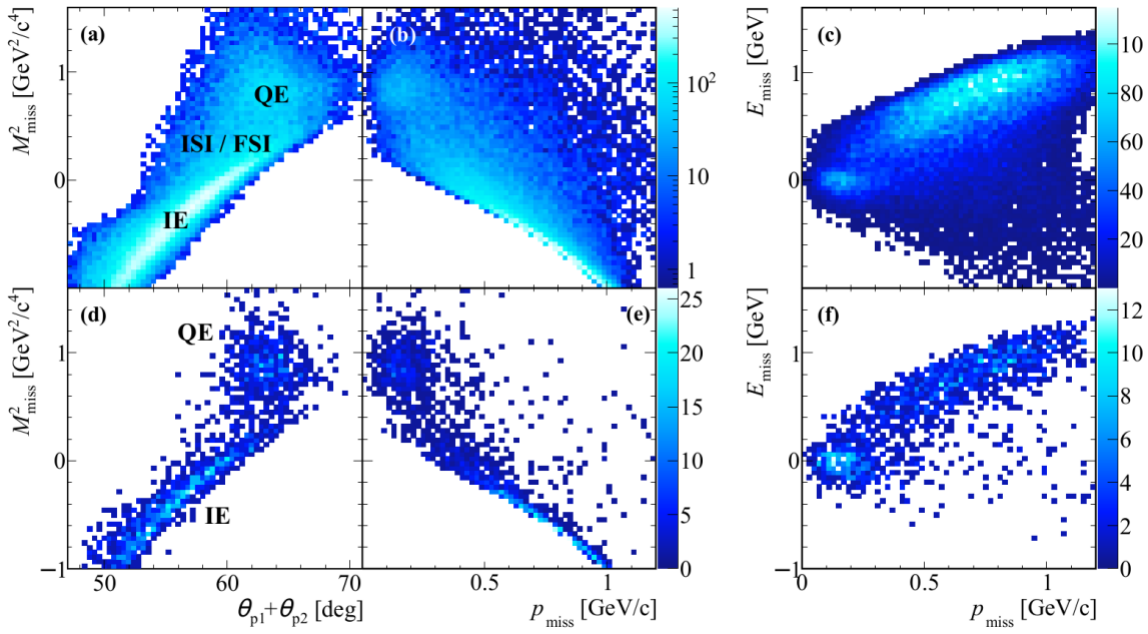

Fig. 7.5: Kinematical Correlations in single-proton Knockout. Figures (a)-(c) show the inclusive 12C(p,2p) channel, and (d)-(f) the exclusive channel, i.e. with tagging 11B. In both cases, the quasielastic peak (QE) and inelastic (IE) events are visible, while ISI/FSI are reduced by the fragment tagging. Eventually, a selection in Emiss and in-plane opening angle was chosen to select QE events, see Fig. 7.3. The distributions are not corrected for fragment-identification efficiency.

7.3 Exclusive Reaction Channel

We applied the QE cuts on the (p,2p) events. We are left with Boron fragments but no unreacted beam, see Fig. 7.6. The exclusive reaction channel requires an additional identification of the heavy fragment, namely 11B for the meanfield analysis, following the fragment selection as discussed above in Chapter 6.

In Fig. 7.7 clearly the nucleon mass is reconstructed. Additionally, a lower boundary in the squared missing mass of $M^2_{miss} > 0.47$ GeV^2/c^4 is applied for sanity to remove very few background events after the QE selection, see Fig. 7.7.

The (p,2p) scattering itself features a distinct angular correlation between the two scattered protons. The ~90° c.m. scattering angle reflects in our kinematics as in-plane opening angle in the lab of $(\theta_{p1}+\theta_{p2})$~63° and off-plane $\Delta\varphi=\varphi_{p2}-\varphi_{p1}$ with ~180° (360°-Δφ if Δφ>180°). The distributions are shown Fig. 7.8 with cut in missing mass only for the QE selection, not to introduce any bias in the angular distribution.

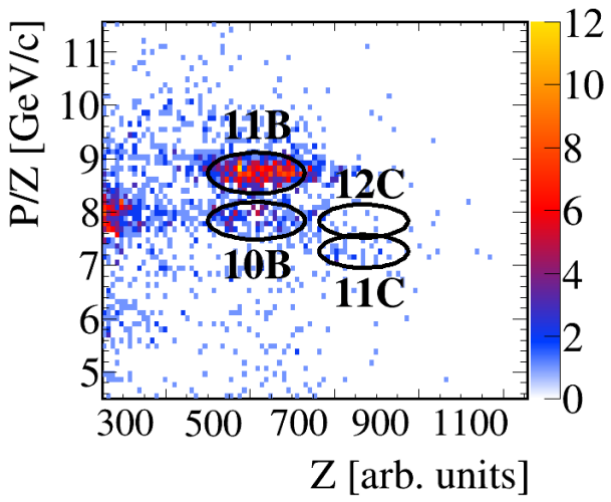

Fig. 7.6: Fragment identification, with (p,2p) additional quasielastic selection cuts.

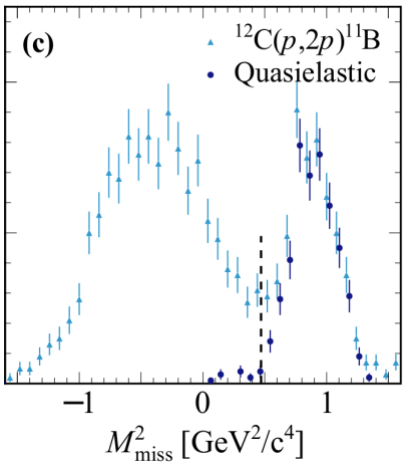

Fig. 7.7: Proton missing mass for tagged 12C(p, 2p)11B evens. After the QE selection in Emiss and in-plane opening angle, the distribution is shown in dark blue dots with artificial offset for better visibility. We apply an additional missing mass cut $M^2_{miss} > 0.47$ GeV^2/c^4, indicated by the dashed line.

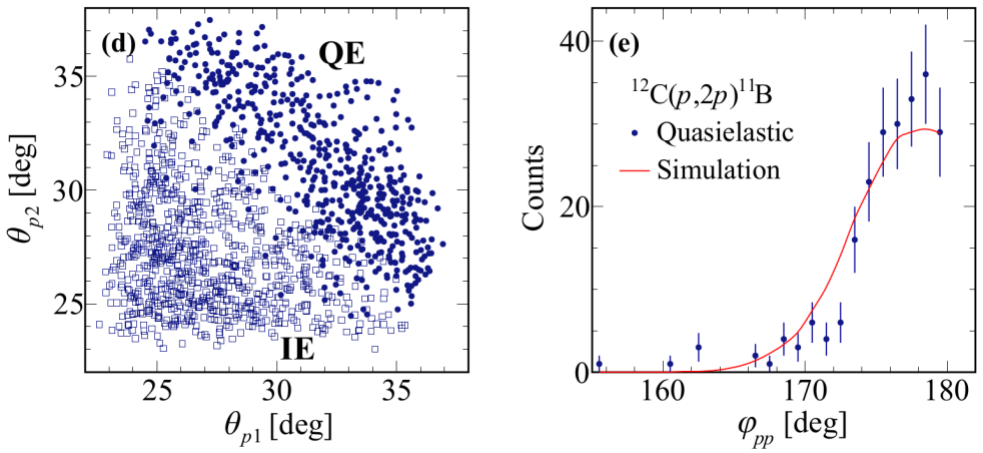

Fig. 7.8: Angular correlation between the two (p, 2p) protons for quasielastic ($M^2_{miss} > 0.47$ GeV²/c⁴) and inelastic ($M^2_{miss} < 0.55$ GeV²/c⁴) reactions only selected by missing mass. The QE events show a strong correlation with a polar opening angle of ~ 63°. Right: The off-plane opening angle for $M^2_{miss} > 0.55$ GeV²/c⁴ peaks at 180° as expected.

The resulting missing-momentum distributions for the QE selection decomposed in their components are shown in Fig. 7.9, together with the unbiased selection in missing mass only (lower panel). No difference between those two QE selections is observed.

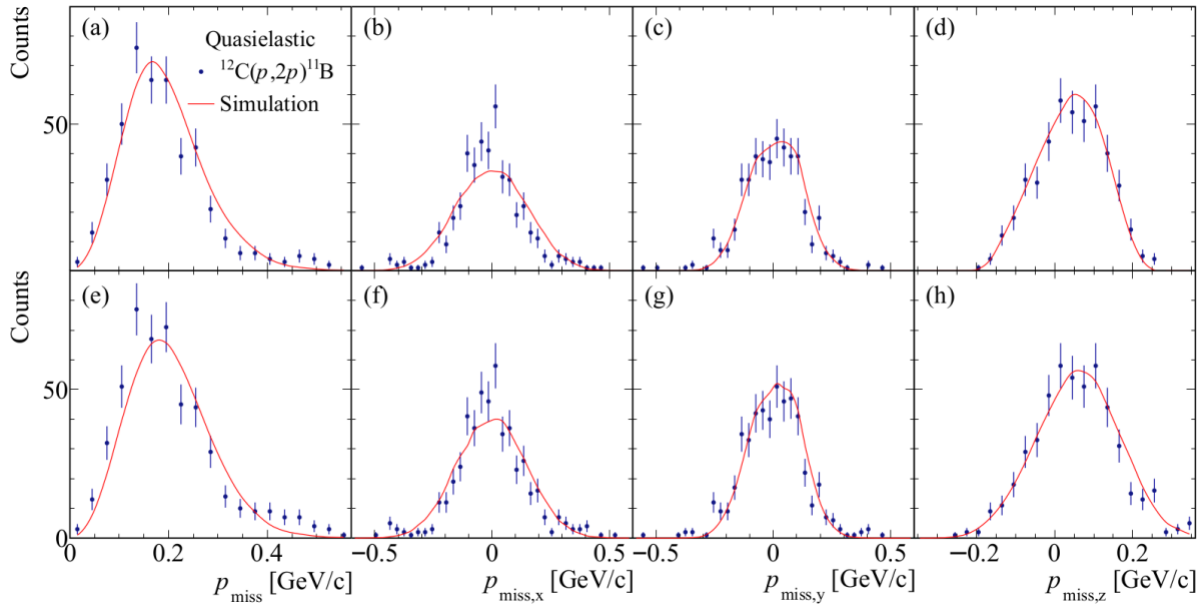

Fig. 7.9: Momentum components for quasielastic 12C(p,2p)11B reactions compared to simulation. The proton missing momentum is shown for (a)-(d), while (e)-(h) show the same distributions but with missing mass cut only $M^2_{miss} > 0.55$ GeV²/c⁴.

7.4 Simulation

Our data are compared to theoretical calculations of exclusive QE (p,2p) scattering off a p-shell nucleon in 12C. The calculation is implemented via a simulation that accounts for the experimental acceptance and detector resolutions, uses measured 1H(p,2p) elastic scattering cross section, and does not include ISI/FSI effects. See details below.

Reaction Simulation

In the calculation, the 12C system is treated as spectator plus initial proton, $\mathbf{p}_{12C} = \mathbf{p}_{11B} + \mathbf{p}_i$. The proton's initial momentum distribution in 12C is sampled from a theoretical distribution. Note that all kinematical quantities discussed here correspond to the carbon rest-frame.

In terms of the kinematics, we raffle $|p_i|$ from the total momentum distribution and randomize its direction, cf. Fig. 7.10. The proton's off-shell mass is

$$m_{\text{off}}^2 = m_{^{12}\text{C}}^2 + m_{^{11}\text{B}}^2 - 2m_{^{12}\text{C}} \cdot \sqrt{m_{^{11}\text{B}}^2 + \mathbf{p}_i^2}.$$

The two-body scattering between the proton in 12C and the target proton is examined in their c.m. frame. The elastic-scattering cross section is parameterized from free pp differential cross section data. Following the scattering process, the two protons and 11B four-momenta are boosted back into the laboratory frame.

The two-arm spectrometer was placed such that it covers the symmetric, large-momentum transfer, 90° c.m. scattering region. Given the large forward momentum, the detectors cover an angular acceptance of $\sim 24° < \theta < 37°$ in the laboratory system which corresponds to $\sim 75° < \theta_{\text{c.m.}} < 101°$ in the c.m. frame. In order to compare the simulated data to the experimental distributions, the simulation is treated and analyzed in the same way as the experimental data. Experimental acceptances are included. Resolution effects are convoluted to proton and fragment momenta. The proton time-of-flight resolution $\Delta\text{ToF}/\text{ToF}$ is 0.95% at 2 GeV/c and the angular resolution 5 mrad, while the fragment momentum resolution is 1.5% and the angular resolution 1.1 mrad in the x and y directions. The angular resolution of the incoming beam is 1.1 mrad. The beam-momentum uncertainty, examined as Gaussian profile, does not significantly impact rest-frame momentum distribution as long as the nominal beam momentum is the same used for extracting physical quantities (or observables) from the experimental data and the simulated ion. However, the momentum distributions are dominated by the width of the input distribution. In Figs. 7.9 and 6.11 we show the comparison between data and the simulation for the missing and fragment momenta.

Initial Momentum Distribution from Theory

The initial momentum distributions are calculated in the eikonal formalism for quasi-free scattering as described in Ref. [5]. In this work we compare the data to the momentum-distribution calculated explicitly without absorption effects, i.e. without multiple-scattering. A comparison to the same calculation that includes absorption effects from the imaginary part of the potential explicitly, calculated in the optical limit of Glauber theory, results basically in the same shape. The

distorted waves are calculated from the real and imaginary part of the optical potential for the inter action between proton and nucleus.

The single particle wave function of the removed proton is generated from a Woods-Saxon potential with radius given by $R = 1.2 \cdot A_{1/3}$ fm and diffuseness a = 0.65 fm, while the depth of the potential was adjusted to reproduce the removal energy, S_p = 15.96 MeV, of a proton from the $p_{3/2}$-shell. For the 12C nucleus a density distribution from electron scattering was used as input, assuming that is has the same profile for the proton and neutron densities. The density is of the form $\rho_{12C} = (1+\alpha \cdot (r/b)_2) \cdot \exp(-r_2/b_2)$, with $\alpha = 1.4$ and b chosen so as to reproduce the RMS radius of the 12C, b = 2.47 fm. Although the fragment selection removes events from FSI and we do not need to account for their scattering into measured phase space, we look at the calculation with absorption since the survival probability is larger if the knockout happens at the nuclear surface. This effect might create a difference from no distortions. However, the momentum distributions with and without absorption look very similar, see Fig. 7.11, and do not seem to have a large impact on the reconstructed initial momentum distribution in a light system such as 12C.

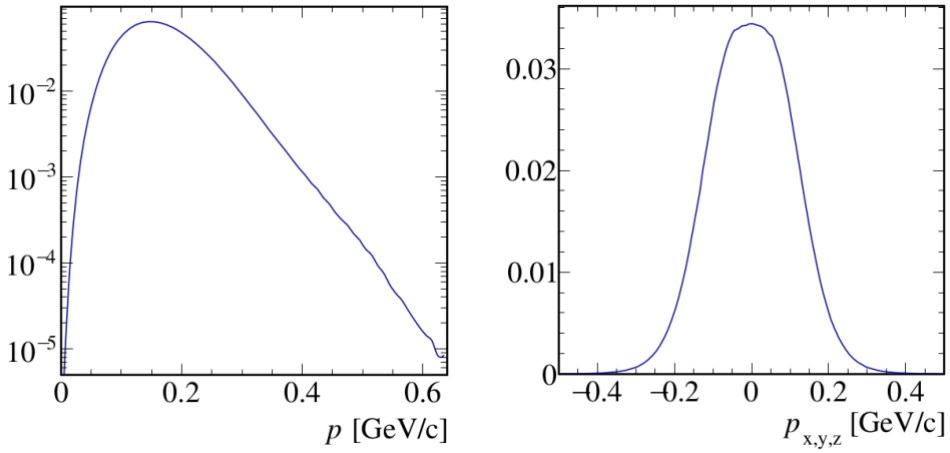

Fig. 7.10: Realistic theoretical p-shell momentum distributions [5] used as input to the simulation.

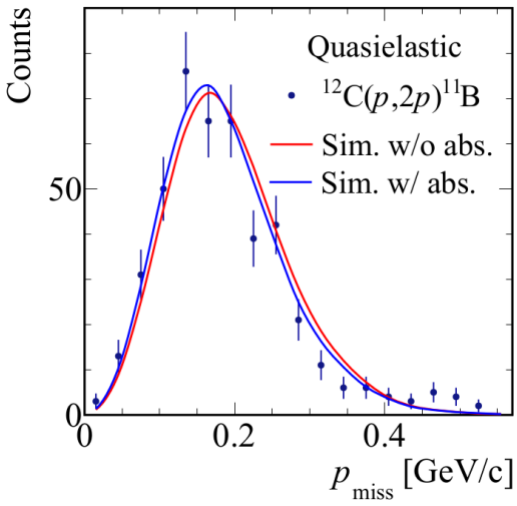

Fig. 7.11: Missing-momentum distribution for quasielastic 12C(p,2p)11B events. The data are compared with single-proton knockout simulation based on momentum distributions from an eikonal calculation with and without including absorption effects in the calculation and normalized to the same integral as the data. See text for details. Both curves agree with the measured data and show only a small difference.

7.5 Ratio Extraction (p,2p)11B / (p,2p)

Our data shows that the 12C(p,2p)11B QE events yield account for (40.3±5.8)% of the total number of 12C(p,2p) QE events. We further measured 12C(p,2p)10B and 12C(p,2p)10Be events that correspond to QE scattering to an excited 11B state that de-excites via neutron or proton emission respectively. These events correspond to (11.1±1.9)% (10B) and ≤ 2% (10Be) of the total number of 12C(p,2p) QE events.

To extract the fraction of (p,2p) events with a detected heavy fragment we need to apply several corrections to the number of measured events which do not cancel in the ratio. The ratio of the exclusive cross section with a detected fragment to the inclusive cross section is given by:

$$\frac{^{12}\mathrm{C}(p,2p)\mathrm{X}}{^{12}\mathrm{C}(p,2p)} = \frac{R}{\epsilon_Z \times \epsilon_{\mathrm{track}} \times att},$$

where

- R is the measured ratio based on the number of QE events in each sample. We added a cut on low missing momentum, p_{miss} < 250 MeV/c, in addition to the missing energy and in-plane opening angle cuts to clean up the inclusive (p,2p) sample, and focusing at the region of small missing momentum.

- ε_Z is the outgoing fragment charge determination efficiency (BC3,BC4). We consider a value of $\varepsilon_Z = (83\pm6)\%$, see discussion above.
- ε_{track} is the outgoing fragment tacking efficiency. We consider a value of $\varepsilon_{track} = (50\pm5)\%$ for 11,10B, and $\varepsilon_{track} = (50 \pm 15)\%$ for 10Be, see discussion above.
- ε_{att} is the attenuation of the outgoing fragment due to secondary fragmentation in the target. After the reaction, the flux of the fragment depends on the remaining distance the fragment needs to travel in the target. The attenuation is given by the reduction of this flux $att = \exp(-\rho \sigma_{tot} z)$, (5) where ρ is the target density and σ_{tot} the total reaction cross section. We evaluate the attenuation factor by taking an average over the 30 cm target length, using $\rho = 0.07$ g/cm3, $\sigma_{tot} = 220\pm10$ mb (assumed to be the same for 10B,10 Be within uncertainty), such that $\varepsilon_{att} = 0.87\pm0.01$.

The total reaction cross section σtot is calculated in eikonal reaction theory [6] using the 11B harmonic-oscillator like density distribution and the NN cross section at 4 GeV/c/u as the input. In a benchmark test it reproduces the measured cross section for 11B+12C at kinetic energy of 950 MeV/u [7] while the beam energy has only a very small impact. We consider the ∼ 5% systematic overestimate of eikonal cross sections compared to measurements as the uncertainty.

From ratio equation above we see that there are four individual contributions to the uncertainty in the ratio of 12C(p,2pX)/12C(p,2p): statistics ΔR, efficiencies (ΔZ and Δtrack) and attenuation (Δatt). In addition, we have a systematic uncertainty due to the event selection cuts. Each event cut was modified over a given σ range and the resulting change in the relative yield was taken as the systematic uncertainty. The 2D E_{miss}-angle cuts were varied as $(2 \pm 1/2)\sigma$, where both these quantities are described by a Gaussian. The cut in missing momentum was varied according to the missing momentum resolution like $p_{miss} < 250\pm50$ MeV/c. We did not observe a significant asymmetry in the measured quantities. Combining these contributions, we obtained the fractions given in the paper with the quoted statistical (stat) and systematic (sys) uncertainties. The single contributions are listed in the Tables below:

Table 7.1: The fractions of exclusive to inclusive (p,2p) low-missing momentum QE events, and the different contributions to the uncertainty; quoting the statistical (R_{stat}), systematic uncertainty (R_{es}) from cut variations (see Table 7.2), charge ID (Z), tracking (track), and target attenuation (att) relative uncertainty. The ratio is given with stat. and syst. uncertainty in the 2nd column.

X	(p,2p)X/(p,2p) (%)	ΔR_{sta} (%)	ΔR_{es} (%)	$\Delta\varepsilon_Z$	$\Delta\varepsilon_{track}$	Δatt
11B	40.3 ± 2.0 ± 5.5	2.0	$\pm_{2.32.2}$	2.9	4.0	0.4
10B	11.1 ± 1.1 ± 1.5	1.1	$\pm_{0.40.4}$	0.8	1.2	0.1
10Be	1.7 ± 0.4 ± 0.5	0.4	$\pm_{0.10.1}$	0.1	0.5	0.0

Table 7.2: The selected cuts for low-missing momentum QE events, the range used for the sensitivity study, and the relative change in the ratios due to variations in the cuts.

Cut	Sensitivity range	$\frac{(p,2p)^{11}\mathrm{B}}{(p,2p)}$	$\frac{(p,2p)^{10}\mathrm{B}}{(p,2p)}$	$\frac{(p,2p)^{10}\mathrm{Be}}{(p,2p)}$
E_{miss} + in-plane opening angle	$2\sigma \rightarrow 2\sigma \pm \sigma/2$	$\pm^{5.41\%}_{5.27\%}$	$\pm^{2.74\%}_{3.76\%}$	$\pm^{3.24\%}_{5.35\%}$
$p_{miss} < 250\ \mathrm{MeV/c}$	$\pm 50\ \mathrm{MeV/c}$	$\pm^{1.85\%}_{1.42\%}$	$\pm^{2.68\%}_{1.78\%}$	$\pm^{1.97\%}_{2.34\%}$
Total		$\pm^{5.72\%}_{5.46\%}$	$\pm^{3.83\%}_{4.16\%}$	$\pm^{3.79\%}_{5.84\%}$

8. Hard Breakup of SRC Pairs

We present below the study of SRCs by selecting exclusive 12C(p,2p)10B and 12C(p,2p)10Be events.

8.1 Event Selection and Results

We start with the two-proton detection imposing the vertex and β cuts mentioned above. The first cut applied to select SRC breakup events is to look at high-missing momentum, $p_{miss} > 350$ MeV/c. The remaining event selection cuts are chosen following a GCF simulation of the 12C(p,2p) scattering reaction off high missing-momentum SRC pairs.

After applying the high-missing momentum cut, we look at the in-plane opening angle between the protons for different cases: (i) inclusive 12C(p,2p) events, (ii) GCF simulated SRC events, (iii) exclusive 12C(p,2p)10B events, and (iv) exclusive 12C(p,2p)10Be events, cf. Fig. 8.1. The GCF predicts relatively large opening angles that guides our selection of in-plane lab-frame opening angle larger than 63° (that also suppresses contributions from inelastic reactions that contribute mainly at low in-plane angles).

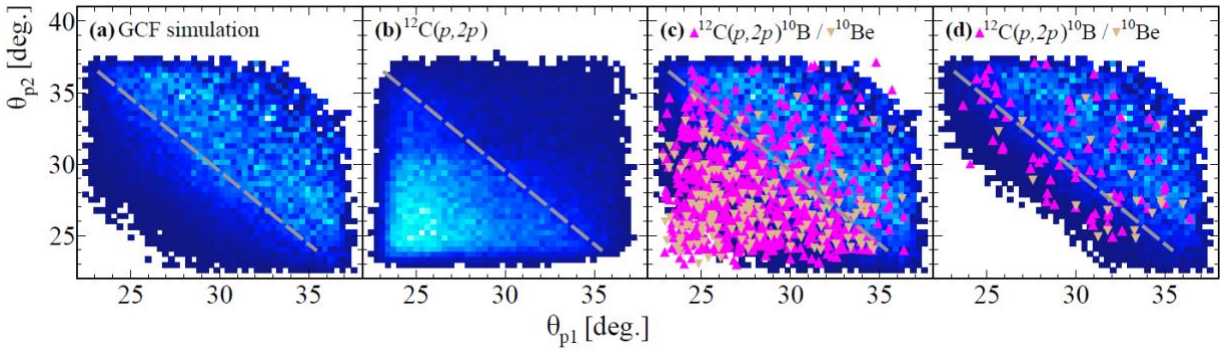

Fig. 8.1: The proton-proton polar angular correlations are shown in (a)-(d) with pmiss > 350 MeV/c, the in-plane opening angle cut to be applied is indicated by the dashed line: (a) GCF simulation, (b) 12C(p,2p) data, (c) 12C(p,2p)10B/Be data on top of simulation, and (d) the same as (c) but with additional Emiss cut.

Next, we apply a missing-energy cut to further exclude inelastic and FSI contributions that appear at very large missing-energies, see Fig. 8.2. To this end we examine the correlation between the missing energy and missing momentum, after applying the in-plane opening angle cut, for the full range of the missing momentum (i.e., without the $p_{miss} > 350$ GeV/c cut). We chose to cut on $-110 < Emiss < 240$ MeV.

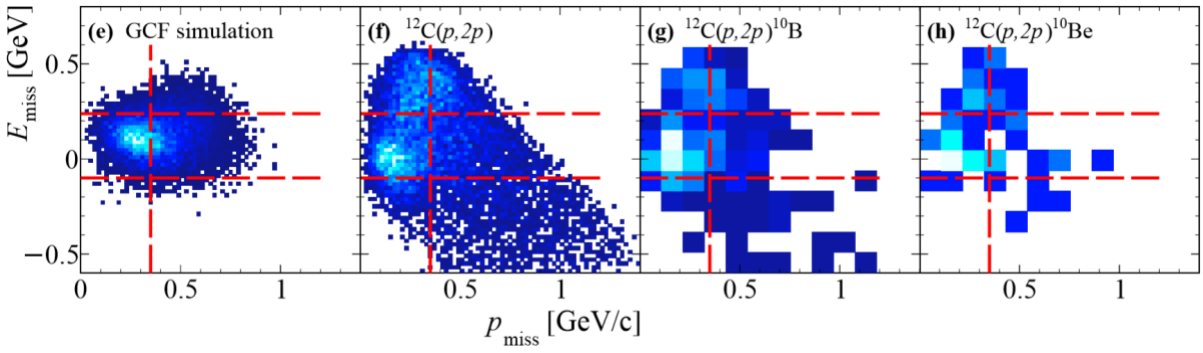

Fig. 8.2: The missing energy vs. missing momentum is shown in (e)-(h): for (e) GCF simulation, (f) 12C(p,2p), (g) 12C(p,2p)10B, and (h) 12C(p,2p)10Be events that pass the in-plane opening angle cut. The selection cuts in −110 MeV< Emiss < 240 MeV and pmiss > 350 MeV/c are indicated by the dashed lines.

To improve the selection cuts we use the total energy and momentum conservation in reactions at which we identified a fragment (10B or 10Be). We can write the exclusive missing-momentum in these reactions as

$$\bar{p}_{\mathrm{miss,excl.}} = \bar{p}_{^{12}\mathrm{C}} + \bar{p}_{tg} - \bar{p}_1 - \bar{p}_2 - \bar{p}_{^{10}\mathrm{B(Be)}}.$$

Neglecting the center-of-mass motion of the SRC pair, the missing-mass of this 4-vector should be equal to the nucleon mass $M^2_{miss,excl.} \sim m^2_N$. The distributions for 12C(p,2p)10B and 12C(p,2p)10Be events that pass the missing-momentum, in-plane opening angle, and missing energy cuts are shown in Fig. 8.3 together with the GCF simulation. To avoid background events with very small values of the missing-mass we choose to cut on $M^2_{miss,excl.} > 420$ MeV^2/c^4. After applying this cut we are left with 26 12C(p,2p)10B and 3 12C(p,2p)10Be events that pass all the SRC cuts.

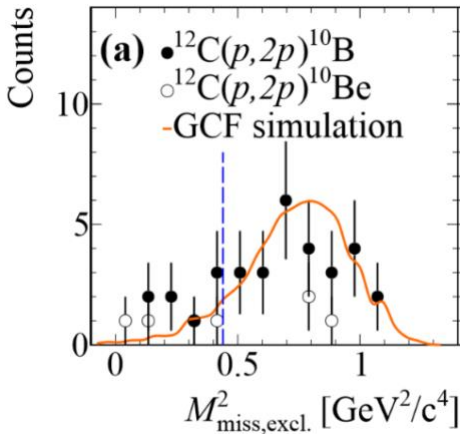

Fig. 8.3: The exclusive missing mass distributions for 12C(p,2p)10B events and 12C(p,2p)10Be events that pass the missing momentum, in-plane opening angle, and missing energy cuts together with the GCF simulation (orange). The blue line represents the applied cut on the exclusive missing-mass $M^2_{miss,excl.} > 0.42$ GeV^2/c^4

Having applied all these selections, we compare the missing and fragment momentum distributions to the GCF simulation for 12C(p,2p)10B, see Fig. 8.4. Overall good agreement is found.

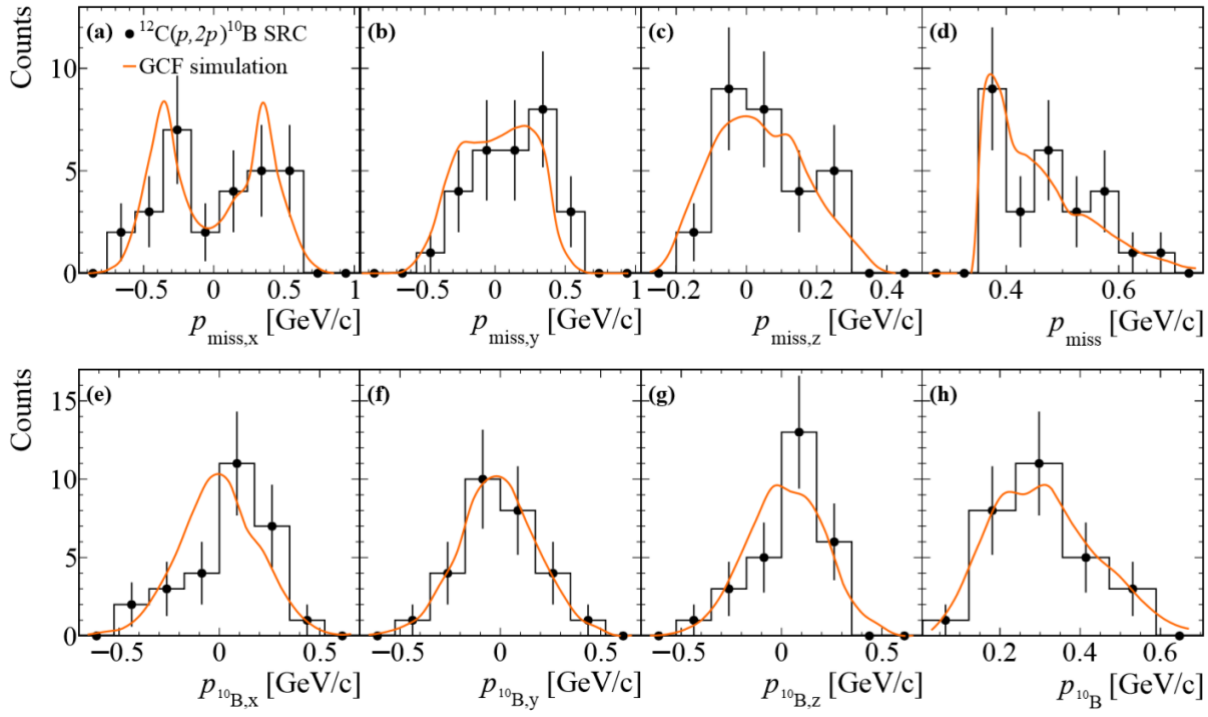

Fig. 8.4: SRC Missing and Fragment Momentum. The missing momentum distributions (a)–(d) for the selected 12C(p,2p)10B SRC events (black) together with the GCF simulation (orange). Acceptance effects, especially in the transverse direction are well captured by the simulation. The lower figures (e)–(h) show the fragment momentum distributions in the rest frame of the nucleus for the same selected 12C(p,2p)10B SRC events (black) together with the GCF simulation (orange).

We note that if the measured SRC events were caused by FSI with a neutron in 11B, we would expect to also detect a similar number of 10Be fragments due to FSI with a proton in 11B. At the high energies of our measurement these two FSI processes have almost the same rescattering cross sections [8]. Our measurement of only 3 10Be events is consistent with the SRC np-dominance expectation and not with FSI. In addition, while our selection cuts suppress QE scattering events off the tail of the mean-field momentum distribution they do not completely eliminate them. Therefore, some events could result from de-excitation of high-pmiss 11B fragments. Using the de-excitation cross-sections of Ref. [25] and the measured number of 12C(p,2p)11B events that pass our SRC selection cuts (except for the exclusive missing-mass cut), we estimate a maximal background of 4 10B and 2 10Be events due to knockout of mean-field protons and subsequent de-excitation.

8.2 GCF Simulations

The Theoretical background for the generalized contact formalism (GCF) is given in Ref. [12-15] and its numerical implementation follows Ref. [16] and was previously used in Ref. [17, 18]. Below we present the main (p,2p)A-2 cross-section equation used for the current analysis and discuss its input parameters.

The A(p,2p)A-2 process is shown in Fig. 8. 5 and its cross-section is modeled in the GCF approximation by:

$$\frac{d^8\sigma^{pA}}{dtd\phi^* dp_{rel} d^2\mathbf{\Omega}_{rel} d^3\mathbf{p}_{CM}} = \frac{v_{12}}{v_{1A}} \frac{1}{2\pi} \frac{d\sigma^{pp}}{dt} \sum_{\alpha} C_{ab}^{\alpha} \frac{|\tilde{\phi}_{ab}^{\alpha}(p_{rel})|}{(2\pi)^3} p_{rel}^2 n(p_{CM})$$

Where p_{rel} and p_{CM} are the SRC pair relative and center-of-mass momentum, C are nuclear contacts defining the number of SRC pairs of type ab (= pp, np) and spin α (= 0, 1) [12-15]. σ_{pp} is the proton-proton elastic scattering cross-section. $n(p_{CM})$ is a three-dimensional Gaussian describing the total pair momentum distribution. $\phi(p_{rel})$ is the pair relative momentum distribution given by the zero-energy solution of the two-body Schrödinger equation. ν are kinematical factors given by $\nu_{tg,i} = \frac{\sqrt{(p_{tg} \cdot p_i)^2 - m_N^2 \tilde{m}_N^2}}{E_{tg} E_i}$ and $\nu_{tg,A} = \frac{|\mathbf{p}_{tg}|}{E_{tg}}$.

The calculation of $\phi(p_{rel})$ is done using the AV18 interaction. $n(p_{CM})$ is calculated using a gaussian width of 150 MeV/c. The nuclear contacts values are taken from Ref. [12], based on many-body quantum monte carlo calculations.

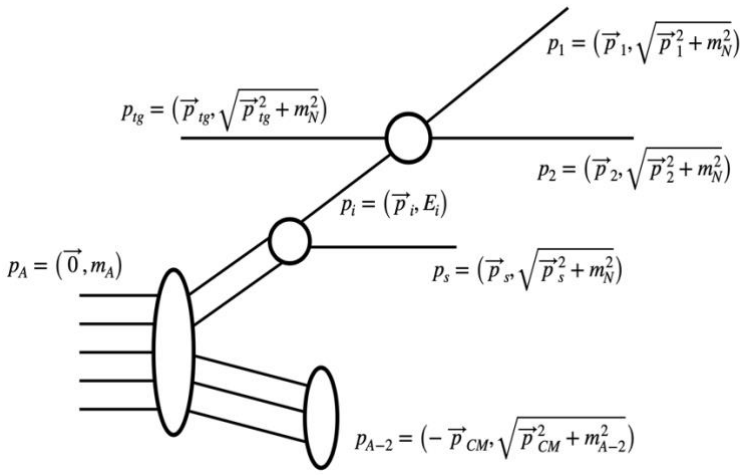

Fig. 8.4: SRC Breakup reaction diagram.

Appendix A – simulation study of sample purity:

We studied in detail to what extend our tracking in the TAS could be contaminated by particles that are not protons after our selection cuts.

Note, that while we do not have particle identification, the measured reactions are exclusive and their kinematics is very specific. Events where a different particle was detected will not show the measured characteristics.

We did the 12C_in 12C_out test. Indeed, such events can produce particles that cause a trigger in the TAS. However, no such events are left after our most basic analysis cuts.

Using the "Dubna Cascade Model and Multifragmentation Model" (DCM-SMM) for a simulation we further explored the possible contamination of our sample by non-proton tracks. We used the simulation to produce a sample of 45M 12C+p events, passed them through our experimental setup, and analyzed them just like the data.

Starting from the QE mean-field:

We applied the same selection cuts, like in the Emiss vs. opening angle selection, see Fig. A.1.

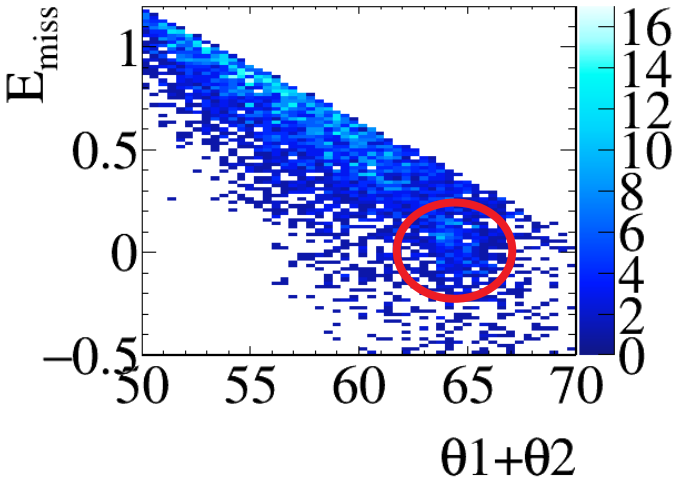

Fig. A.1: Meanfield selection in the DCM-SMM for Emiss and in-plane opening angle.

1. (p,2p): Out of 364 simulated events that pass our selection only 5% (i.e. 19 events) have tracks in the TAS where at least one of the particles is not a proton. We account for this in the extraction of the (p,2p)11B / (p,2p) ratio.
2. (p,2p)11B: all 194 simulated events that pass our selection have two proton tracks in the TAS.

Continuing with SRCs:

For SRC the use of the simulation is more complex. The simulation does not properly model SRCs and therefore cannot fully estimate our 'signal' or Signal:BG ratio. We therefore take a conservative approach and consider the simulation as 100% BG. The applied selection is shown in Fig. A.2.

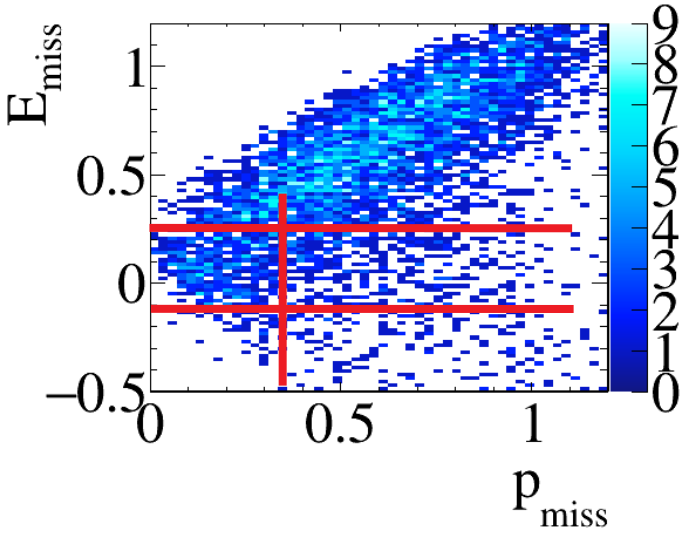

Fig. A.2: SRC selection in the DCM-SMM for Emiss and pmiss.

We normalize the simulation by scaling the simulated event yields for mean-field QE (p,2p)11B events to the measured yield. We then treat the scaled simulated SRC yield as 'BG' to the measured SRC event yield which is our 'signal+BG'. For (p,2p)X events, we account for the fragment detection efficiency when doing the scaling.

Results:

1. (p,2p)10B: The scaled simulation yield equals 7±2 events, all with proton tracks in the TAS. This is consistent with the possible BG we report from 11B de-excitation.

2. (p,2p)10Be: no simulated events pass our selection.

3. (p,2p): The scaled simulation yield equals 760±215 event, where 34% have two protons in the TAS and the rest have at least one track that isn't a proton. Compared with the measured (p,2p) events yield of 2057, this indicates a possible BG of 30% in this channel. This is a non-negligible fraction that has large uncertainty. Unlike the mean-field channels, we can't say if the simulation is reliable for the SRC channel or if it is really all BG or not. We therefore chose to remove the discussion of the SRC (p,2p)10B(10Be) / (p,2p) ratio from the current paper. We might get back to it in future works.

Appendix B – Data quality and good run selection:

Signals from the TAS-TCs were combined with the BC and V-BC scintillators signals to form the main 12C(p,2p) reaction trigger for the experiment. Additional triggers were set up for monitoring and calibration purposes, see Sec. 2. The stability of the trigger was monitored on-line during the experiment as part of our data quality control, see Figs. B.1 and B.2. We collect and recorded about 20 million triggers. The ratio between BC2/BC1 and BC4/BC3 was not smaller than 65%, and the rate on the V-BC is on average 24% relative to BC2. The physics data were taken with a rate of about 180 Hz as measured during a beam pulse duration. Variations of beam detector pulse high over the measurement time was monitored and accounted for in the analysis (see. Sec. 3). No significant run-to-run variations were observed in any of the final observables, see Fig. B.3.

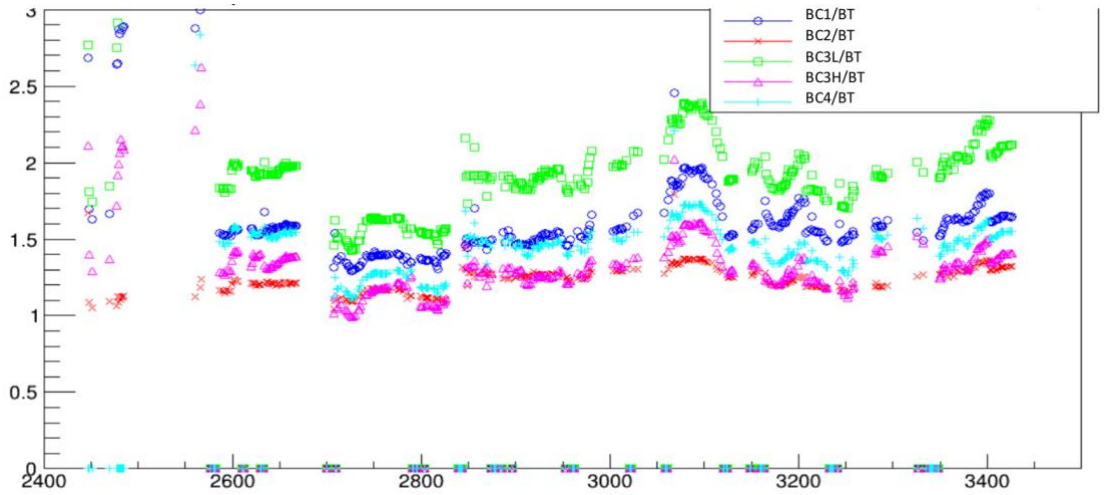

Fig. B.1: Scaler counts for BCs normalized to Beam Trigger (BT) as function of run. In a few runs no scaler values were recorded.

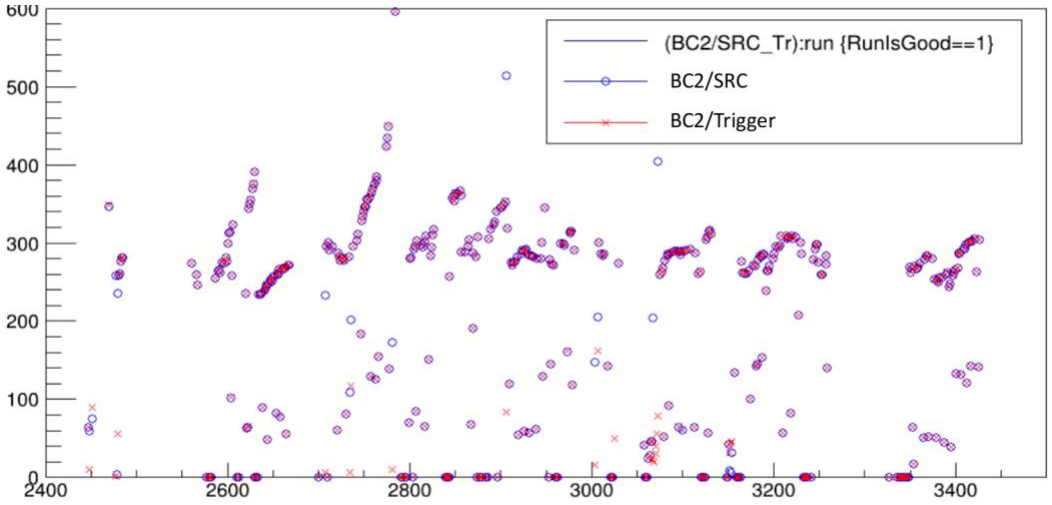

Fig. B.2: Ratio of BC2 scaler to the SRC trigger.

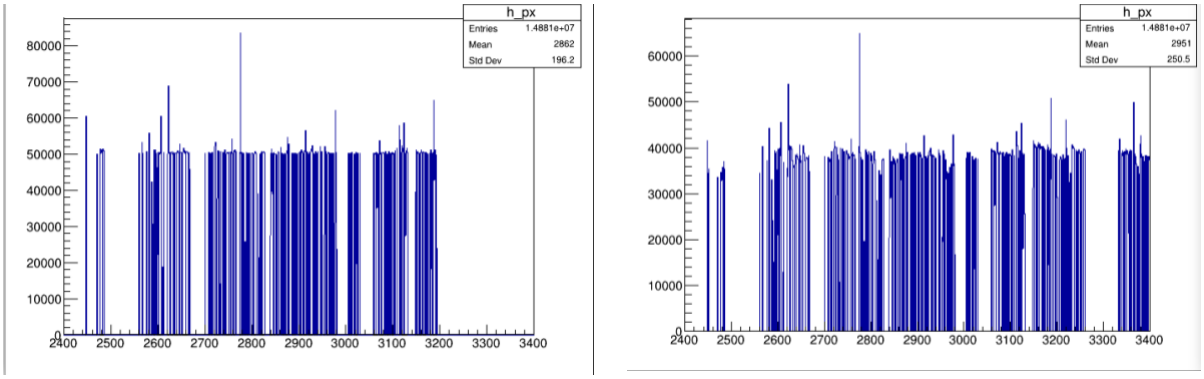

Fig. B.3: (Left) Number of recorded reaction trigger as function of run number, and (right) the number of reconstructed vertices, stable as function of run number.

Appendix C – Response to collaborator comments

C.1 Round 1:

These comments refer to the paper draft circulated to the collaboration, describing the results of the analysis presented in this note. They were sent before the report was fully drafted and available for review.

Comments from Itzhak Tserruya

This is excellent work. The authors present a new method to measure single proton momentum distribution and to identify short range correlation pairs, in C12, free of initial or final state interactions. As such the results deserve to be granted the status of preliminary BM@N results.

However, on the technical or format side, the material presented is not really an Analysis Note. It is hard to follow the description of the experimental set-up and the analysis procedure when the material is split between the main text, the extended data material and the Supplemental Material. The text is well written but the split makes the reading not easy. On the content side, I find that many details are missing both on the description of the experiment and on the data analysis. I also find that some steps could be or should be improved in the analysis chain. In the following I present a list of questions and comments for the authors to consider (the line numbes refer to the version that I received on May 11):

L 4, 7, 16 and several other places: when you talk about distributions do you mean momentum distribution? Pls specify.

This is a delicate point from a theoretical perspective, which is why we intentionally chose to use a more general term.

L 8: need a ref at the end of this sentence.

Many references were missing and are now added. We note that the target journal (Nature) limits the main text to 30 references. A final selection will be done.

L 19: what is quasi-free inverse kinematics?

It means quasi-free scattering, only in inverse kinematics. We now say separate this and say: "…by measuring the quasi-free scattering of 48 GeV/c 12C ions from hydrogen". The inverse-kinematics aspect is mentioned explicitly only later:

"*we use post-selection in high-energy inverse kinematics (p,2p) scattering*"

L 23: would → could?

At the energies of this measurement we think 'would' is appropriate. The draft will soon be sent to theoreticians with expertise in reaction theory who will be able to comment on this point.

L 28: factorization needs explanation

We now say: "*… and establish the separation of the pair wave-function from that of the residual nuclear system*".

L 31: theoretical calculations or simulations?

We think 'calculations' is appropriate. They are implemented as a simulation but that part is technical and trivial, it is the theory input to the simulation that is important.

L 612: what is the interaction length of the hydrogen target?

The interaction length is 215 cm. For our 30 cm long target this corresponds to a 14% interaction length. We now state this explicitly when discussing the target in the Methods section (Liquid-hydrogen target):

"The target constitutes a 14% interaction length for 12C."

L 998: what is the orientation of the X' U' and V' planes?

The same as X,U,V. It is corrected in the text.

"*Each chamber has six planes (X,U,V,X,U,V).*"

L 1021: only 4 of the 8 coordinate planes are defined.

The prime coordinates are the same as the un-prime. It is corrected in the text.

"Each chamber consists of eight coordinate planes, twice {X,Y,U,V}"

L 1083-4: It is more important and significant to know the momentum resolution with the liquid H2 target. In addition to Fig. 2, could you show also the C12 momentum resolution with the liquid H2 target?

We studied the resolution for 12C events that go through the target using our beam-trigger. We found that the resolution is the same as the resolution reported without the target. We now state this explicitly in the text:

"Using this approach, a total-momentum resolution of 0.7 GeV/c for 12C is achieved, as estimated with the empty target data, consistent with the resolution limits of the detection systems, see Fig. 2. The same momentum resolution was obtained for unreacted 12C events, analyzed under the same conditions but with LH2 target inserted."

L 1102: Can you show the distribution of minimum distance between the two proton tracks?

See below for events with an incoming 12C, outgoing fragments with Z_{eff}>3, and beam on target position in {x,y}. The analysis cut of $D <$ 4 cm is shown in red.

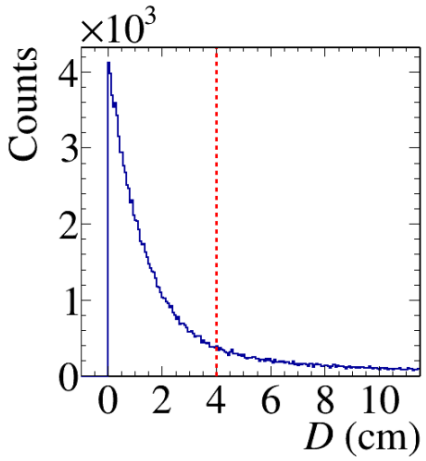

Fig. 1: Vertex minimum Distance.
(Details on multi-tracks on p. 11-12.)

L 1111: Do I understand it properly that tracks are reconstructed in the two arms with two spatial points only and that all reconstructed tracks are assigned the proton mass in the momentum determination?

Yes, we have two points for each track (GEM and RPC hits). The quality of these tracks is evident by the vertex reconstruction, especially of the three foils.

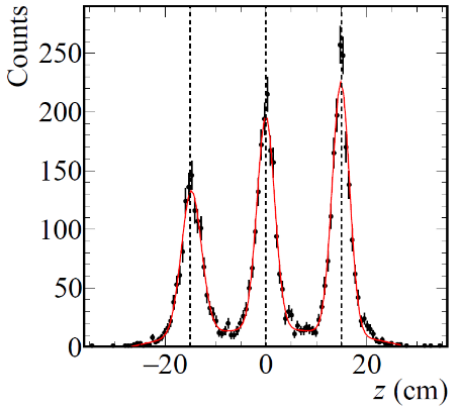

Fig. 2: Vertex in z direction for 3Pb foils. The distance between the foils was 15 cm.

What is the momentum resolution of the proton arms?

The TOF resolution is ~175 ps. This corresponds to a lab-frame proton momentum resolution of ~5.3% at 2 GeV/c and to 60 MeV/c (1σ) in the longitudinal direction of p_{miss} when boosting to the 12C rest-frame. This is now reported in the text (end of supplementary materials section). It was always accounted for in our simulations.

"…*Together with the time-of-flight that is measured between the start counter BC2 and the RPC, the total proton momentum can be determined. For a 2 GeV/c proton this corresponds to ΔToF/ToF ~ 0.95% which translates into a total-momentum resolution of 5.3% in the laboratory system and ~60 MeV/c for the missing momentum from the two protons in the 12C rest frame*."

L 779: How was the total reaction cross section determined? Or give a ref?

We added proper references to the text *(M. Hussein, R. Rego, and C. Bertulani, Phys. Rept. 201, 461 279 (1991).; A. Ozawa, T. Suzuki, and I. Tanihata, Nucl. Phys. A 463 693, 32 (2001).).* We added these details of the calculation to the Methods section.

"The total reaction cross section σtot is calculated in eikonal reaction theory [37] using the 11B harmonic oscillator like density distribution and the NN cross section at 4 GeV/c/u as the input. In a benchmark test it reproduces the measured cross section for 11B+12C at kinetic energy of 950 MeV/u [38] while the beam energy has only a very small impact. We consider the ~ 5% systematic overestimate of eikonal cross sections compared to measurements as uncertainty."

L 811-813: The Introduction speaks about ground state distributions. However, it is clear that the selected residual nuclear fragment is not necessarily in its ground state. You should quote the sigma value of the selected events in order to quantify the quasi-elasticity of the events.

Added mention it in the main text:
"We note that while bound excited states cannot be separated from the ground state in 12C(p,2p)11B events, their contribution is very small [20] and should not impact the measured momentum distribution"

And with a reference to the Methods section that now states:
"We select a bound 11B where the 3/2- ground-state is populated with the largest cross section. However, we cannot distinguish bound excited states that de-excite via -ray emission that are also populated in our experiment. Previous works [20] found the contribution from such states to be small, coming primarily from the 1/2- and 3/2- states that contribute ~10% each to the total cross section. This contribution also corresponds to p-shell knockout and does not impact the resulting momentum distribution significantly."

L 827-828: What is the phi acceptance of the two proton arms? The distribution shown in Extended data Fig. 2c could just be an artifact of their limited acceptance?

It is not, as evident by the comparison with event mixing shown below by the red histogram.

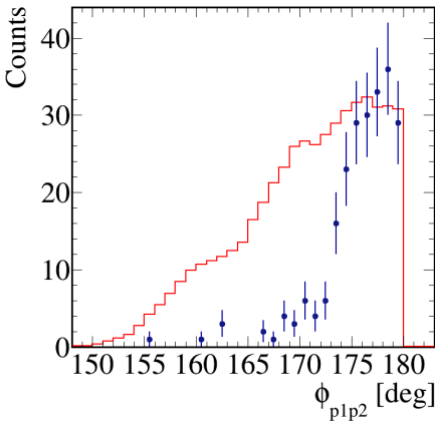

Fig. 3: Off-plane opening angle.

L 880: you should quote the value of R as defined in eq. 4 with its statistical and systematic uncertainty. The latter is not at all discussed in the material presented. It should be estimated by a thorough study based on variations of the cuts that may affect differently the exclusive and inclusive reactions.

The ratios and uncertainties are now evaluated more thoroughly in the Method Section, see discussion following Eq. 4. The tables requested are given below.

L 905: why the fragment attenuation factor was calculated at the center of the hydrogen target instead of performing a proper average over the entire target length?

We now integrate over the target length. The resulting average attenuation factor is now 0.87 ± 0.01.

L 209-216: the fractions quoted in this paragraph are significantly different from those quoted in the Extended data right before L 909. Why is that so? Also the uncertainties quoted in this paragraph are different (in particular for the 11B case) from those quoted in the Extended data before L 909?

It was a typo that is now fixed. All number are now consistent.

Where are the statistical errors and where are the systematic errors in these fractions? They should be quoted separately.

Done. See the Tables below:

Table 1: The fractions of exclusive to inclusive (p,2p) low-missing momentum QE events, and the different contributions to the uncertainty; quoting the statistical (R_{stat}), systematic uncertainty (R_{es}) from cut variations (see Table 2), charge ID (Z), tracking (track), and target attenuation (att) relative uncertainty. The ratio is given with stat. and syst. uncertainty in the 2nd column.

X	(p,2p)X/(p,2p) (%)	ΔR_{sta} (%)	ΔR_{es} (%)	$\Delta\varepsilon_Z$	$\Delta\varepsilon_{track}$	Δatt
11B	40.3 ± 2.0 ± 5.5	2.0	$\pm_{2.32.2}$	2.9	4.0	0.4
10B	11.1 ± 1.1 ± 1.5	1.1	$\pm_{0.40.4}$	0.8	1.2	0.1
10Be	1.7 ± 0.4 ± 0.5	0.4	$\pm_{0.10.1}$	0.1	0.5	0.0

Table 2: The selected cuts for low-missing momentum QE events, the range used for the sensitivity study, and the relative change in the ratios due to variations in the cuts.

Cut	Sensitivity range	$\frac{(p,2p)^{11}B}{(p,2p)}$	$\frac{(p,2p)^{10}B}{(p,2p)}$	$\frac{(p,2p)^{10}Be}{(p,2p)}$
E_{miss} + in-plane opening angle	$2\sigma \rightarrow 2\sigma \pm \sigma/2$	$\pm^{5.41\%}_{5.27\%}$	$\pm^{2.74\%}_{3.76\%}$	$\pm^{3.24\%}_{5.35\%}$
$p_{miss} < 250$ MeV/c	± 50 MeV/c	$\pm^{1.85\%}_{1.42\%}$	$\pm^{2.68\%}_{1.78\%}$	$\pm^{1.97\%}_{2.34\%}$
Total		$\pm^{5.72\%}_{5.46\%}$	$\pm^{3.83\%}_{4.16\%}$	$\pm^{3.79\%}_{5.84\%}$

L 919-920: you should show the opening angle distributions for the four cases considered to justify the angular cut used.

Done, cf. Extended Data Fig.4.

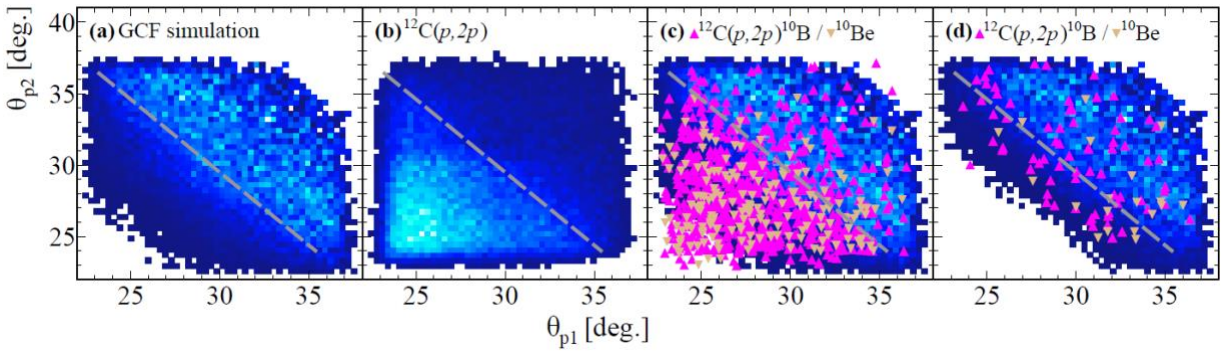

Fig. 4: The proton-proton polar angular correlations are shown in (a)-(d) with pmiss > 350 MeV/c, the in-plane opening angle cut to be applied is indicated by the dashed line: (a) GCF simulation, (b) 12C(p,2p) data, (c) 12C(p,2p)10B/Be data on top of simulation, and (d) the same as (c) but with additional Emiss cut.

Fig.4a needs more explanation: the scatter plot shows triangles of two kinds and squares and it is not clear from the figure caption what do they represent.

We revised the figure in general, and also edited the caption with respect to the symbols.

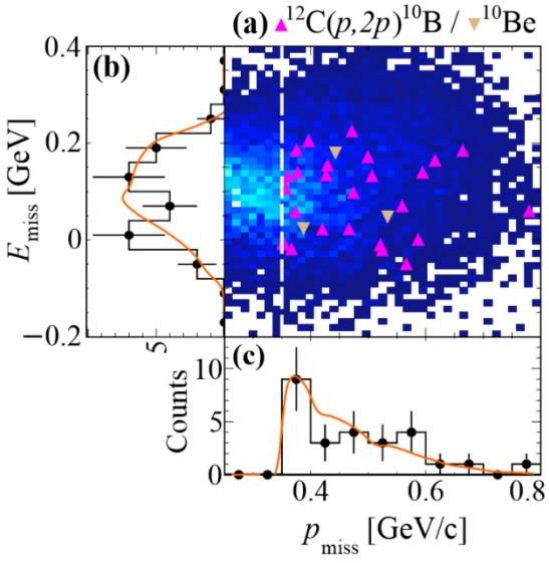

Fig. 5: SRC Selection in missing momentum and energy. (a) Correlation between the missing-energy and missing-momentum for the measured 12C(p,2p)10B (upwards facing purple triangles) and 12C(p,2p)10Be (downwards facing brown triangles) selected SRC events, on top of the GCF simulation (color scale). (b) and (c) one dimensional projections for the measured (black points) and GCF simulated (orange line) missing-energy (b) and missing-momentum (c) for 12C(p,2p)10B. Data error bars show statistical uncertainties at the 1σ confidence level. *Should we show it assuming Poisson distribution?*

Extended data Fig.4a: the p_miss > 350 MeV/c cut seems to miss most of the SRC yield. Can you better justify this cut? Or am I missing something?

While there are SRC pairs at low momentum, they are 'buried' under the many more mean-field nucleons that dominate this part of the momentum distribution. We now explain this in the text.

"An interaction with a nucleon that is part of an SRC pair will be significantly different. The high relative momentum of nucleons in SRC pairs leads to a large value of pmiss that is largely balanced by a single correlated nucleon, as oppose to the entire A-1 nucleons system. Therefore, we require |pmiss| > 350 MeV/c to select SRC breakup events that are far enough from the Fermi level where contributions from meanfield nucleons are negligible. IE events where the high-pmiss is caused by the production of additional particles or by QE interaction followed by FSI that knock out a neutron from the 11B fragment will not be suppressed by this requirement. IE interactions can be suppressed by requiring a large in plane opening angle between the protons measured in the (p,2p) reaction and restricting the missing-energy of the reaction …"

We do hope to be able to access such 'low Pmiss pairs' using fully exclusive measurements, but this goes beyond the scope of the current paper.

Fractions of SRC events quoted at the end of the Extended data section:

-The variation of the opening angle cut by 1 deg seems very small.

It is actually quite large compared to the acceptance of the detectors as can be seen in Extended Data Fig. 4. However, we removed the discussion about SRC ratios due to the reasons given below.

You should quote separately the statistical and systematic uncertainties.

We have done this, but also removed this discussion due to the reasons given below.

Some of the cut variations (for example the p_miss cut) seem to have an asymmetric effect in the SRC yield. This should be reflected in asymmetric uncertainties in the SRC fractions.

We examined the asymmetry and found it to be very small, also in the meanfield case. We refer to it in the Methods section:

"In the following we quote symmetric uncertainties since we did not observe in the simulation a significant asymmetry in the measured quantities. Combining these contributions we obtain the following fractions given with statistical (stat) and systematic (sys) uncertainties…"

- I suggest to make a table with the values of the fractions of SRC events obtained by the variation of each cut.

We have selected not to report on (p,2p) results for the SRC case.

Some additional comments or missing information:

- Weakness of the analysis: the proton arms do not have real particle identification Capabilities and it is assumed that all reconstructed tracks are proton tracks. The analysis is lacking a full GEANT detector simulation of generated events. Such simulations would allow to determine the proton track reconstruction efficiency, the purity of the proton sample and the amount of background under the quantities measured. The addition of SRC pairs in the simulated events would also allow to determine the acceptance and reconstruction efficiencies of SRC pairs. This type of simulation would greatly enhance the value of the results and could pave the way to allow the determination of absolute cross sections or probabilities.
    1. Our observables are not sensitive to the TAS efficiency. It is true that full Geant simulation will allow quantifying it and report absolute cross-section. However, this work goes beyond the scope of the current paper and includes additional challenges having to do with scalar readout and others. It is part of our plan for future publications.

    2. While we do not have particle identification, the measured reactions are exclusive and their kinematics is very specific. Events where a different particle was detected will not show the measured characteristics.

We did the 12C_in 12C_out test (see Fig. 12 below). Indeed, such events can produce particles that cause a trigger in the TAS. However, no such events are left after our most basic analysis cuts.

Using the "Dubna Cascade Model and Multifragmentation Model" (DCM-SMM) for a simulation we further explored the possible contamination of our sample by non-proton tracks. We used the simulation to produce a sample of 45M 12C+p events, passed them through our experimental setup, and analyzed them just like the data.

Starting from the QE mean-field:

1. (p,2p): Out of 364 simulated events that pass our selection only 5% (i.e. 19 events) have tracks in the TAS where at least one of the particles is not a proton. We account for this in the extraction of the (p,2p)11B / (p,2p) ratio.
2. (p,2p)11B: all 194 simulated events that pass our selection have two proton tracks in the TAS.

Continuing with SRCs:

For SRC the use of the simulation is more complex. The simulation does not properly model SRCs and therefore cannot fully estimate our 'signal' or Signal:BG ratio. We therefore take a conservative approach and consider the simulation as 100% BG.

We normalize the simulation by scaling the simulated event yields for mean-field QE (p,2p)11B events to the measured yield. We then treat the scaled simulated SRC yield as 'BG' to the measured SRC event yield which is our 'signal+BG'. For (p,2p)X events, we account for the fragment detection efficiency when doing the scaling.

Results:

1. (p,2p)10B: The scaled simulation yield equals 7±2 events, all with proton tracks in the TAS. This is consistent with the possible BG we report from 11B de-excitation.

2. (p,2p)10Be: no simulated events pass our selection.

3. (p,2p): The scaled simulation yield equals 760±215 event, where 34% have two protons in the TAS and the rest have at least one track that isn't a proton. Compared with the measured (p,2p) events yield of 2057, this indicates a possible BG of 30% in this channel. This is a non-negligible fraction that has large uncertainty. Unlike the mean-field channels, we can't say if the simulation is reliable for the SRC channel or if it is really all BG or not. We therefore chose to remove the discussion of the SRC (p,2p)10B(10Be) / (p,2p) ratio from the current paper. We might get back to it in future works.

- What is the size of the beam or the beam profile?
  4cm diameter (Extended Data Fig. 1c). We state it in the Methods section.
  "…They are focused on the target with a beam diameter of about 4 cm…"

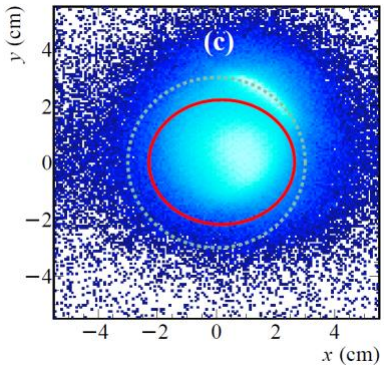

Fig. 6: Beam profile on target.

- How many events were recorded?
  About 20 million events with a reaction trigger.

- There is no QA analysis of the data recorded. How many events were analyzed?
  We added a paragraph to the Methods Section.

"Data Taking and Quality.

Signals from the TAS-TCs were combined with the BC and V-BC scintillators signals to form the main 12C(p,2p) reaction trigger for the experiment. Additional triggers were set up for monitoring and calibration purposes, see online Supplementary Materials for details. The stability of the trigger was monitored on-line during the experiment as part of our data quality control. We collected and recorded about 20 million triggers. The ratio between BC2/BC1 and BC4/BC3 was not smaller than 65%, and the rate on the V-BC is on average 24% relative to BC2. The physics data were taken with a rate of about 180 Hz as measured during a beam pulse duration. Variations of beam detector pulse heigth over the measurement time was monitored and accounted for in the analysis. No significant run-to-run variations were observed in any of the final observables"

- The systematic uncertainties should be analyzed and presented more thoroughly.
  Done, detailed in the Methods section, cf. also Tables 1 & 2 above for the meanfield case.

"From Eq. 4 we see that there are four individual contributions to the uncertainty in the ratio of

12C(p,2pX)/12C(p,2p): statistics ΔR, efficiencies ($\Delta\varepsilon_z$, and $\Delta\varepsilon_{track}$) and attenuation ($\Delta att$). In addition, we have a systematic uncertainty due to the event selection cuts. Each event cut was modified over a given range and the resulting change in the relative yield was taken as the systematic uncertainty. The 2D Emiss-angle cuts were varied as $(2\pm1/2)\sigma$, where both these quantities are described by a Gaussian. The

cut in missing momentum was varied according to the missing momentum resolution like pmiss < 250±50 MeV/c."

- How sensitive are the results to variations of the beta selection cuts on the proton tracks?
  The figure below shows the beta distribution for the two particles identified in the arms with all analysis cuts applied except for the beta selection cuts. Practically all resulting events pass our beta selection cut marked by the red square in the figure below. Thus, our final results like momentum distributions etc. are not sensitive to this selection cut.

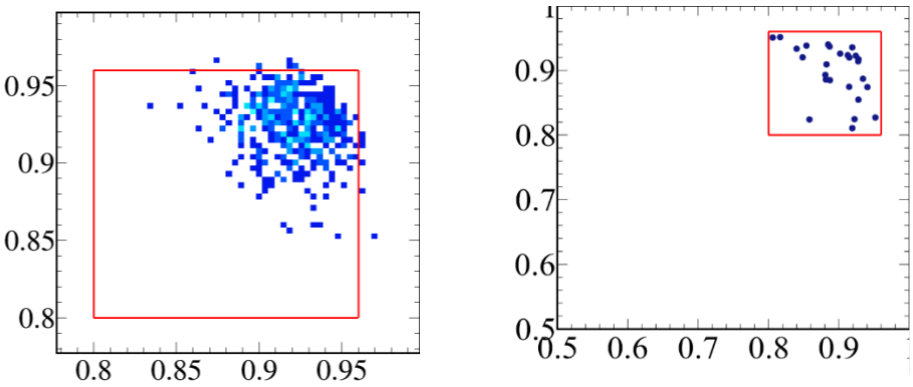

Fig. 7: Beta1 vs. Beta2, left vs. right arm. Left: for meanfield 11B events. Right: with SRC selection (10B) and $|t|,|u| > 1.2$ GeV² where the $|t|,|u|$ cut remove the low beta events.

- Could you show the distributions of track multiplicities in the RPC and GEM detectors and their correlations i.e # of tracks in RPC vs. # of track in GEM.
  Most events considered in our analysis (80%) have hit multiplicity of 1 in each detector, where a hit is a cluster determined by the BM@N tracking algorithm. For the remaining 20% of the event we choose the 'correct' track as the one that results in the smallest distance between the left and right arm tracks intersection. The method follows this scheme:

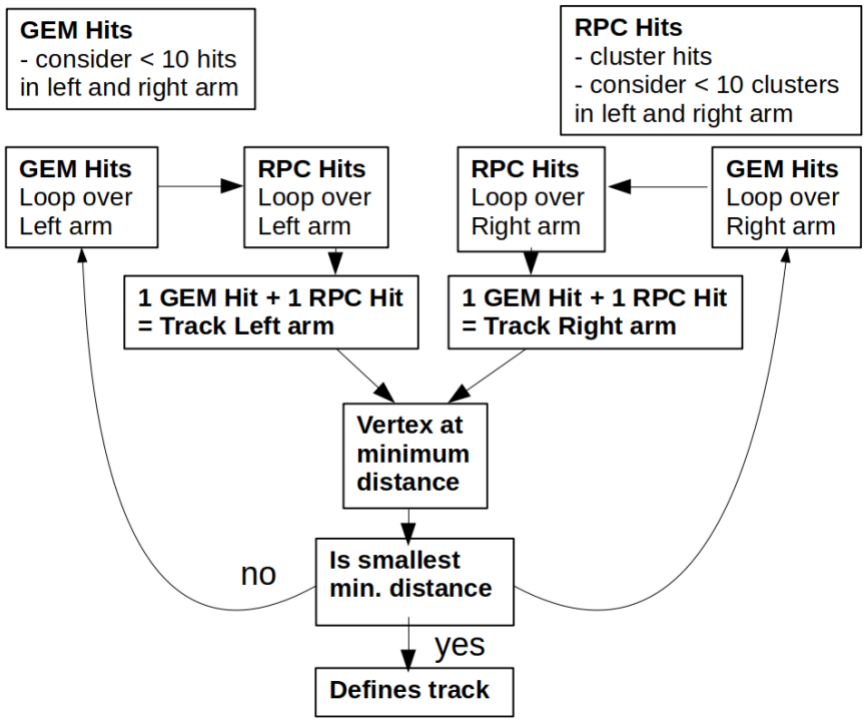

Fig. 8: Vertex reconstruction scheme.

We examined what would happen if we choose the 2nd best track that still satisfies the 4 cm difference cut we apply in the data analysis process. No visible impact is seen. We studied it further and find that its simply because these tracks are essentially the same and result from small 'leftovers' of the clustering algorithm. The difference in their momentum follows a Gaussian distribution with sigma <5 MeV/c. Similarly, their angles are practically identical. Plots are shown below.

Multiplicity distribution for mean-field QE events:

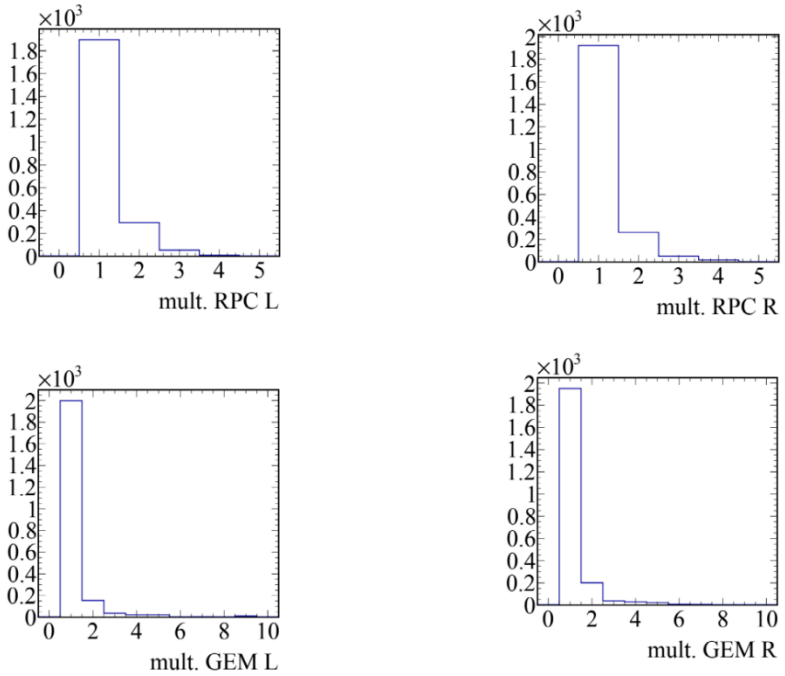

Fig. 9: Multiplicity distribution for RPC (top) left (L) and right (R) arm, and GEM (bottom) left and right.

Distance between the second smallest approach and the minimal approach vertices:

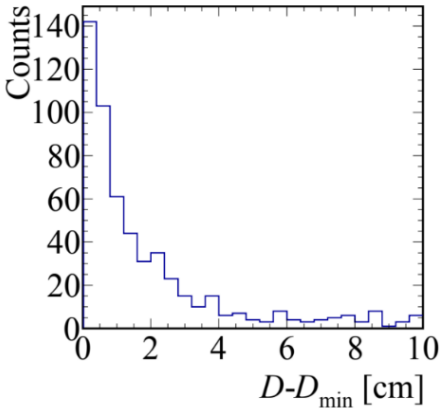

Fig. 10: Minimal distance difference to second smallest D

Momentum difference between minimal approach vertex and the second closest approach vertex with $(D\text{-}D_{min}) < 4$ cm:

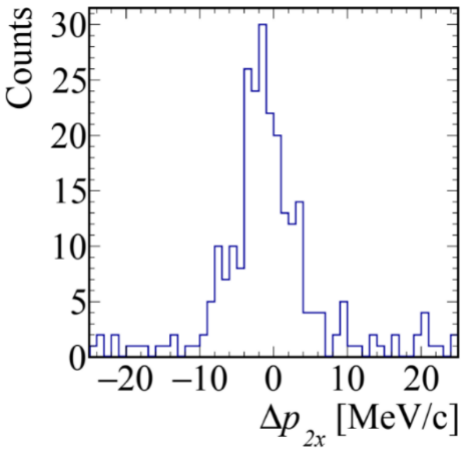

Fig. 11: Momentum difference, example in p_x of right arm.

Results for SRC selection look the same only with less statistics

- Fig. 1b: could you quote the relative abundances of 11B, 10B and 10Be?
  We don't intend to quote the relative abundances in the analysis presented in this draft.

- What would you get in Figs. 2b and 3a if instead of asking for a 11B fragment to be in coincidence with the two arms you ask for a 12C fragment?
  See below. Left: 12C incoming and vertex cut and velocity cuts on the proton tracks. Right: additional quasielastic cut in E_{miss}, opening angle, and M_{miss} as applied in the physics analysis, no events above background level (2% ~ 12C/11B) are left for 12C.

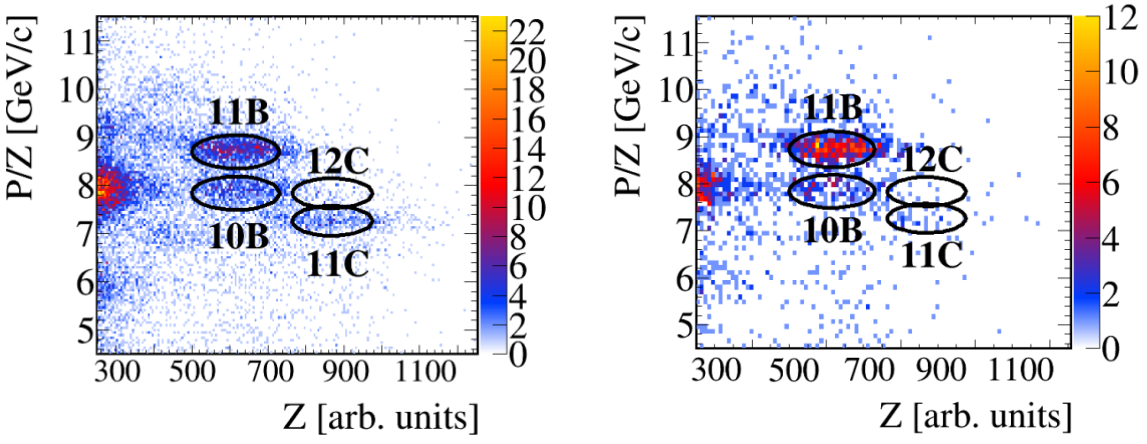

Fig. 12: Fragment identification, right with additional quasielastic selection cuts.

Following the discussions on June 1st:

We show in the following the energy-momentum conservation for the quasielastic reaction:

$P_{12C} + P_{target} - P_{11B} - P_{p1} - P_{p2}$,

using the lab frame variables. The distributions are compared to our *p*-shell p2p simulation (red line). The single momentum components and the energy are shown.

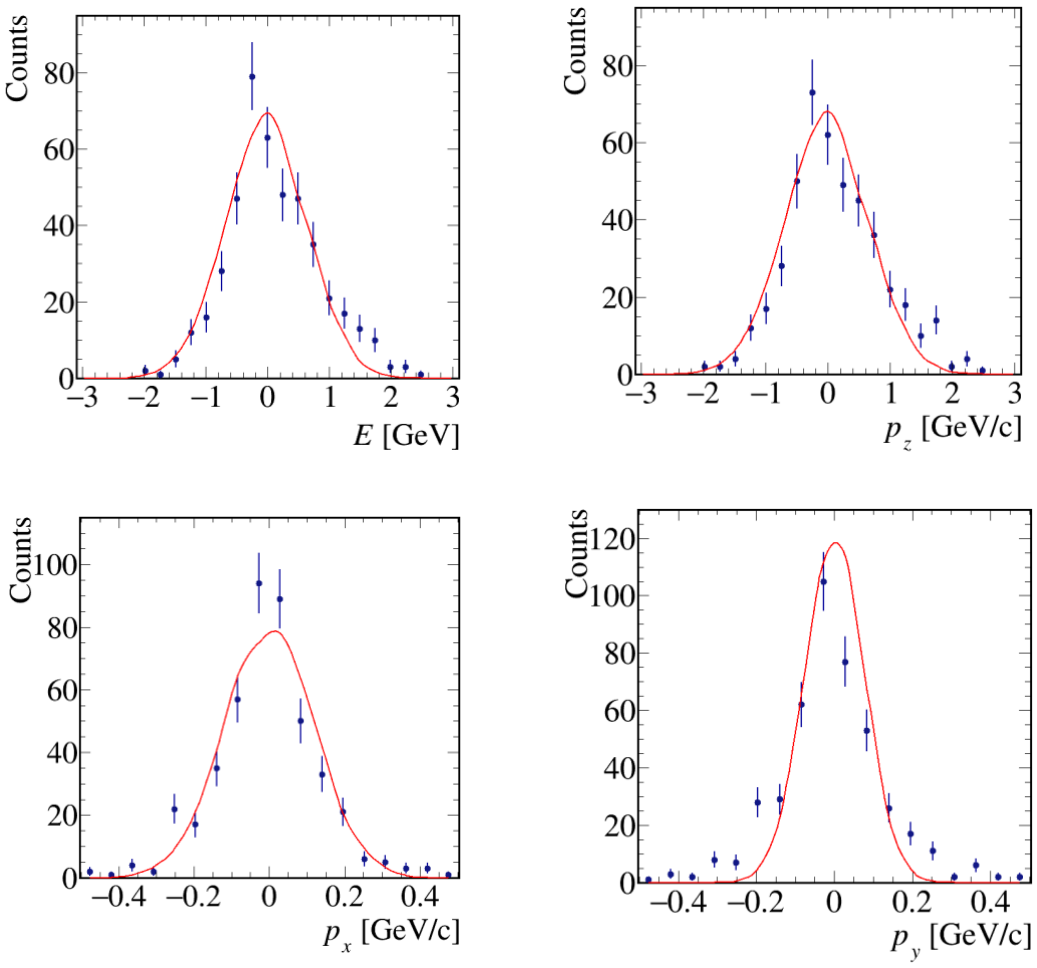

Fig. 16: Four-vector components from energy-momentum conservation in the quasielastic 12C(p,2p)11B reaction, compared to simulation (red line).

Note that when no resolution is included, the simulation reproduces a delta distribution.

Comments from Mikhail Kapishin

- Need plot showing the p_miss resolution and Mx_miss^2 distribution in simulation compared with the data Mx2 distribution to justify the statement that resolution effects are taken into account in the QE p_miss simulation spectrum.
  Extended data Fig. 3 a – h show the P_miss distribution compared with simulation.

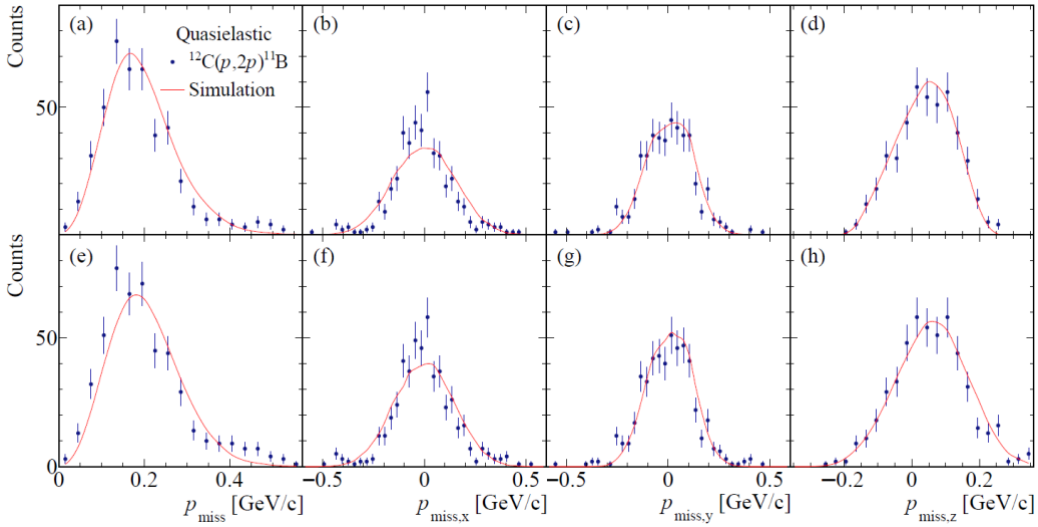

Fig. 13: pmiss distributions and their components. e-h show the same distributions

but with missing mass cut only (0.55 $GeV^2/c^4 < M^2miss < 1.40\ GeV^2/c^4$).

The missing mass spectra for data and simulation is shown below. The simulation is slightly narrower than the data.

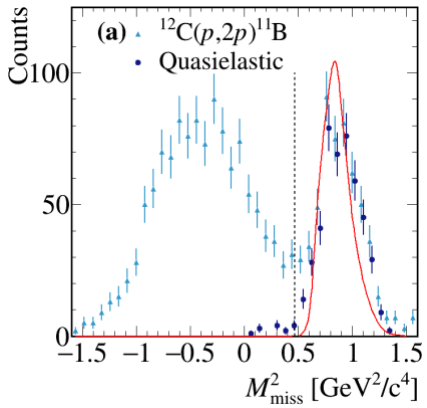

Fig. 14: Missing mass distribution for quasielastic events (dark blue) compared to simulation (red line).

- Provide two dimensional distribution of E_miss vs p_miss for mean field simulation to justify SRC selection ranges in E_miss and p_miss.
  See below mean field 11B simulation with indicated SRC cuts. As can be seen, the mean-field tail that extends to the SRC region is very small and is completely suppressed by the A=10 requirement.

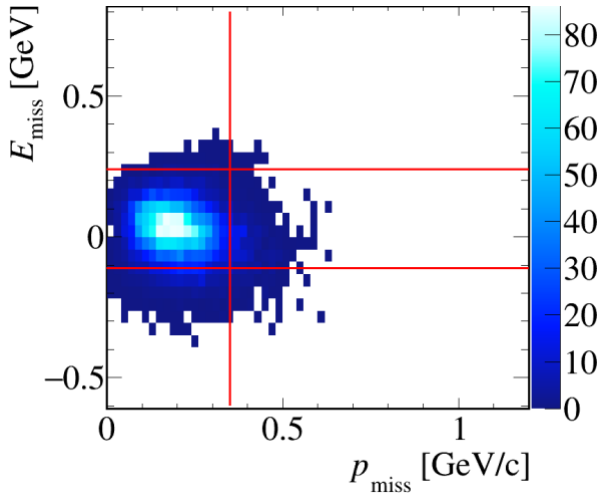

Fig. 15: Meanfield simulation.

- Clarify seeming contradiction between the claimed high efficiencies in the upstream / downstream detectors (MWPC/Si and DCH) ~97% and the track reconstruction efficiency of ~50%
  We added a breakdown of the detector and tracking efficiency in the Supplementary Material. Matching a global track from upstream detectors to DCH reduces the efficiency from 91.4% to 69.7%, and another reduction to 50% comes from the constraints we put in the analysis (like a single global track) and a reasonably reconstructed P/Z. Those values were obtained from a 12C empty-target run and estimated for other nuclear charges. See table below.

Table 3: Contributions to the tracking efficiency.

Good track	ϵ_{track}
$Z_{\text{in}} = 6$, $Z_{\text{eff}} = 6$	100%
Upstream track	98.3%
DCH track	92.7%
Upstream and DCH tracks	91.4%
Global track	69.7%
Good P/Z	50.0%

- Make comment in the paper about possible contribution to B10 from B11 -> B10
  Done.

- and losses of B11, B10, Be10 reaction due to interactions after the target in MWPC / Si / GEM detectors
  In the main text we state the possible scenarios that populate 10B coming from 11B. It can be produced by second-step FSI which however is not consistent with the observed ratio between 10B and 10Be. Contamination from mean field events that left 11B in an excited state above the neutron-separation threshold are also possible. We estimated 4 background events of this kind (compared to 26 measured events) based on known experimental cross sections and given our analysis procedure. We also present the details in the Methods section.

  The material budget downstream the target adds only a small reaction probability compared to the LH2 target. We calculated a reaction probability of about 5% from the 2 MWPCs, the Silicon detectors, and the 2 BCs. The GEMs and DCHs add only another 0.5%. The cross section of 11B+12C is about 800 mb as calculated in eikonal theory (same framework as for 11B+p) and scaled according to (A/12)^1/3. In terms of reaction probability for SRC events, the 5% are only a small contribution compared to the statistical uncertainty.

"Last, as our selection cuts suppress, but do not eliminate events originating from the tail of the mean-field distribution, some events could result from de-excitation of high-pmiss 11B fragments. To evaluate that fraction, we consider 11B events that pass the SRC selection cuts (except for the exclusive missing mass cut). 39 such events are observed, of the total 424 MF 11B events (i.e. a fraction of 9%). Reference [25] measured a neutron (proton) evaporation cross-section relative to the total continuum cross-section of 17% (7%). Using these fractions we expect a 10B (10Be) contribution from neutron (proton) evaporation based on the measured 11B events of 39·(36%/53%)·17% = 4 events (39·(36%/53%)·7% = 2). This is the maximum number that can be expected from this background, since for 10B and 10Be we apply an additional cut on the exclusive missing mass as explained above."

- If anti-BC3high was indeed included into the IT logics of the main SRC triggers SRCT Full and SRCT2 Full, then its efficiency to accept events with final B11, B10, Be10 has a rather big impact to the measured ratio of (p,2p) A-1,A-2 / (p,2p). Vasilisa Lenivenko measured the antiBC2high efficiency for Z<=4 final states of only 46%.
  The anti-BC3high requirement is only meant to suppress very heavy fragments ($Z \geq 6$). The number that Vasilisa quotes is the efficiency for rejecting such heavy fragments. It does not impact the detection of lighter fragments.

Comments to the draft version jinr_v15

Line 585 : 3 x 10^5 -> up to 2 x 10^5

We now state that *on average* the accelerator provided 2.5×10^5 ions per spill (based on what we got from the scalers).

Line 621-622: 90 degree -> put right angular acceptance range

Done.

Line 647: z position (along the beam line)

Done.

Line 667: choosing -> excluding the strong peak

Done.

Line 679: QFS is defined only at line 773

Done.

Line 770: the uncertainty is obtained from examining different energy-deposition cuts of 2 - 5 sigma.

Done.

Line 806: Emiss = mp – emiss should be defined much earlier to describe Fig.2

Together with Eq. 2 we now say:

"…the measured missing energy Emiss = mp - emiss (where emiss is the energy component of pbar_miss in the 12C rest-frame) …"

Line 856: proton time-of-fight resolution is 0.9%

The proton time-of-flight resolution ΔToF/ToF is 0.95% at 2 GeV/c. That corresponds to ~5.3% at 2 GeV/c in the lab frame and is driven by the TOF resolution. This translates into 60 MeV/c (1σ) in the longitudinal direction of p_{miss}. Details are given now in the Supplementary Material.

Reply to Comments from Vladimir Yurevich

1. Lines 100 – 108 have to be replaced with. The beam was monitored before the target using a set of thin scintillator-based beam counters (BC1, BC2, and VC) and two multiwire proportional chambers (MWPCs) used for trajectory and charge identification for each event. The BC2 closer to the target was also used to dene the event start time t0 and the VC with a hole for the beam was used to discriminate nuclear interactions of carbon ions in beam line and to reject events with halo particles.

We only give a very general overview of the setup in the main text. We added a phrase mentioning the Veto counter. The details are outlined in the Methods section and Supplementary Material.

"Beam halo interactions were suppressed using a dedicated BC veto counter (V-650 BC), consisting of a scintillator with a 5 cm diameter651 hole in its center."

"A veto-counter with the dimensions of 15 cm x 15 cm x 0.3 cm and a hole of 5 cm in diameter was located between BC2 and the target. It was read out by an XP2020 PMT and was included in the reaction trigger to suppress the beam halo"

2. Lines 143 – 145, I propose to make a small change in the text: and energy deposition in two scintillators of beam counters BC3 and BC4 placed in about 1 m behind the target, see Fig. 1b.

We don't think such detail is needed in the main text.

3. A small change is needed in the fig. 1 because the beam detector setup is not correct. The BC2(T0) and VC have to be added in front of the target.

BC2 and VC are placed directly in front of the target and are hidden by the cartoonish proton. The orange line indicated their existence there. Note that we describe in the text the VC as part of the BCs so its accounted for by that line.

C.2 Round 2:

As with round 1, the comments below only refer to the paper draft and thee response of round I.

Comments from Itzhak Tserruya

Comments on round-1 response:

1)

L 4, 7, 16 and several other places: when you talk about distributions do you mean momentum distribution? Pls specify.

This is a delicate point from a theoretical perspective, which is why we intentionally chose to use a more general term.

This answer is not clear to me. Distribution by itself doesn't mean anything unless you specify what distributions you are talking about. What is delicate about specifying it?

Our community, especially theorists, is very sensitive to experimental works that claim to be 'measuring momentum distributions'. Momentum distributions are not quantum mechanical observables, but they are extractable under certain assumptions and in specific conditions. It is our vast experience that stating 'momentum distributions' already in the abstract can lead to issues in the review process which we prefer to avoid by using more general terms in this early stage of the text.

2)

L 811-813: The Introduction speaks about ground state distributions. However, it is clear that the selected residual nuclear fragment is not necessarily in its ground state. You should quote the sigma value of the selected events in order to quantify the quasi-elasticity of the events.

Added mention it in the main text:
"We note that while bound excited states cannot be separated from the ground state in 12C(p,2p)11B events, their contribution is very small [20] and should not impact the measured momentum distribution"

And with a reference to the Methods section that now states:
"We select a bound 11B where the 3/2- ground-state is populated with the largest cross section. However, we cannot distinguish bound excited states that de-excite via -ray emission that are also populated in our experiment. Previous works [20] found the contribution from such states to be small, coming primarily from the 1/2- and 3/2- states that contribute ~10% each to the total cross section. This contribution also corresponds to p-shell knockout and does not impact the resulting momentum distribution significantly."

This is fine but please quote the sigma value of the energy window of the selected QE events.

If you refer to the excitation up to the separation energy, the neutron (proton) separation energy of 11B is 11.4 MeV (11.2 MeV).

The bound excited states that are dominantly populated, and we are referring to, have excitation energy of 2.1 MeV (1/2-) and 5.0 MeV (3/2-).

3)

L 827-828: What is the phi acceptance of the two proton arms? The distribution shown in Extended data Fig. 2c could just be an artifact of their limited acceptance?

It is not, as evident by the comparison with event mixing shown below by the red histogram.

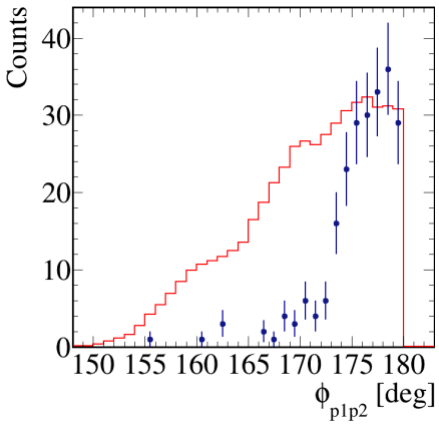

Fig. 3: Off-plane opening angle.

Good! I would propose to add the random curve to Fig. 3 together with an appropriate sentence in the text.

We added a sentence in the figure caption. We propose not to include this line in the figure itself as it could require adding such lines to other figures which we think will take away attention from the main points of the paper. Also note that the importance of such a comparison is very different when working with small solid angle spectrometers as oppose to large acceptance detectors.

4)

How sensitive are the results to variations of the beta selection cuts on the proton tracks?

The figure below shows the beta distribution for the two particles identified in the arms with all analysis cuts applied except for the beta selection cuts. Practically all resulting events pass our beta selection cut marked by the red square in the figure below. Thus, our final results like momentum distributions etc. are not sensitive to this selection cut.

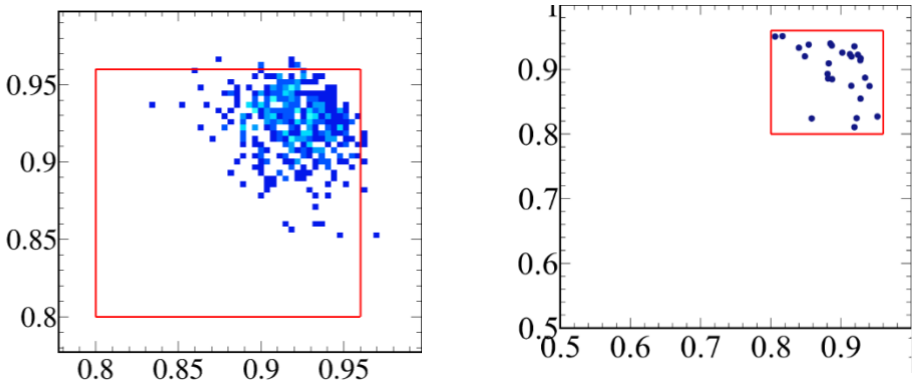

Fig. 7: Beta1 vs. Beta2, left vs. right arm. Left: for meanfield 11B events. Right: with SRC selection (10B) and $|t|,|u| > 1.2$ GeV² where the $|t|,|u|$ cut remove the low beta events.

If this is so, you actually do not need the beta1-beta2 cut at all. Why are you applying it?

Indeed, there is some redundancy between the cuts. Starting with this cut helps 'clean' things up before looking at the various distributions and define our other cuts.

5)

Fig. 1b: could you quote the relative abundances of 11B, 10B and 10Be?

We don't intend to quote the relative abundances in the analysis presented in this draft.

Why not?

Fig. 1b is qualitative and we do not wish to make it quantitative. All we want to show here is that our experimental setup can detect and identify various types of fragments, which is a very common practice in such nuclear structure papers. Quoting the requested numbers would require adding details and a discussion that distracts the reader from the main point of the paper. There will be follow up papers where we analyze lighter fragments as well and discuss these numbers.

6)

Following the discussions on June 1st

We show in the following the energy-momentum conservation for the quasielastic reaction:

$P_{12C} + P_{target} - P_{11B} - P_{p1} - P_{p2}$,

using the lab frame variables. The distributions are compared to our *p*-shell p2p simulation (red line). The single momentum components and the energy are shown.

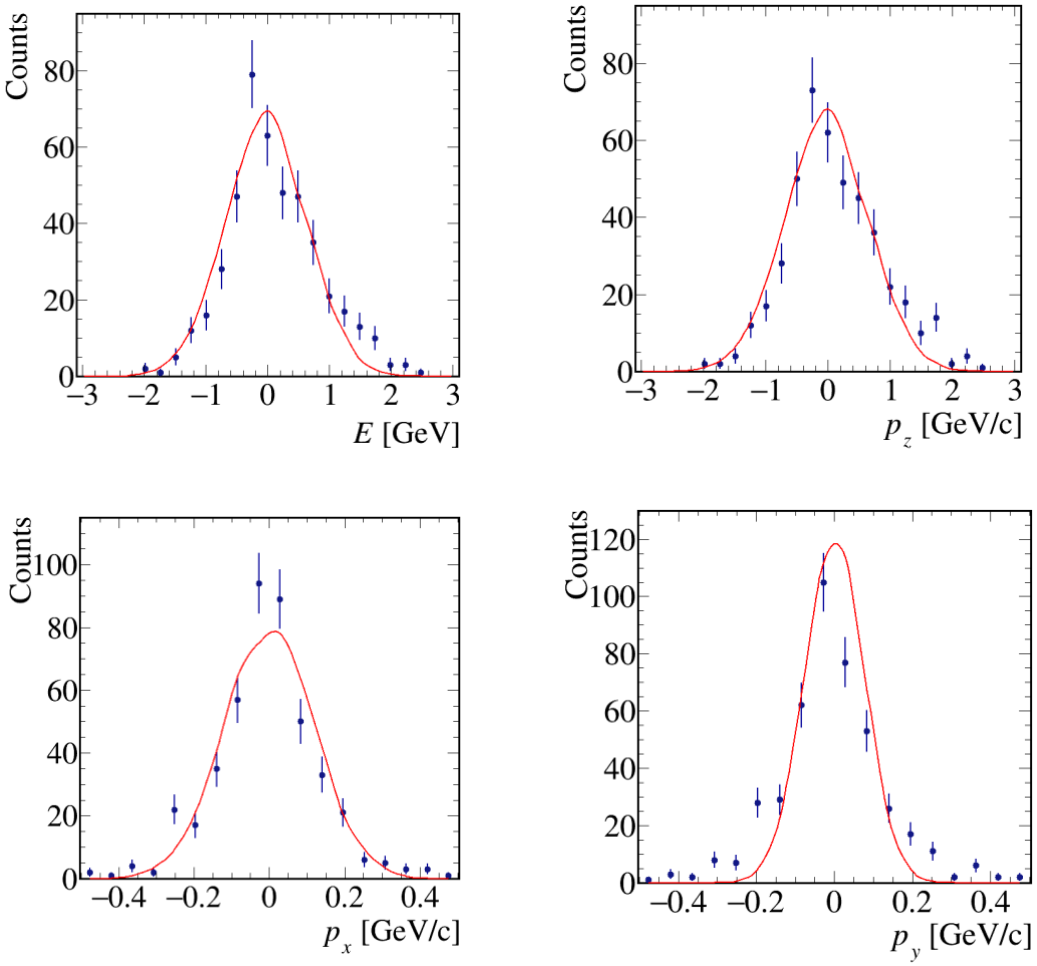

Fig. 16: Four-vector components from energy-momentum conservation in the quasielastic 12C(p,2p)11B reaction, compared to simulation (red line).

Note that when no resolution is included, the simulation reproduces a delta distribution.

This is great! But with energy and momentum resolution of the order of 1 GeV, there is room for obeying E and p conservation with one of the detected particles being a pion instead of a proton, Therefore, to complete the argumentation you should show that assuming that one of the two arms detects a pion instead of a proton, leads t**o unphysical or** unrealistic results. In this case, the energy and momentum distribution should give the E and p of the undetected proton:

$P_{undet} = P_{12C} + P_{target} - P_{11B} - P_{p1} - P_{p2}$

Where P_1 or P_2 is a pion. One should consider two cases here:
a) the particle detected in the same side of 11B is the pion,
b) the particle detected in the opposite side of 11B is the pion.

As requested, we calculated the equation above for our final QE 11B events sample, only assigning a pion mass to one of the particles, (i.e. recalculated its 4-momentum vector using that mass). The plots below show the missing mass of the reaction, i.e. P_{undet2}. As can be seen, the resulting distribution is unphysical. We repeated this exercise using our simulated events, which we know have two protons, and found that the incurred assignment of a pion mass to one of the protons lead to the same unphysical distributions in good agreement with the data.

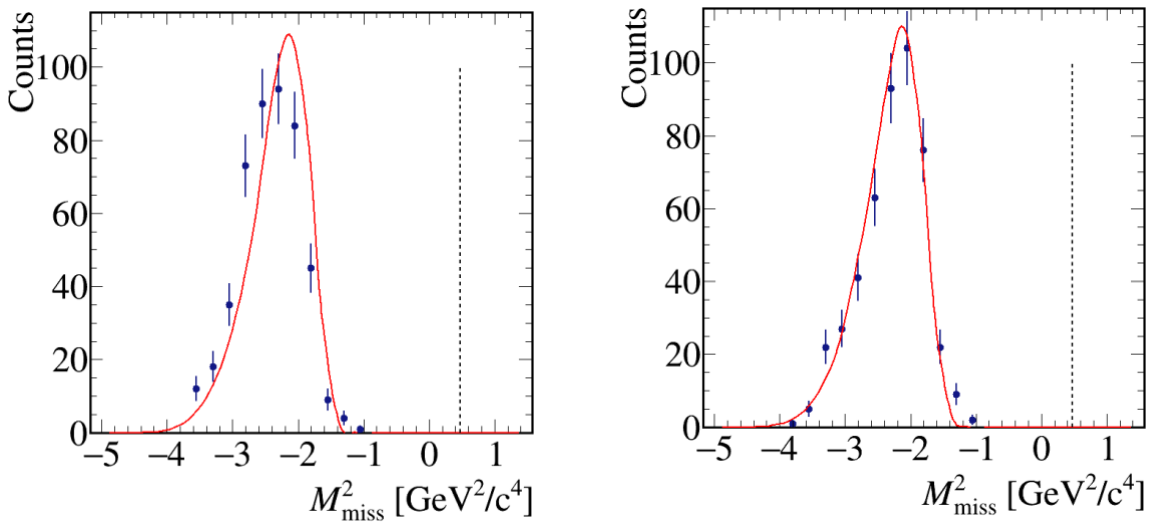

Fig. 2.1: Missing mass squared assuming pion and proton instead of two protons. The dashed line indicates the lower limit we apply in the QE event selection, our data sample is well separated from pion contributions. Left and right panels correspond to case (a) and (b) above.

Comments on the paper draft circulated on June 2, 2020.

-You should mention somewhere in the experimental set-up or in the single proton knockout section that the particles detected in the 2 TAS are assumed to be protons.
Done.

"The time difference between the RPC and t_0 signals define the proton time of flight (TOF), that is used to determine its momentum from the measured track length, assuming a proton mass"

-Fig. 1a: Could you modify the Figure to show all the elements mentioned in the text? If the target region is too crowded you could consider adding an insert.

We prefer keeping it as is. We also don't have simple access to the designer that made this version for us. The elements not explicitly shown are part of the BCs which we do indicate via the orange lines.

-L 112-115: I think that the wording would be more precise or correct if it is modified to read: "Each spectrometer arm consisted of two scintillator trigger counters (TC), a gas electron multiplier (GEM) station and a multi-gap resistive plate chamber (RPC) wall.

Done.

-L 126: a beta value of 0.96 corresponds to a p momentum of 3.3 GeV/c not to 2.5 GeV/c.

The momenta we quote correspond to beta between 0.85 – 0.935. We apply a wider cut to be sure we don't cut out the signal only the region that is far away from it. Text was clarified.

-L 199: please quote the 1sigma value of E_miss and teta1+teta2

$\sigma(E_{miss}) = 0.108$ GeV

$\sigma(\theta_1 + \theta_2) = 1.8°$

Added to the Methods Section: "The standard deviation was obtained from a Gaussian fit to Emiss ($\sigma = 0.108$ GeV) and $\theta p1 + \theta p2$ ($\sigma = 1.8°$)."

-L 239: it seems that you have added quadratically the statistical and the systematic uncertainties. This is bad practice and should not be done. Please quote separately the two uncertainties as you did in the tables presented in your responses.

Done.

-L 240-245: the entire section is devoted to the exclusive measurement with 11B and here you mention measuring 10B and 10Be. Obviously an additional n or proton is involved here and some more explanation is needed. Are the cuts the same as for 11B? Could you be detecting a d in one of the arms in the case of 10B? If so, you have an exclusive channel and the detected particles should satisfy E and p conservation.

We made the text clearer. The event selection is based on (p,2p) kinematics which is independent of the fragment. There are no deuterons in these reactions, it's a ^{11}B that decays via one proton or neutron emission. We don't attempt to detect that proton / neutron as it is not clear we can do it and it is not needed for this work.

-L 251-262: this paragraph does not really fit here.

We edited this paragraph and moved some of the details and references to the conclusion:

"Next we study SRCs by selecting12C(p,2p)10B and12C(p,2p)10Be events. SRC breakup reactions produce10B and10Be fragments when interacting with a proton-neutron (pn) or proton-proton (pp) pair, respectively. The fragment selection guarantees exclusion of secondary scattering processes as shown in the previous section. It implies also a selection of an excitation-energy window of the residual A-2 system corresponding to its nucleon separation energy. As pn-SRC were shown to be 20 times more abundant …"

-L 272: result → results

Done.

-L 274: neutron emission → neutron or proton emission, respectively.

In the case of 10B couldn't you have a d knockout?

No. The kinematics is different and cross-section much smaller.

-L 276: 10B → 10B or 10Be.

Done.

-L 282: p_miss is defined by eq. (6) and it should be mentioned here, to avoid any confusion with p_miss as defined in eq. 2

P_miss is defined only by Eq. 2, and is what is used in the text. Eq. 6 defines a different quantity, P_miss,excl. that is not the one used in the quoted line.

-L 317-324: This text is not clear. Alpha is not defined.

We removed alpha from this paragraph.

-L 327: "…distribution of the cosine of the angle between the missing momentum and the undetected recoil nucleon momentum." Not clear. What is the difference between these two quantities? The missing momentum is defined in eq. 6 and that same equation is by definition the momentum of the undetected nucleon.

The missing momentum is balanced by both the 10B and undetected neutron momentum. To make it clear we added "(Eq. 2)" after missing momentum.

-L 502-514: This is never done in the large collaborations working in high energy nuclear or particle physics. I know that the journal Nature requires that but let me quote here what STAR, PHENIX and HADES have done in their recent papers published in Nature:

STAR 2020:

Author contributions: All authors made important contributions to this publication, in one or more of the areas of detector hardware and software, operation of the experiment, acquisition of data and data analysis. All STAR collaborations who are authors reviewed and approved the submitted manuscript.

PHENIX 2019:

Author contributions: All PHENIX collaboration members contributed to the publication of these results in a variety of roles including detector construction, data collection, data processing, and analysis. A subset of collaboration members prepared this manuscript, and all authors had the opportunity to review the final version.

HADES 2019:

Author contributions: All authors have contributed equally to the publication, being variously involved in the design and the construction of the detectors, writing software, calibrating subsystems, operating the detectors and acquiring data, and finally analysing the processed data.

I personally prefer the PHENIX formulation but the STAR one is also fine.

Various large collaborating working in high energy and nuclear physics do follow the formal requirement of the journal (see examples below). We prefer to also do so.

IceCube: https://doi.org/10.1038/nature24459
https://doi.org/10.1038/s41567-018-0172-2

PRad: https://doi.org/10.1038/s41586-019-1721-2
CLAS: https://doi.org/10.1038/s41586-018-0400-z
https://doi.org/10.1038/s41586-019-0925-9
https://doi.org/10.1038/s41586-020-2021-6
Alpha: https://doi.org/10.1038/s41586-020-2006-5
nEXO: https://doi.org/10.1038/s41586-019-1169-4
nDVCS: https://doi.org/10.1038/s41567-019-0774-3
MAGIC: https://doi.org/10.1038/s41586-019-1754-6
ISOLDE: https://doi.org/10.1038/nature12073
https://doi.org/10.1038/s41467-019-10494-5
RIKEN: https://doi.org/10.1038/s41586-019-1155-x

Comments from Mikhail Kapishin

Line 16: "The ground-state distribution of single nucleons is studied" contradicts to Line 189: "We note that while bound excited states cannot be separated from the ground state"

The contribution of the excited states is very small and we don't think that this is a detail we should discuss at the abstract level.

Lines 213-222: Considerable fraction of QE events are beyond the back-to-back peak in the angular distribution. These could be events with additional pions in the final state or excited B11 with gamma emission. From this plot we cannot claim that the fraction of these types of events is negligible (see statement at line 189).

The angular distribution, including its tail, is fully explained by our simulation. Therefore, we conclude that the tail is due to resolution effects.

Lines 239, 244: specify statistical and systematic uncertainties. Fractions of B10, Be10 are only for the measured kinematical range in Emiss/ angle and Pmiss, not for the full phase space. It is not specified here.

We now separately present the statistical and systematic uncertainty and clearly state that these numbers refer only to our measured kinematics.

Lines 273-274: -> via neutron (proton) emission

We changed the text to 'nucleon emission'.

Paragraph lines 350-361: What is the resolution of cos(p_B10,p_rel)? The poor resolution could be a reason for a flat cos distribution. Than the statement that there is the experimental evidence of the factorization is too strong.

In order to investigate that we fed the GCF with three different correlations between center-of-mass p_cm and relative momentum p_rel, and calculated the chi² between simulation and data:

(a) p_cm and p_rel aligned parallel (cos = +1): χ^2/NDF = 4.2
(b) p_cm and p_rel aligned transverse (cos = 0): χ^2/NDF = 2.1
(c) p_cm and p_rel aligned antiparallel (cos = -1: χ^2/NDF = 9.0
(d) isotropic (cos = uniform distribution): χ^2/NDF = 0.9

The resulting distributions in opening angle are shown in Fig. 2.2 below as residual between simulation and data (#sim-data), together with the factorized/isotropic version (panel d). The bestagreement in shape and χ^2 is established for the factorized version, ruling out that the distributions are dominated by resolution effects.

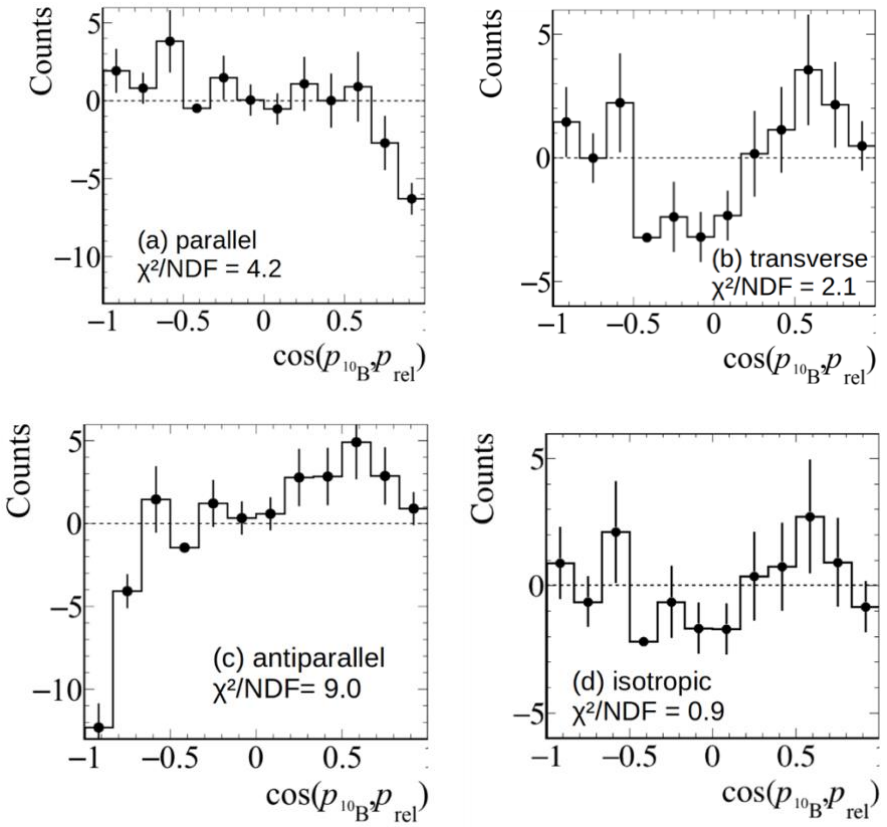

Fig. 2.2: Cosine of the opening angle between fragment and pair relative-momentum. The residual for GCF simulation – data is shown for the above listed cases. The simulation is fed with the different correlations between p_cm and p_rel: (a) parallel, (b) transverse, (c) antiparallel, (d) isotropic.

Line 588: include V.Zhezher (JINR) into the author list,

Done.

Corrections from Y.G. Ma related to the affiliation and author spelling:

Line 555, My name: Yu-G. Ma --> Y. G. Ma

Line 612, Our affiliation is missing, it is

17. Fudan University, Shanghai, China

Also Affiliation 18 is missing, I think it should

18. Tsinghua University, Beijing, China

Done.

Line 674: -> beam direction

Done.

Line 695: -> collected

Done.

Line 700: -> pulse height

Done.

Line 787: -> Figure 1b

Done.

Line 793: “with or without a two protons signal in the TAS.” Do you indeed analyze data without two tracks in TAS?

We removed the quoted statement.

Line 808: -> here

Done.

Line 815: -> such a fragment

Done.

Line 867: here need reference to Fig.2 to follow the text

Done.

Line 962-964: “However, the momentum distributions are dominated by the width of the input distribution”. It is not clear which kind of the input distribution.

Changed to “width of the input p-shell momentum distribution”

Line 1002: is rho = 0.07 g/cm3 for 1.1 atm. in the H2 target?

We removed the rho number.

Line 1004: You do not mention an attenuation effect for B11, B10, Be10 in materials behind the target. Even if the reaction probability is 5%, it should be mentioned, see my comment to the first draft:

-Make comment in the paper about possible contribution to B10 from B11 -> B10 and losses of B11, B10, Be10 reaction due to interactions after the target in MWPC/Si/GEM detectors

Added to the Methods Section:

“Additional break-up reactions due to material in the beam-line downstream the target and before the magnet were estimated (and scaled) based on the total cross section on carbon. The contribution to the secondary reaction probability is comparably small (< 5%), in particular production of 10B or 10Be via such reactions is negligible.”

Line 964: Put sentence “When comparing, the simulation is normalized to the integral of the experimental distributions.” After reference to Extended data Fig.3 (line 970).

Done.

Equation (3): is this formula exact or within an approximation? Is there any reference to its inference?

It is exact for ground-state transitions. Changes in mass due to excitation energy were addressed in the simulation but don´t impact the distributions that are shown.

Line 1108: “due to the transparency of the recoil nucleon”. What does it mean?

It means that in ~50% of the cases the recoil nucleon re-interacts with the nucleus and is “attenuated”. We added references to transparency papers.

Lines 1117-1118: “loss due to acceptance of the longitudinal momentum”. What does it mean?

The deep around zero seen in Extended Data Fig. 6a.

Line 1233: remove condition “!hBC3” from table 1. Looking to the BC3 amplitude distributions Sergey Sedukh proved that this condition was not used in the main SRC triggers.

We removed that detail.

Lines 1229-1230: remove “and no signal in BC3 which does exceed a certain upper threshold (!hBC3) to mainly reject unreacted particles”

Done.

Comments from Yuri Uzikov

1. Ref. [16] presents two-nucleon distributions over relative momentum and internal coordinate obtained from many-body calculations for different type of NN+3N potentials, but does not contain c.m. SRC distributions. The c.m. SRC distributions for 12C are shown to be the Gaussian with \sigma=140MeV/c (Cioffi degli Atti,Simula,1996) or very close to the Gaussian with \sigma=140-142 MeV/c (C. Colle et al., 2014) that all is in agreement with electron data (E.Cohen et al.,2018) \sigma= 143\pm 5 MeV/c.

Why not to take the c.m. distribution from above papers, mentioned by O. Hen, n(k_cm)=N\exp{-k_cm^2/(2\sigma^2)} with \sigma \sim 140 - 145 MeV/c to compare with BM@N data?

Indeed the GCF calculations use the quoted \sigma values and it is in good agreement with the BM@N data as shown by the comparison between the 10B distributions and the GCF curves.

2. Concerning one-nucleon distribution, in Methods (lines 913-924) the parameters of the Woods-Saxon potential are present which are used to calculate the proton momentum distributions in 12C within the shell model. At this point one need to know how well is described the charge form factor of 12C and, in particular, its radius with this potential. However, instead the h.o. distribution for nuclear density is given which cannot be obtained from the Woods-Saxon potential.

The Woods-Saxon potential used reproduces both the binding and experimental RMS radius of 12C as stated in the text.

References

[1] S. Khabarov, E. Kulish, V. Lenivenko, A. Makankin, A. Maksymchuk, V. Palichik, M. Patsyuk, S. Vasiliev, A. Vishnevskij, and N. Voytishin, EPJ Web Conf. 201, 04002 (2019).

[2] Y. Kovalev, M. Kapishin, S. Khabarov, A. Shafronovskaia, O. Tarasov, A. Makankin, N. Zamiatin, and E. Zubarev, Journal of Instrumentation 12, C07031 (2017).

[3] "Bm@n daq system," ().

[4] "Root Cern: Multi-dimensional fit," https://root. cern.ch/doc/master/classTMultiDimFit.html

[5] T. Aumann, C. Bertulani, and J. Ryckebusch, Phys. Rev. C 88, 064610 (2013), arXiv:1311.6734 [nucl-th].

[6] M. Hussein, R. Rego, and C. Bertulani, Phys. Rept. 201, 279 (1991).

[7] A. Ozawa, T. Suzuki, and I. Tanihata, Nucl. Phys. A 693, 32 (2001).

[8] G. Alkhazov, S. Belostotsky, and A. Vorobev, Phys. Rept. 42, 89 (1978).

[9] "Conceptual design report bm@n baryonic matter at nuclotron,".

[10] V. Babkin et al., Nucl. Instrum. Meth. A 824, 490 (2016).

[11] A. Kolesnikov, Position Laser Measurement.

https://doi.org/10.1051/epjconf/201920407009

https://doi.org/10.1088%2F1748-0221%2F12%2F06%2Fc06041

[12] arXiv: 1907.03658

[13] Phys. Lett. B 791, 242 (2019).

[14] Phys. Lett. B 780, 211 (2018).

[15] Phys. Rev. C 92, 054311 (2015).

[16] Phys. Lett. B 805, 135429 (2020).

[17] Nature 578, 540 (2020)

[18] Phys. Rev. Lett, 122, 172502 (2019).